

Liquid Hydrogen boil-off modelling & cryogenic cold integration for Fuel Cell Thermal Management in Aviation

Master Thesis

Energy Flow Process Technology,
Mechanical Engineering

Debdutta Chatterjee

by

Debdutta Chatterjee

<u>Student Name</u>	<u>Student Number</u>
Debdutta Chatterjee	5497205

Project Supervisors: Dr.ir Mahinder Ramdin
Dr. Othonas A. Moulτος
Research Group: Engineering Thermodynamics
Chair Committee Members: Dr. ir. Lindert Van Biert
Dr. ir. TMJ Nijssen
Faculty: Faculty of Mechanical Engineering, TU Delft



Contents

Nomenclature	iii
1 Introduction	3
1.1 Research Question	6
2 Literature Overview	7
2.1 How different is H ₂ from other fluids?	7
2.2 Hydrogen Boil-off Mechanism	9
2.2.1 Thermodynamics of boil-off	9
2.2.2 Heat Transfer boil-off mechanism for ambient heat ingress	11
2.2.3 Cryogenic vessels	14
2.2.4 Thermal Stratification	15
2.3 Dynamic Conditions for Boil-off	16
2.3.1 Filling	16
2.3.2 Sloshing	17
2.4 Solutions for boil-off reduction	18
2.5 Boil-off and Cryogenic energy integration schemes	20
2.5.1 Schemes for hydrogen boil-off capture	21
2.6 Application of Hydrogen as an Aviation Fuel	22
2.7 Research Gap	25
3 Methodology	26
3.1 Hydrogen Supply	27
3.1.1 Modelling boil-off while tank filling	27
3.1.2 Modelling boil-off at Stand-alone Condition	31
3.2 Power Generation	32
3.2.1 Fuel Cell Heat Release	33
3.3 Thermal Management System	35
3.3.1 Basic Vapor Compression Refrigeration system	35
3.3.2 Pumped 2-phase cooling	37
3.3.3 Single Phase cooling	37
3.3.4 Serial cooling using single phase circuit	39
3.4 Effect of Altitude Variations on Thermal Management system	40
4 Design of Integrated System Components	41
4.1 Fuel supply system	41
4.1.1 Fuel Tank Configuration	41
4.1.2 Tank pressure balance	41
4.2 Single phase heat exchanger design	44
5 Results	50
5.1 Reactant Supply and Fuel Cell Heat Release	50
5.2 Integration of Intercooler and De-superheater	50
5.2.1 Hydrogen Supply Stream	51
5.2.2 Thermal Management System	53
5.3 Integration of Serial cooling circuits	56
5.3.1 Single phase cooling circuit	56
5.3.2 Vapor Compression Refrigeration System	58
5.4 Results of component sizing	59
5.4.1 De-superheater	59
5.4.2 Intercooler	61

5.4.3	Integrated Single Phase circuit cooling	63
5.4.4	System parasitic load	65
5.4.5	Expansion valve	66
5.5	Comparison of thermal management system results	67
5.6	Results for dynamic conditions of boil-off	68
5.7	Results for stand-alone conditions of boil-off	69
6	Conclusions and Recommendations	74
A	Appendix	76
A.1	Choked Flow Equations	76
A.2	Heat Ingress in non-spherical tanks	76
A.3	Altitude effects on Fuel Cell performance	77
A.4	Defrosting of fuel cooled heat exchangers at regular intervals	77
A.5	Logarithmic mean temperature difference correction factors	79
A.5.1	De-superheater	79
A.5.2	Intercooler	79
A.6	Aircraft Dimensions	80
	References	81

Nomenclature

The following Abbreviations and Symbols can be used for reference.

Abbreviations

Abbreviation	Definition
BOG	Boil-off gas
BOR	Boil-off Rate (%/day)
BHS	Boil-off Handling System
CAPEX	Capital Expenditure
COP	Coefficient of Performance
FCHX	Fuel Cooled Heat Exchanger
GUI	Graphical user interface
GHe	Gaseous Helium
HX	Heat Exchanger
H ₂ O	Water
HTPEMFC	High Temperature Proton Exchange Membrane Fuel Cell
IRAS	Integrated Refrigeration and Storage
LH ₂	Liquid Hydrogen
LN ₂	Liquid Nitrogen
LNG	Liquefied Natural Gas
LTPEMFC	Low Temperature Proton Exchange Membrane Fuel Cells
LOHC	Liquid Organic Hydrogen Carriers
MLI	Multilayer Insulation
NASA	National Aeronautics and Space Administration
NIST	National Institute of Standards and Technology
NO _x	Oxides of Nitrogen
ODE	Ordinary Differential Equation
OPEX	Operational Expenditure
PORTHOS	Port of Rotterdam CO ₂ Transport Hub and Offshore Storage
PEMFC	Proton Exchange Membrane Fuel Cells
PFHE	Plate Fin Heat Exchanger
REFPROP	Reference fluid properties
ROI	Return On Investment
STP	Standard Temperature and Pressure
VCRS	Vapor Compression Refrigeration System

Symbols

Symbol	Definition	Unit
C_{OP}	Ratio of Ortho to Para concentration	-
ΔH_{vap}	Latent Heat of Vaporization	KJ/kg
μ	Joule Thomson coefficient	-
m	mass	kg
J	mass flowrate	kg/s
h	Specific Enthalpy	J/kg
u	Specific Internal Energy	J/kg
ϵ	emissivity	-
R	Universal Gas constant	J/(molK)
P	Pressure	bar
T	Temperature	K
σ	Stephan-Boltzmann constant	W/(m ² K ⁴)
c_p	Specific Heat capacity at constant pressure	J/(kg°C)
k	Thermal Conductivity	W/(mK)
h_c	Heat Transfer Coefficient	W/(m ² K)
Q	Heat Ingress	W
U	Overall Heat Transfer Coefficient	W/(m ² K)
\dot{q}	Flux	W/m ²
v	Velocity	m/s
Nu	Nusselt Number	-
Ra	Rayleigh Number	-
Ma	Mach Number	-
D	Diameter	m
r	Radius	m
Q	Volumetric Flowrate	m ³ /s
A_c	Cross-sectional area	m ²
A_s	Surface Area	m ²
ρ	Density	kg/m ³
μ	Dynamic Viscosity	kg/(m · s)
ν	Kinematic viscosity	m ² /s
ψ	Exergy	W
e	Specific Energy	kWh/kg
s	Entropy	J/(mol · K)
a	Acceleration	m/s ²
t	Time	s

Preface

Low temperatures have significant applications in today's world. From the medical industry, sample preservation in animal husbandry, space research, aircraft propulsion, fuel storage, heat recovery, atomic research, to various industries including LNG and LH₂ production and transportation—it is the world of Cryogenics! I wonder how can one not be a part of it. I have a strong affinity to low temperature research and I am eager to contribute in this field for the betterment of mankind.

Beyond its extensive applications, the urgent need for de-carbonization in our fight against climate change cannot be overstated. Reducing carbon emissions is essential for sustainable development and the preservation of our planet. Through the combination of cryogenics with hydrogen technology and other innovations, we can make significant strides toward a cleaner, more sustainable future. My project for my Master of Science degree is just the beginning of this journey.

First and foremost, I would like to express my deepest thanks to my supervisors, Dr. ir. Mahinder Ramdin and Dr. Othonas A. Moulton. Your guidance, expertise, and encouragement have been invaluable throughout this journey. Your constructive feedback and unwavering support have significantly shaped this research, and I am deeply grateful for your mentorship.

I would like to extend my gratitude to my Thesis Committee members, Dr. ir. Lindert Van Biert and Dr. ir. TMJ Nijssen, as well as the Thermodynamics research group under the department of Process and Energy, TU Delft. Your insights and suggestions during the presentations have enriched my work, and your availability for discussions has been helpful in refining my ideas and approaches. Your collaborative spirit and dedication have been a great source of motivation.

I am forever grateful to my parents, Arunima and Debashish Chatterjee, as well as my entire family and friends, for their unwavering support and encouragement throughout my academic journey. Your belief in me has been a constant source of strength.

Thank you all for making this journey possible.

*Debdutta Chatterjee
Delft, July 2024*

Abstract

De-carbonizing aviation is necessary for a sustainable future, and using hydrogen in a fuel cell, that produces water, can greatly reduce greenhouse gas emissions. Achieving higher gravimetric energy density with hydrogen compared to conventional jet fuels, involves storing it in cryogenic liquid form. Along with it, its cryogenic temperature range not only enables its use as chemical energy storage but also as a potential heat sink. However, rapid vaporization, known as 'boil-off,' limits the long-term storage of liquid hydrogen in fuel tanks, requiring regular venting due to self-pressurization over time. Additionally, hydrogen needs to be heated to the fuel cell's operating temperature before being used as a reactant. Understanding these requirements, this thesis focuses on three areas: predicting the maximum boil-off rate of liquid hydrogen while charging the fuel tank using a MATLAB simulation and the boil-off rate during the flight journey using a validated software called BoilFAST, and understanding feasibility of retrieving the boil-off for its integration with the fuel supply; designing a fuel supply system that integrates the boil-off with the vaporized liquid hydrogen supply line to the fuel cell system; and integrating the cryogenic energy of hydrogen with a ram air-cooled vapor compression refrigeration system (VCRS) based thermal management of fuel cell, with the intention of reducing its parasitic load and improving system compactness. Two methods were used for the thermal integration: VCRS involving fuel cooled heat exchangers that function as an intercooler between staged compression and as a separate de-superheater before the ram air-cooled condenser; and VCRS with a separate single-phase, 52% ethylene-glycol based serial cooling circuit with four fuel cooled heat exchangers (FCHX). This resulted in a significant reduction of parasitic load by 13.4% and 26% when integrated with the intercooler system and single-phase serial cooling system, respectively. The study also examined the expected additional component weight, considering the aviation sector's preference for lighter systems. The findings demonstrate that the holding time of the fuel for minimum 13 minutes after tank filling and before the start of the propulsion system unit can allow a controlled amount of boil-off gas to be integrated with the fuel supply. Utilizing cryogenic energy for thermal management can significantly enhance the system's coefficient of performance by 15.3% and 33.3% respectively. Future work should involve experiments to obtain actual boil-off rates at different ambient exposures of fuel tank, tests on sloshing effect due to turbulence during flight journeys, analysis of thermal stress effects in cryogenic heat exchangers due to high temperature gradients, and testing new compatible mixed refrigerants with improved thermal properties for optimum cryogenic heat exchange.

1

Introduction

There is a growing consensus that hydrogen (H_2) will be essential in the global shift towards a sustainable energy economy [1]. H_2 and its derived fuels can play a vital role in reducing emissions in sectors where it is challenging to find alternatives or implement other solutions, such as for long-distance transport. This is important for the overall effort for decarbonization. H_2 based fuel cells can power vehicles, offering a zero-emission alternative to internal combustion engines. They emit only water vapor and heat, thereby enhancing air quality and diminishing the carbon footprint associated with transportation. H_2 is highly versatile and can effectively store energy, offering a practical solution to the intermittent power production from renewable sources. Stored H_2 can be smoothly converted back to electricity through fuel cells during periods of high energy demand or when renewable sources are inactive. As an asset of space exploration, H_2 is stored for use as rocket fuel due to its high energy content. The role of H_2 as an energy carrier has generated interest in various approaches related to its storage. To date, numerous methods of H_2 storage have been explored, as illustrated in the Figure 1.1.

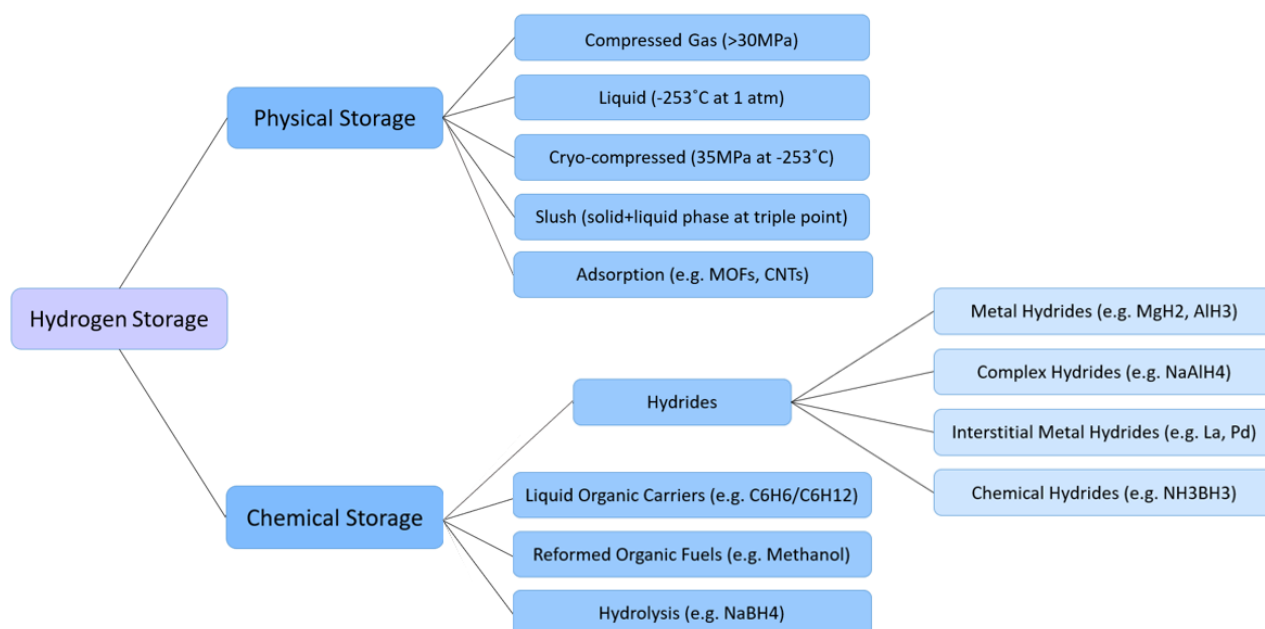


Figure 1.1: Flowchart on Physical Storage (in pure form) and Chemical Storage (in carriers) of H_2 that was reproduced from [2].

These include the potential for storage in its pure form and integration into various carriers. Pure H₂ can be stored in two individual phases: compressed and liquefied. For compressed storage, the main disadvantage lies in the size of the storage tank, given that compressed hydrogen has lower density compared to liquid hydrogen. The compression of hydrogen proves to be an energy-intensive process, thereby elevating the overall cost [3]. Cryo-compressed storage which is a combination of cryogenic liquid and compressed storage also has challenges such as expensive re-fueling infrastructure, tank design and high strength materials [2]. Slush hydrogen is a dual phase solid-liquid cryogenic fluid, where the particle diameter of the solid-phase is in the order of 10⁻³m. The flow pattern of slurry during transportation depends on solid fraction and flow velocity. When the solid fraction is high and the flow velocity is low, there is a risk of blockages at narrow flow passages such as in valves [4].

Storing H₂ as metal hydrides, and chemical alloys face quite a number of challenges such as the requirement of additional external energy source for dehydrogenation, making it less commercial [5]. For ship propulsion using hydrogen in the maritime sector, the Proton exchange membrane fuel cell (PEMFC) system is majorly used, but is limited by the requirement of extremely pure hydrogen (which gets contaminated with ppm levels of carbon monoxide or ammonia) [6]. Chemical mediums which store H₂ face the problem of slow reaction kinetics, formation of by-product and thermodynamic limitations [2]. Adsorption includes the effect of weak van der Waals forces that require high pressure and temperature to achieve a comparatively greater hydrogen storage density. It is also exothermic which would require an additional heat removal system. Liquid Organic Hydrogen carriers (LOHC) have drawbacks such as the requirement of purification after dehydrogenation, non-carbon-free storage and low H₂ density. Reformed Organic fuels such as ammonia contain high toxicity, possibility of NO_x generation when combusted, generation of extra heat during ammonia decomposition. The image below in Figure 1.2 shows the energy density of liquid hydrogen (LH₂) on a volumetric basis and the H₂ content on % weight basis compared to other forms of H₂ storage. It is understood from the illustration that LH₂ has a highest hydrogen content by weight, and a comparatively low volumetric energy density than H₂ in other mediums. Based on the comparisons made on the methods used for H₂ storage, the gravimetric compactness shown in Figure 1.2, and the requirement of its pure elemental form in most applications, the upcoming work sets an eye on LH₂.

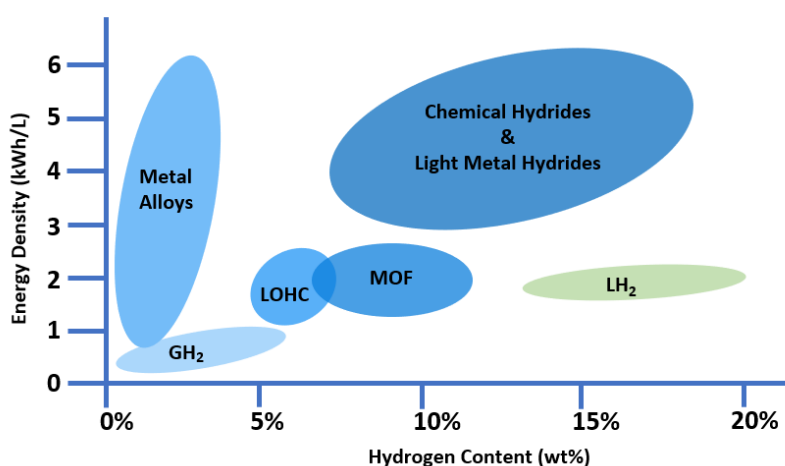


Figure 1.2: Energy content of different Hydrogen carrier methods that was reproduced from [7]. It shows that the weight % of hydrogen in LH₂ is the highest of all hydrogen carrier methods and its energy density (kWh/L) is highest when compared to storage in its pure form.

Ambient in-leak of heat in a cryogenic vessel causes the stored fluid such as LH₂ to warm up. A phenomenon known as ‘boil-off’ occurs as the heat from the environment vaporizes the cryogenic liquid in the vessel [8]. The process of liquefying hydrogen demands a substantial amount of energy, accounting for around 25-30% of the stored hydrogen’s energy content. Although the initial energy input for generating LH₂ is significant, the primary challenge in long-term storage and for non-bulk quantities, like in automotive applications, arises from the boil-off losses attributed to heat leakage through the

walls of the storage vessel [9]. Presently, the majority of ground-based large liquid hydrogen storage tanks with conventional cryogenic insulation, lead to boil-off rates ranging from 1% to 5% per day.

In the aerospace industry, boil-off is a significant issue, as seen in NASA's Space Shuttle program. Out of over 24,500 tonnes of LH₂ acquired, 45.4% was lost in the process of loading, storage or replenishment. Within this, 12.6% was lost while transporting from carrier trucks to storage tanks, and another 20.6% was lost from the storage tank to the shuttle's fuel tank [1, 6]. Boil-off is a critical concern during atmospheric departure, leading to increased vapor pressure and temperature. If warmer layers of boil-off gas enter the rocket's system, it may cause pump cavitation and even rocket destruction. Additionally, the unused boil-off becomes a liability to the rocket's payload capacity [10]. Mitigating boil-off during loading and unloading operations could reclaim around 1.5 million gallons, saving over \$2 million annually, by assuming a cost of \$1.50 per gallon [11].

Recognizing the severity of the problem, the United States has allocated \$48 million for hydrogen research and development, with an emphasis on addressing LH₂ boil-off. Another \$30 million has been invested in improving storage and fueling systems for LH₂ in vehicles. The Colorado School of Mines has received \$6 million to create a solid-state hydrogen loss recovery system, aiming to capture 80% of boil-off during LH₂ transfer [12].

LH₂ has emerged as a promising alternative fuel for airplanes, driven by the need to reduce carbon emissions and the aviation sector's growing emphasis on sustainability. It offers a high energy density and theoretically offers a clean chemical reaction, emitting only water vapor as a byproduct, making it an attractive option for future aviation. However, its use presents significant challenges, particularly in terms of storage and handling. It must be kept at extremely low temperatures (below 20K) to remain in its liquid state, requiring highly specialized and insulated tanks. The risk of hydrogen venting due to boil-off, where the LH₂ evaporates due to heat ingress, poses a safety and efficiency concern. This boil-off can lead to the loss of hydrogen fuel and requires careful management to prevent pressure build-up in storage tanks. Additionally, the production, transportation, and refueling infrastructure for LH₂ is not yet fully developed, further complicating its adoption in the aviation industry. Addressing these challenges is necessary to harness the full potential of LH₂ as a sustainable aviation fuel.

With global warming increasing the ambient temperature annually, the highest officially recorded temperature is 56.7°C (134°F), measured in Death Valley, California, in 1913. Africa's record is 55°C (131°F) in Kebili, Tunisia, in 1931. Iran holds Asia's record at 54°C (129°F), set in 2017. Europe's highest temperature, 48.8°C (119.8°F), was recorded in Sicily on August 11, 2021. The UK's highest temperature was 40.2°C (104.4°F) on July 19, 2022. In 2020, Seymour Island in Antarctica reached 20.7°C (69.3°F). The UN's World Meteorological Organization reports a nearly 3°C (5.4°F) rise in temperatures on the Antarctic Peninsula over the past 50 years [13]. If ambient temperatures keep increasing, the rise in ambient heat flux can reduce the dormancy time of any cryogenic fluid during its storage in a tank.

This increasing ambient intensifies the challenges of storing and transporting LH₂, as higher temperatures accelerate the boil-off rate. This not only leads to greater hydrogen losses but also increases the risks associated with pressure build-up and venting. Consequently, innovative solutions and technologies are urgently needed to minimize boil-off and manage the cold energy released during the process.

1.1. Research Question

Although LH₂ has the potential to be a key player in sustainable energy with its high energy density and as a pure fuel for aircraft, it is the risk of venting the H₂ due to boil-off that is holding back its potential. In exploring the untapped potential of LH₂ as a fuel in the aviation sector, understanding how to minimize and effectively utilize the cold boil-off energy becomes crucial.

To accomplish the main objective of this study that is to reduce the losses of hydrogen, it is necessary to address the following research inquiries:

1. **“What is an efficient way to tackle the challenge of minimizing the boil-off, during storage of LH₂ in a fuel tank of commercial aircraft?”**
2. **“For a certain boil-off rate, how can the LH₂ boil-off be captured and utilized rather than venting it out from an aircraft fuel tank while filling and during the entire journey of the flight?”**
3. **“Since H₂ is stored as a cryogenic liquid, how can the cryogenic cold be integrated as a potential heat sink to reduce the aircraft system load?”**

There are different perspectives of answering the above research questions regarding H₂ losses:

- By changing the thermodynamic conditions in the tank, thereby reducing the boil-off such as using active cooling (explained in the upcoming section 2.4), or catalyst for desired spin isomer conversion
- By altering the heat transfer from the surrounding into the tank using proper insulation or changing the ambient itself for portable tanks.
- For an existing boil-off rate, designing systems that can integrate and thus capture the boiled-off vapor using worst case scenarios

This thesis focuses on the third perspective, which is to understand and predict the boil-off rates when LH₂ is filled and stored in existing fuel tank configurations, and designing novel systems for integrating the BOG and its cold to the power generation system of a commercial short-ranged aircraft. Modelling of the effects of material and structural properties of tank and insulation and the thermodynamic variations to trigger and control spin isomer conversion are out of the scope of this thesis. The upcoming section gives a short overview from prior efforts made by researches on achieving similar targets.

2

Literature Overview

This chapter aims to gather findings from both theoretical and practical scenarios to understand the boil-off mechanism, model the boil-off process, study the existing technologies that utilize the boil-off gas and/or cold energy for certain applications and compare various methods of energy integration.

2.1. How different is H_2 from other fluids?

As the most abundant element in the universe, hydrogen stands out as a pivotal energy carrier. Understanding the behavior of elemental hydrogen is crucial, as it forms the foundational knowledge essential for grasping the processes involved in liquefying, storing, and utilizing it as an energy fuel. Despite its cosmic presence, elemental hydrogen is not naturally obtained on earth and requires energy to release elemental hydrogen from its compounds. At STP, elemental hydrogen takes the form of a diatomic molecule, with density of about 0.089883 kg/m^3 . The boiling point of hydrogen is at 20.3K , and at this temperature, it exhibits a density of about 70.927 kg/m^3 , as obtained from NIST database [14]. Figure 2.1 shows the phase diagram of H_2 , its triple point being at 21.2K and critical point at 32K . LH_2 is present within the enclosed blue shaded region [15]. When hydrogen is liquefied down to -253°C , its density substantially increases, about 775 times greater than gaseous hydrogen under normal atmospheric conditions [6].

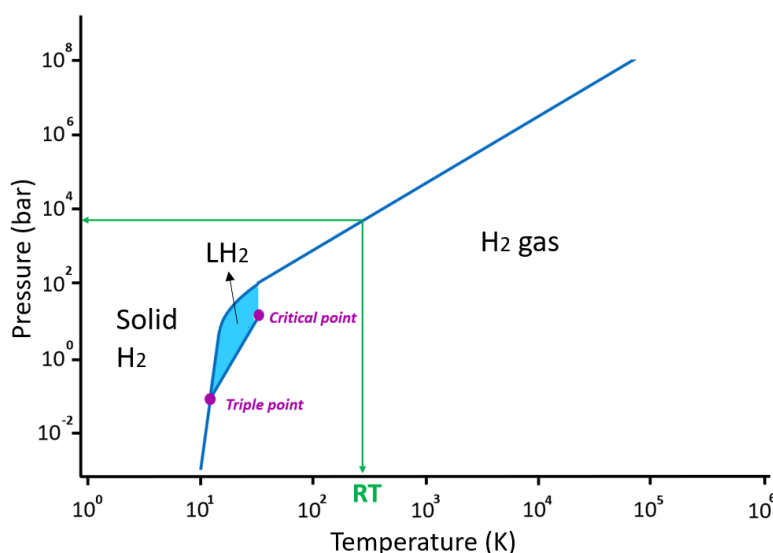


Figure 2.1: Phase diagram of hydrogen showing the triple point and critical Point in purple. Enclosed region in blue is where H_2 exists in liquid form that was reproduced from [15].

Hydrogen, having the highest gravimetric energy density among all other non-nuclear fuels, is widely regarded as an effective alternative for fossil fuels. The specific energy density of LH₂ is 120 MJ/kg whereas diesel has a specific energy density of 45.5 MJ/kg [16, 17]. However, LH₂ also has a volumetric energy density of around 8.5 MJ/L, in comparison to diesel fuels which have a volumetric energy density of 36.3 MJ/L. This means that, in order to store the same amount of energy, LH₂ requires more volume than conventional fuels for storage [6].

Coming to the atomic level, each hydrogen nucleus contains a single proton, resulting in two potential spin isomers for the diatomic molecule: para that is characterized by anti-parallel spin with lower rotational energy levels, and ortho which is the parallel spin with higher rotational energy levels [1, 18]. Despite the para isomer being at the lowest energy configuration, approximately 75% of hydrogen exists as the ortho-isomer at room temperature. The graph of para-hydrogen concentration is shown in Figure 2.2.

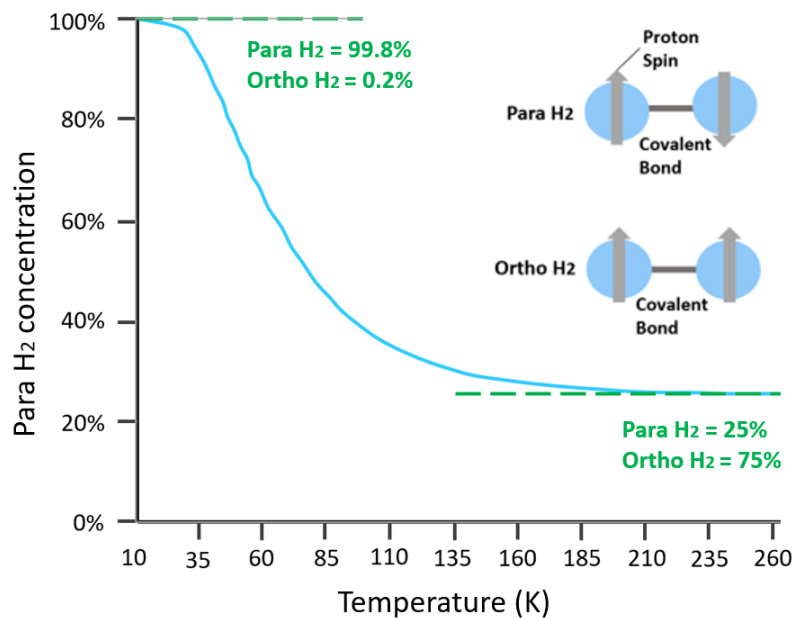


Figure 2.2: Para-H₂ % at equilibrium based on temperature and their respective spins that was reproduced from [1].

Intermolecular forces between two ortho-hydrogen molecules is greater than the intermolecular force between two para-hydrogen molecules as para-hydrogen has a greater resultant nuclear spin. The ratio of ortho and para hydrogen therefore affects the optical, thermal, magnetic and volumetric properties of hydrogen [1]. As the conversion from ortho to para hydrogen is highly exothermic in nature, the heat released is larger than the latent heat of vaporization of LH₂. This causes significant evaporation rates of LH₂. Therefore the conversion is carried out using catalysts such as iron oxide Fe₂O₃, nickel silicates NiO₃Si and chromium oxides during the liquefaction process, as the spontaneous conversion takes several days [9, 18].

The minimum theoretical energy needed to liquefy hydrogen is 2.3 kWh/kg when hydrogen is provided at a pressure of 20 bar. Additionally, the catalytic transformation from normal hydrogen (with 75% ortho-hydrogen and 25% para-hydrogen) to 100% para-hydrogen requires 0.65 kWh/kg_{LH₂}. The conversion of LH₂ to para-hydrogen is essential to minimize the formation of boil-off gas during storage. In practical applications, the liquefaction process may require up to 13.3 kWh/kg_{LH₂}, depending on the technique used and the quantity of hydrogen involved [19].

Another property of H₂ which makes it different from the other conventional gasses such as nitrogen, is that H₂ gas heats up when expanded in ambient conditions. This happens when the Joule-Thomson (JT) coefficient (which is the gradient of the isenthalp in Temperature-Pressure plot [20]) of H₂ is neg-

ative at ambient temperature and pressure. This leads to an understanding that having a negative JT coefficient under ambient temperature and pressure indicates that hydrogen gas tends to heat up during isenthalpic expansion, as observed in processes like throttling. For a gas to cool during expansion, the JT coefficient has to be positive. Inversion curve is the locus of all points at which the JT coefficient is zero ($\mu = 0$). The maximum inversion temperature of H_2 is at 193K (-80.15°C) [21], which is way lower than ambient temperature. This behavior of H_2 at ambient poses a challenge in liquefying hydrogen due to the difficulty in achieving cooling during expansion. It therefore becomes necessary to bring the thermodynamic state of the hydrogen gas below the inversion curve. The pre-cooling step is thus a crucial component in H_2 liquefaction processes. Following gives the relation of the JT coefficient denoted as μ .

$$\mu = \left(\frac{\partial T}{\partial P} \right)_H \quad (2.1)$$

The chapter of Cryogenic Technology in Ullmann's Encyclopedia of Industrial Chemistry [22], plotted the inversion curves of some conventional cryogenic fluids such as methane, air, neon, hydrogen and helium, as illustrated in Figure 2.3. It displayed that hydrogen has a relatively low and small enclosed area within the inversion curve compared to methane, air and neon. It also shows that the maximum inversion temperature of hydrogen, helium and neon is at a sub-atmospheric condition, unlike methane, and air. This makes it necessary for the hydrogen to be pre-cooled before the isenthalpic expansion step during its liquefaction, to bring the temperature of the hydrogen below the maximum inversion temperature, so that it cools when expanded.

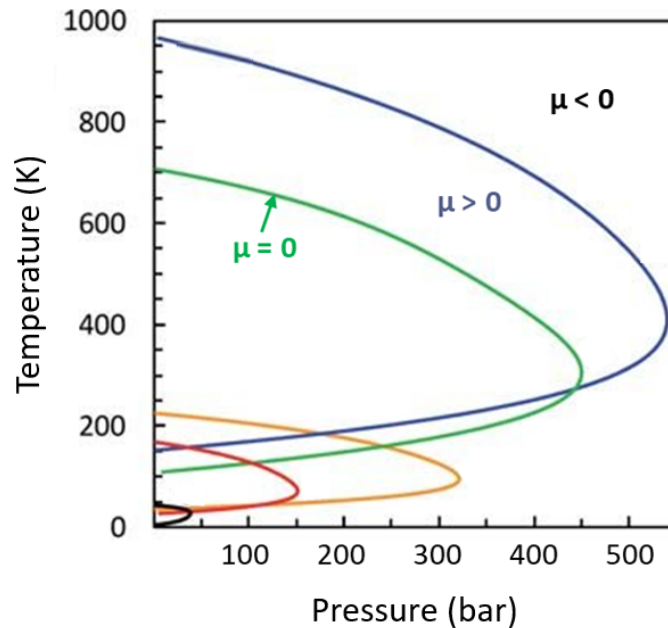


Figure 2.3: Inversion curve of different fluids. blue = methane, green = air, yellow = neon, red = hydrogen, black = helium. Reproduced from [22]. The JT coefficient for the particular fluid is negative outside the inversion curve, positive inside the curve, and 0 when exactly on the inversion curve.

2.2. Hydrogen Boil-off Mechanism

2.2.1. Thermodynamics of boil-off

This subsection considers the overall energy content and the energy changes involved, to understand how the boil-off phenomenon occurs [23]. Figure 2.4 illustrates the energy flows involved in the mass and energy balances for a two-phase cryogenic fluid in a storage tank. The wall of the storage vessel is assumed to have a homogeneous temperature distribution denoted by T_w .

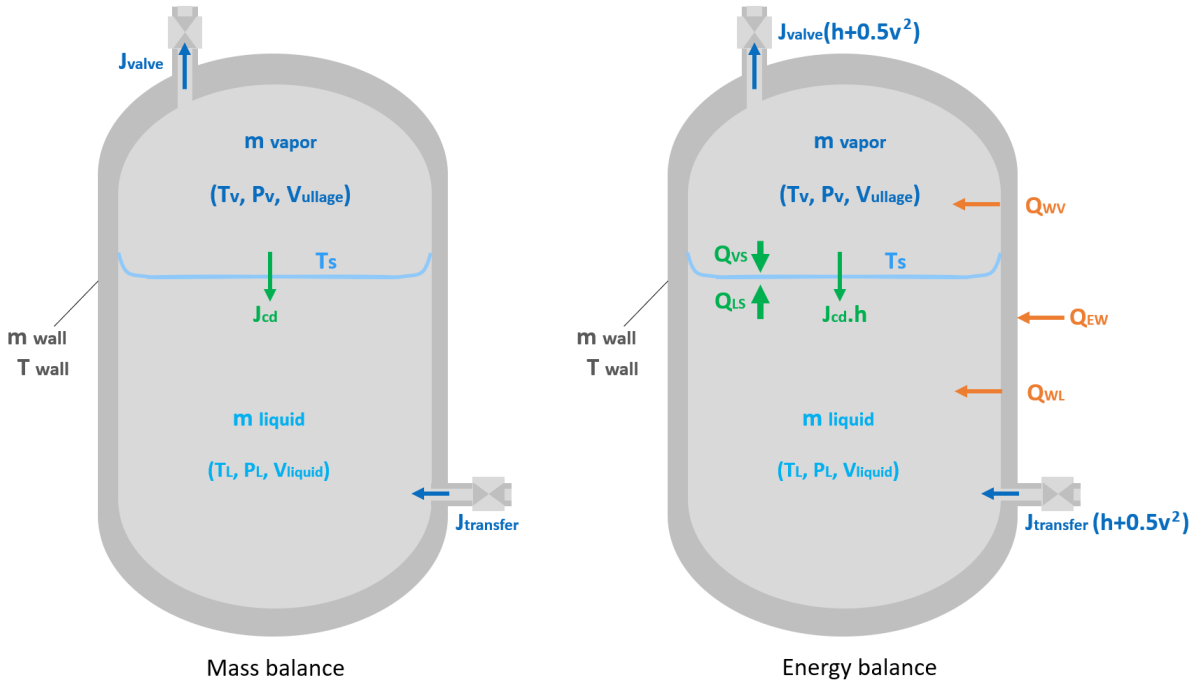


Figure 2.4: Mass and Energy conservation for 2-phase pure cryogenic fluid. Showing the ullage space and the liquid space. The arrows provide the direction of heat and mass transfer based on the type of balancing that was reproduced from [23].

The equations for the conservation of mass and energy for each phase separately are obtained as follows [23]:

$$\frac{dm_L}{dt} = J_{cd} + J_{transfer} \quad (2.2)$$

$$\frac{dm_V}{dt} = -J_{cd} - J_{valve} \quad (2.3)$$

Here the subscripts v and L represent vapor and liquid phase respectively, $J_{transfer}$ is the mass flow of the LH₂ that is entering the tank, J_{valve} is the mass flow of vapor leaving the tank, J_{cd} is the mass flow of the condensing vapor, where a positive J_{cd} would mean condensation and a negative J_{cd} would mean evaporation of LH₂, J_{cd} can be separately determined by the following equation that is governed by the fluxes through the interface:

$$J_{cd} = -\frac{Q_{LS} + Q_{VS}}{\Delta H_{vap}} \quad (2.4)$$

where Q_{LS} is the heat transfer from the liquid to the interface, Q_{VS} is the heat transfer from the vapor to the interface, ΔH_{vap} is the latent heat of vaporization of LH₂ in J/kg, $J_{transfer}$ can be obtained from the difference in total flow pressure (P_{total}) between the source of the incoming cryogenic fluid stream and the receiving storage tank, denoted using subscripts $_1$ and $_2$ respectively. Following shows the equation for $J_{transfer}$:

$$J_{transfer} = 2\pi \left(\frac{D}{2}\right)^2 \sqrt{\frac{2\rho_1(P_{total1} - P_{total2})}{\alpha}} \quad (2.5)$$

where D is the main valve diameter in the transfer line, α is the valve coefficient for that particular transfer valve, ρ_1 is the density of the incoming LH₂ stream through the transfer line, J_{valve} can be similarly obtained using choked flow equation A.1 which use the ratio of the vapor pressure and the downstream pressure (atmospheric pressure, if the BOG is released through a pressure relief valve). The condition for choked flow is when the Mach number $Ma = 1$. The choked flow equation was obtained from the gas releasing process in cryogenic systems in [24], and is provided in Appendix section A.1.

The conservation of energy is separately applied to each phase giving:

$$\frac{d(m_L \cdot u_L)}{dt} = Q_{WL} - Q_{LS} + PdV + J_{cd} \cdot h + J_{transfer} \cdot \left(h + \frac{v^2}{2} \right) \quad (2.6)$$

$$\frac{d(m_V \cdot u_V)}{dt} = Q_{WV} - Q_{VS} - PdV - J_{cd} \cdot h - J_{valve} \cdot \left(h + \frac{v^2}{2} \right) \quad (2.7)$$

where m_L and m_V are the mass flow rates of the liquid and vapor respectively, h is the specific enthalpy, v is the velocity, dV is the change in volume due to work done on/by the fluid, Q_{WL} is the heat transfer from the wall to cryogenic liquid, Q_{WV} is the heat transfer from the wall to cryogenic vapor. The conservation of energy for the wall of the cryogenic storage vessel is as follows:

$$m_{wall} \frac{d(c_{p(wall)} \cdot T_{wall})}{dt} = Q_{EW} - Q_{WL} - Q_{WV} \quad (2.8)$$

Q_{EW} is the heat transfer from the environment to the wall, $c_{p(wall)}$ is the temperature dependant specific heat capacity of the vessel wall. The heat transfers from the environment into the dual phase cryogenic fluid through the storage vessel wall, that are responsible for the thermodynamic changes denoted by the equations 2.6, 2.7 and 2.8 have been focused in the next sub-section.

2.2.2. Heat Transfer boil-off mechanism for ambient heat ingress

While section 2.2.1 dealt with energy transformations that occur within the cryogenic vessel, this section explains about the heat transfer mechanisms which is the driving factor of such energy transformations.

Heat transfer occurs through three main mechanisms: conduction, convection, and radiation. Through conduction, energy moves from one solid to another through direct contact, without any intermixing or flow of material. Convection involves the transfer of energy through the bulk mixing of fluids. In natural convection, the density difference between hot and cold fluids generates buoyant forces that induces the mixing, while forced convection relies on an externally imposed fluid pressure difference (created by a fan or compressor) for mixing. Additionally, radiation includes electromagnetic waves that are emitted from a hot body and is absorbed by a cooler body [25]. In cryogenic tanks, convection occurs only during the presence of fluid surrounding the vessel. For deep space propellant tanks, convection is only dominant at the inner side of the tank as the outside of the tank experiences vacuum. For stationary tanks in ground level and in aviation fuel tanks, the outer wall of the cryogenic vessel experiences natural/forced convection based on ambient wind conditions and the fluid touching the inner tank wall experiences natural convection when the fluid is kept stagnant (no sloshing). Radiation is always a contributing factor in the total heat ingress for all environmental conditions as radiation heat transfer requires no medium.

Certain assumptions were considered for the heat transfer equations:

- The diameter of the cryogenic tank is large compared to the total thickness of the wall and the insulation (very high radius of curvature), assuming a 1-D heat conduction through the walls
- The heat flux on the selected surface is uniform on that respective surface
- For the heat ingress through the top and bottom of the tank, the tank roof and base were assumed to be flat plate
- the material properties such as conductivity and diffusivity of the vessel are constant
- The inner wall temperature is homogeneous (neglecting thermal stratification)

A basic methodology has been outlined in Figure 2.5 to facilitate the understanding of how the heat transfer problem can be approached. The flowchart provides the steps involved to quantify the amount of boil-off and the corresponding equations that need to be referred to.

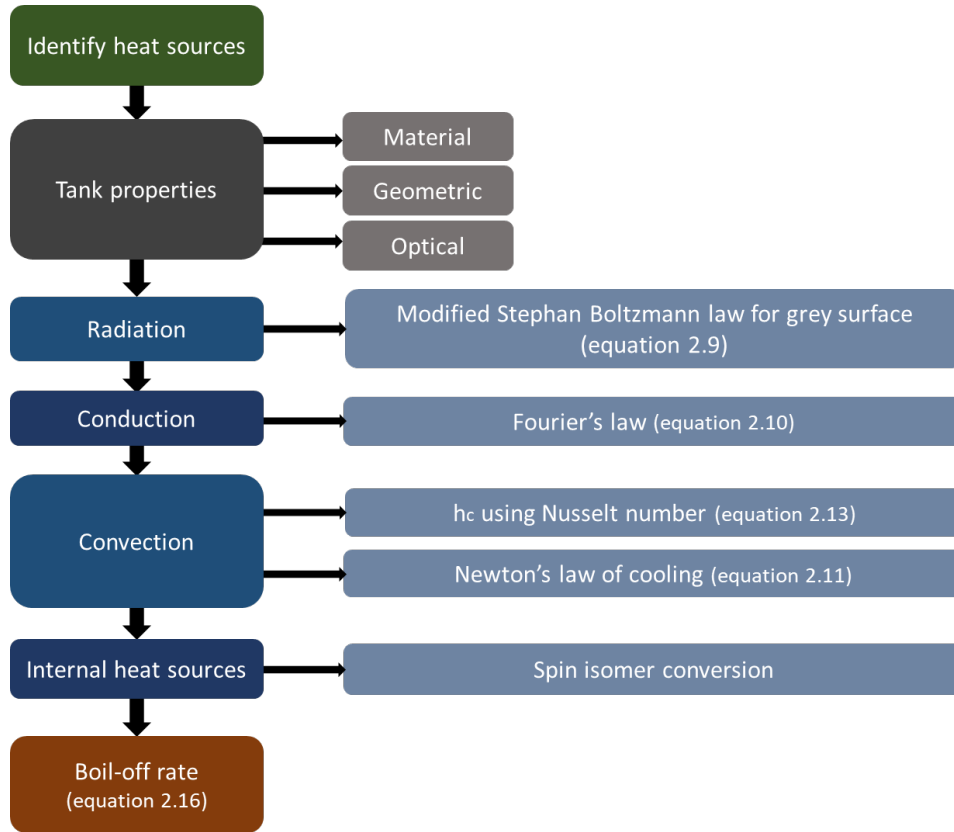


Figure 2.5: Flowchart showing a general methodology for calculating boil-off rate by referring to [26], involving the three modes of heat transfer and considering the properties of tank insulation material of LH₂.

To have a general overview of the heat ingress calculations through the storage tank, the following heat transfer calculations were obtained from [27]. To minimize heat ingress due to radiation from the surroundings, MLI is provided outside the tank which involves multiple reflective layers intended to provide thermal resistance. A separator material is used to keep the layers from thermally shorting. McIntosh [28], studied the heat ingress through the MLI by segregating the modes of heat transfer through the MLI: thermal radiation, gas conduction, and solid conduction through the separator material. It is understood that gas conduction was considered, as the thin gap between each MLI layer prevents any scale of convection currents to be developed. To understand the radiation flux passing through the MLI, the reflective layers were considered as parallel plates. Equation 2.9 was obtained to understand the exposure of the cryogenic tank towards incoming radiation. A small amount of radiation is absorbed by the reflector material that passes by conduction through the spacers.

$$\dot{q} = \frac{Q_{rad}}{A} = \frac{\sigma \cdot (T_w^4 - T_c^4)}{\left(\frac{1}{\epsilon_w} + \frac{1}{\epsilon_c} - 1\right)} \quad (2.9)$$

where Q_{rad} is the radiation heat entering the MLI, A is the surface area exposed to the radiation, $\sigma = 5.675 \times 10^{-8} \text{ W/m}^2 \cdot \text{K}^4$ is the Stephan-Boltzmann constant, T_w and T_c are the temperatures of the relatively warm and cold surface of consecutive MLI layers respectively, ϵ_w and ϵ_c are the warm and cold surface emissivities respectively.

The total conductivity of the MLI results from the sum of individual conductivities: through gas conduction for the trapped gas in between the layers, solid conduction through spacers and the radiation absorbed by each layer [28]. The heat ingress through the MLI can then be calculated using the total conductivity. The generalized equations of heat conduction from the ambient to LH₂, through the tank material can be determined using Fourier's Law of conduction. Considering cylindrical coordinates due to axi-symmetry of the tank, equation 2.10 is obtained [27, 29].

$$Q = -k_{\text{tank}} \cdot A_s \cdot \frac{dT}{dr} \quad (2.10)$$

where k_{tank} is the heat conductivity of the tank material along tank radius, r is the radial direction (along the thickness of the wall) as per cylindrical coordinate with units in metres. By referring to the resistance network shown in Figure 2.6, the Fourier's law is modified to also account for the convection effects forming a general heat transfer equation as follows [30]:

$$Q_{\text{in}} = U \cdot A_s \cdot (T_{\text{in}} - T_{\text{out}}) \quad (2.11)$$

where Q_{in} is the total heat input from the surrounding (Appendix section A.2), A_s is the tank surface area, U is the overall heat transfer coefficient in $W/(m^2K)$, which is the reciprocal of the overall resistance to heat transfer as shown below:

$$\frac{1}{U} = R_{\text{conv}(\text{in})} + R_{\text{cond}(\text{wall})} + R_{\text{conv}(\text{out})} \quad (2.12)$$

where $R_{\text{conv}(\text{in})}$ and $R_{\text{conv}(\text{out})}$ are the inner and outer surface convection resistances of the tank, and $R_{\text{cond}(\text{wall})}$ is the conduction wall resistance of the tank. For non-spherical tanks, further analysis of the heat transfer equations have been provided in Appendix section A.2.

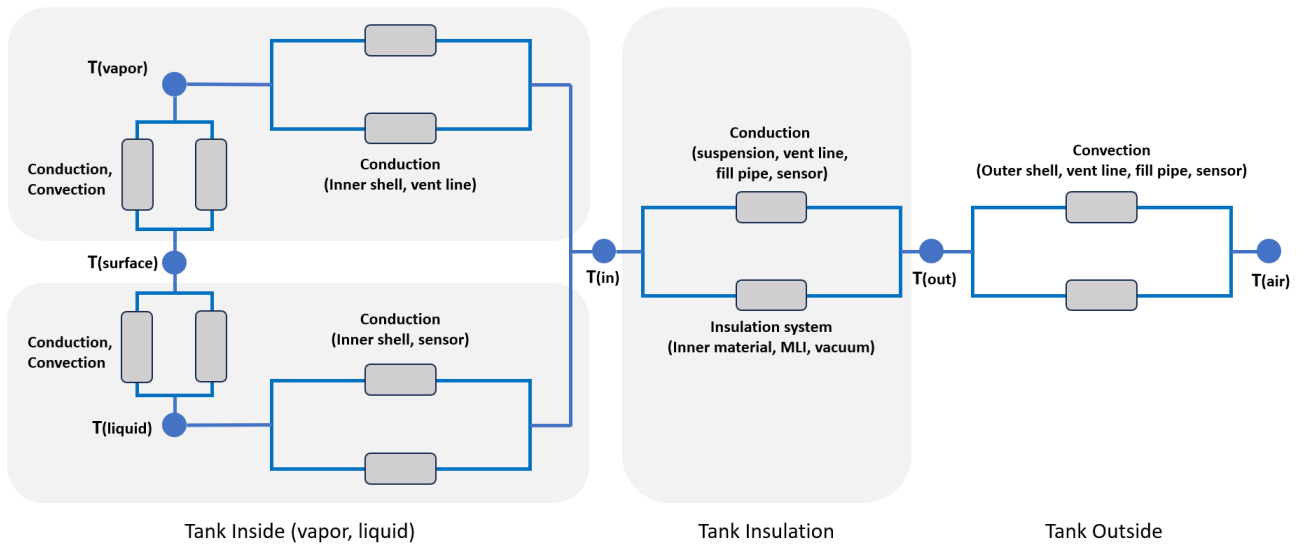


Figure 2.6: Heat transfer network of an LH_2 tank reproduced from [26], starting from the ambient air at the extreme right and the contact fluid phases in the tank interior at the extreme left. Going from right to left, the first resistance includes convection resistance due to the outer surrounding fluid behaviour in contact with the tank's outermost insulation surface, vent lines, charging port, and sensors. Next involves conduction resistance in series through tank and its insulation, and connected component walls in parallel. The inner side of tank is divided into separate resistances in parallel for conduction and convection through hydrogen vapor and liquid which are interconnected through the fluid-vapor interface (T_{surface}). The extra resistances in parallel denote resistances of any additional components.

The external heat transfer coefficient as used by the equations A.3, A.4, A.5 depends upon the external conditions that the tank experiences such as the wind speed and ambient temperature. In order to determine the heat transfer coefficients at the inside and outside of the vessel, the dimensionless number called Nusselt number (Nu) needs to be determined, as shown in the following equation [31].

$$Nu = \frac{\text{convective heat transfer}}{\text{conductive heat transfer}} = \frac{h_{c(\text{out})} \cdot D}{k_{\text{air}}} \quad (2.13)$$

where, $h_{c(\text{out})}$ is the heat transfer coefficient for the external surface of the tank, D is the characteristic length scale of the heat transfer phenomenon (which in this case is the outer diameter of the spherical tank), k_{air} is the thermal conductivity of air.

Variations within laminar to turbulent flow regimes, along with the development of boundary layers result in different Nu correlations. Natural convection is more dominant for very low/nearly stagnant wind speeds, and forced convection for higher wind speeds. Particularly for buoyancy driven flows, the Rayleigh Number (Ra) correlations are used to get Nu . The Nu correlations can be obtained from [31] and then rearranged and substituted in equation 2.13 to obtain the external heat transfer coefficient. Assuming the LH_2 to be stagnant, such as for ground based stationary storage tanks, The total heat generation in the cryogenic tank $Q_{\text{tank}(\text{total})}$ is found as:

$$Q_{\text{tank}(\text{total})} = Q_{\text{in}} + Q_s \quad (2.14)$$

here Q_s is the source term for heat generation such as due to the residual ortho-para hydrogen conversion. The maximum expected boil-off mass can be found by the following equation 2.15, after referring to [32]:

$$m_{\text{max,boiloff}} = \frac{Q_{\text{tank}(\text{total})}}{\Delta H_{\text{vap}}} \quad (2.15)$$

The assumption made in [32] was that the evaporated vapor of H_2 exits the cryogenic vessel without absorbing additional heat from the existing H_2 vapour. The boil-off rate (BOR) in (%/day) of the cryogenic liquid can be obtained as [33]:

$$BOR = \frac{Q_{\text{tank}(\text{total})} \cdot 24 \cdot 3600}{\Delta H_{\text{vap}} \cdot V_{LH_2} \cdot \rho_{LH_2}} \cdot 100\% \quad (2.16)$$

where $Q_{\text{tank}(\text{total})}$ is the total heat increase in the storage tank, ΔH_{vap} is the latent heat of vaporization of the LH_2 , ρ_{LH_2} is the density of LH_2 . V_{LH_2} is the volume of the LH_2 in the storage tank m^3 , obtained from the % fill level of the tank times the tank volume. The latent heat of vaporization can be determined by rearranging the Clausius-Clapeyron equation obtained from [34]. The corresponding boil-off amount per day can be determined by equation 2.17.

$$\dot{J}_{\text{BOG}} = V_{LH_2} \cdot BOR \cdot \rho_{LH_2} \quad (2.17)$$

2.2.3. Cryogenic vessels

The rate and extent of heat transfer depends upon the environment that the tank is experiencing. To identify the effect of surrounding heat sources impacting the tank, it is essential to have an understanding of the application, location, shape, and dimensions of the storage tank. The possible categories of LH_2 storage tanks include [35]:

- Cryogenic tanks attached adjacent to the liquefaction plant used for storage prior to shipment of the LH_2 product to the end users. The storage tank capacity is determined by the capacity to be shipped and the production from the plant, shutdown time of the liquefaction plant.
- Secondary storage in stationary tanks that are filled in bulks by tankers, such as in ports for ship fuelling. These tanks are not attached to liquefaction plants. The tank capacity is determined by the quantity of LH_2 delivered by the tankers and the requirement at the supply base.
- Installations within the site of application. Factors such as required phase of the hydrogen, working pressure of the equipment and the quantity requirement determines the size and type of the cryogenic container.
- Small quantity storage tanks that are portable such as in vehicle fuel tanks, laboratories and are light weight.

To get a general understanding of the basic insulation level that is applicable to cryogenic vessels, the cross-section of an LH_2 tank showing the layers of insulation has been illustrated in Figure 2.7.

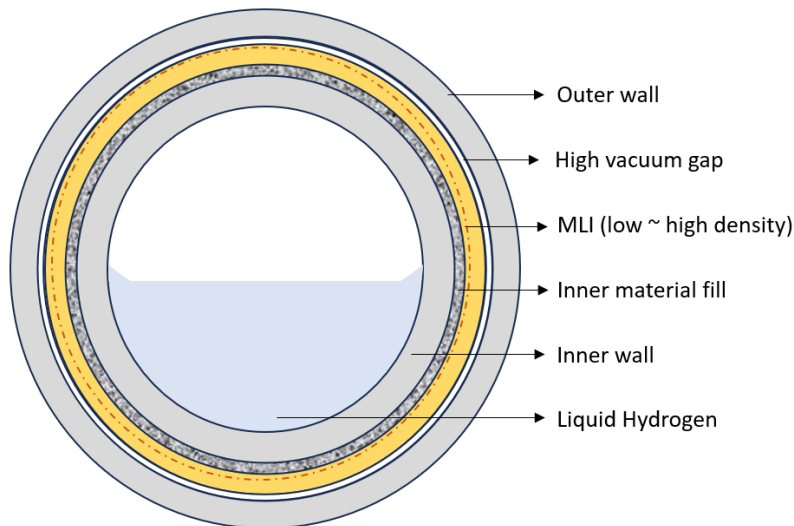


Figure 2.7: Cross-section of an LH₂ tank showing layers of basic cryogenic insulation which was reproduced from [26].

The shape of the tank also contributes in permitting heat transfer. For large scale hydrogen storage such as 3800 m³ tanks located in NASA developed for supplying LH₂ as a rocket fuel along with oxygen, and the tanks of 540 m³ in JAXA, Kawasaki are made spherical to have the least surface area to volume ratio. Tanks that are meant for bulk transport of LH₂ such as for aircraft propulsion and trucks used by Linde are non-spherical shapes such as cylindrical domes, to optimize aerodynamic drag and storage capacity in limited space [36, 37].

2.2.4. Thermal Stratification

The heat ingress causes the temperature of the vapor to increase faster than the liquid, due to the high thermal diffusivity of the vapor. This causes heat conduction through the vapor-liquid interface, resulting in a temperature gradient at the interface and the top layer of the fluid. This creates a temperature at the top layer which is different from the rest of the bulk fluid. The phenomenon of non-uniform temperature distribution within the individual phases is defined as thermal stratification. The presence of such temperature gradients can lead to higher boil-off rates, especially in the warmer layers where the liquid is more susceptible to vaporization [10, 29, 38]. Figure 2.8 shows the thermal stratification of LH₂, with colder layers near to the bulk core liquid shown in blue and warmest layer due to heat accumulation at the interface shown in red. Jing-Jie Ren et al. [38] observed that a stratified fluid presents a plume-like flow under a semi-circulation near the liquid surface. The rising stream near the heated walls due to the reduction in fluid density, carries the heat to the surface of the liquid by forming a free-convection boundary layer, thereby increasing the temperature of the interface and the top layers. The descending plume due to the circulation transfers the heat to the bulk fluid [39]. The effect of surface evaporation on stratification in LH₂ tanks of variable aspect ratios studied by Kumar et al. [40], observed that stratification was more for the tanks with higher aspect ratio.

To model the thermal stratification process, it is important to first understand the changes in fluid behaviour due to the changes in temperature dependent properties such as fluid density, changes in local velocity, and pressure of the fluid. The aspect ratio of the tank should be fixed to model for a particular case. The initial conditions need to be modelled, such as the initial temperature distribution of the LH₂ within the tank. Then the heat transfer mechanisms, including conduction, convection, and radiation need to be simulated to understand how temperature variations develop over time.

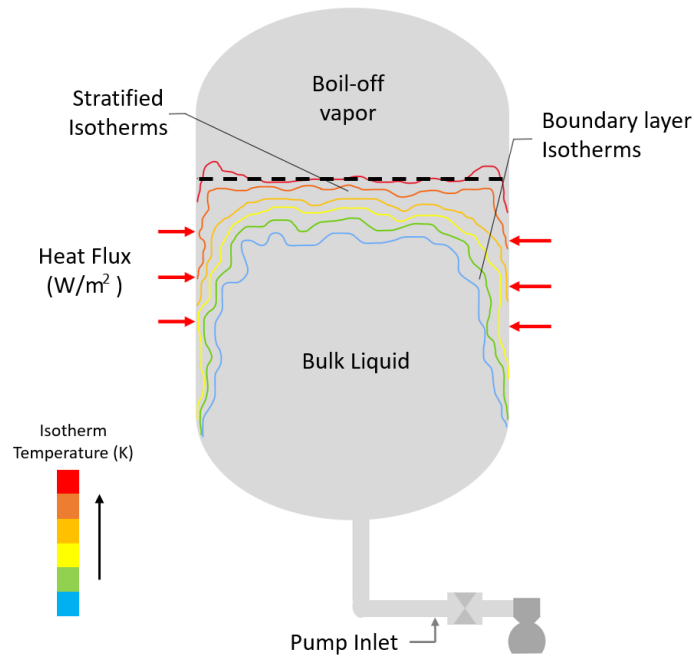


Figure 2.8: Thermal stratification process of a cryogenic propellant tank showing heat accumulation at the interface. The interface is marked in black dashed lines. The isotherms shown in red show the region of highest temperature of LH₂ and the isotherms in blue is almost equal to the bulk temperature of the LH₂, that was reproduced from [39].

The reverse effect known as thermal de-stratification is possible during the process of pressure relief when the safety valve opens and the pressure drops suddenly, causing most of the liquid to boil due to overheating. The formation of bubbles distributes the heat evenly within the liquid [38]. This mixing can expose previously colder liquid to warmer temperatures, also leading to increased vaporization and boil-off rates.

2.3. Dynamic Conditions for Boil-off

2.3.1. Filling

The losses due to boil-off along the pathway of LH₂ are significantly more during the transfer of LH₂ such as in fuelling process and transfer from supply trailer to storage tank [10, 32]. The effect of the filling process responsible for the boil-off losses is explained in this section.

During the condition of equilibrium at the interface of the fluid, the co-existing phases keep interchanging from liquid to vapor and back to liquid. This equates the condensation and evaporation rates, causing a net zero mass flux through the interface. During the process of filling the vessel with LH₂, non-equilibrium conditions exist as there is a non-zero net mass flux entering the control volume of the tank. This is when an effect known as the dynamical condensation blocking effect acts as a negative feedback by trying to bring the non-equilibrium condition back to equilibrium [23, 41]. Initially when the vapor condenses, molecules release the latent heat to the surface of the liquid, causing the interface temperature T_s to increase. The released heat must be transferred to the bulk cryogenic liquid. As LH₂ has a low thermal conductivity, this results in heat accumulation at the interface, causing greater evaporation rates. The rise in the evaporation rate outweighs the condensation rate, thereby blocking the condensation and stopping the resultant phase transfer. A thin saturated film develops, separating the liquid-vapor interface [41, 42]. One major consequence of this effect is that, while filling the tank with the cryogenic fluid from a higher pressure vessel to a lower pressure vessel, the level of fill of LH₂ stops at 50% when the pressure becomes equal, and requires an additional 35 hours to reach 95% fill level. Dynamic condensation blocking, was thus concluded to be a crucial phenomenon to consider in the modeling and design of cryogenic systems, particularly those associated with the current development of spacecrafts [42]. Figure 2.9 shows the temperature profile within a selected control volume

(CV) of the cryogenic tank. In the fluid layers touching the interface, the temperature gradients at each phase differ as vapor phase has a high diffusivity and the liquid phase has a low conductivity.

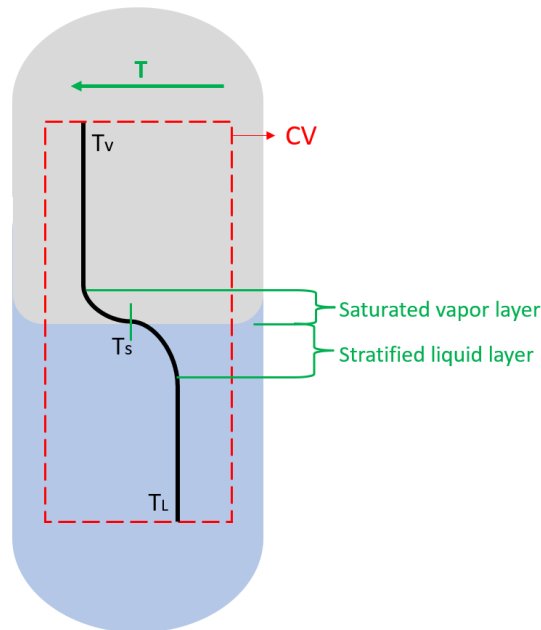


Figure 2.9: Temperature profile at the LH₂ interface showing saturated vapor layer and stratified liquid layer. T_v is the bulk vapor temperature, T_s is the interface temperature, T_L is bulk liquid temperature. The region of stratified liquid layer is at a higher temperature than bulk liquid due to heat accumulation at interface. The Saturated vapor layer is formed when the evaporation rate outweighs the condensation rate, that was reproduced from [42].

Guomeng and Zhang in [43] numerically studied the effect of sloshing (section 2.3.2) during the filling process of LH₂ in a storage tank. It was discussed that the filling process will be favourable when the pressure increase in the tank due to the initial vaporization is less. This is possible when the filling time is kept short. It was also observed in their study that a slight level of sloshing effects positively during the filling process. Presently, the majority of LH₂ loading facilities rely on gravity flow for filling the trailer, which can take approximately 5 hours. However, modern systems are increasingly adopting cryogenic pumps to significantly reduce the filling time [44].

A cryogenic pump is essential for transferring LH₂ to the trailer. The unloading process requires such a pump to transfer the LH₂ either to storage or to a high-pressure pump for dispensing. As a cost effective alternative to cryogenic pumps, pressure-build loops using vaporizers have been utilized for transferring LH₂. In this method, a specific quantity of LH₂ is evaporated and then returned as gaseous hydrogen to the top of the tank, effectively pressurizing it to facilitate the flow. Unlike the cryogenic pump, this approach doesn't require power and lacks moving parts. However, it raises the pressure and heat content of the storage tank, thereby increasing the chances of overall boil-off losses [19].

2.3.2. Sloshing

When a tanker ship, containing a partial load of liquid is subjected to oscillations at its resonance frequency, it triggers a turbulent free-surface movement known as sloshing. Sloshing caused by fluid movement during ship motion, contributes to increased BOG generation. This occurs by transferring heat to the tank system through dissipated kinetic energy and increasing the surface area between the liquid and vapor phases. [45]. If this phenomenon is unchecked, it can lead to ship instability, damage to the vessel's walls, and increased boil-off [46]. Fluid sloshing causes fast blending of the high-temperature fluid at the interface with the subcooled core fluid, leading to disturbances that alter the initial thermodynamic equilibrium inside the tank, leading to pressure drop. Under severe conditions, this may result in ullage collapse and potential destruction of the tank, posing serious hazards to

the safe operation of cryogenic propellant storage tanks [47].

The maritime sector is particularly affected by boil-off losses due to sloshing. Sloshing in maritime environments tends to be more constant and prolonged due to the continuous motion of the sea. In contrast, aviation sloshing is more intermittent, associated with specific phases of flight like takeoff, turbulence, and landing. A study conducted by Jessie et al. [45] on future LH₂ carrier ships thermodynamically modelled the sloshing mechanism by using LNG as the reference and replicating the model based on the properties of LH₂ for the tank design configurations. They found that for the same volume of the cryogenic vessel and the same level of insulation, LH₂ stores only 40% of the fuel energy with 9 times the boil-off rate, as compared to LNG. An LH₂ ship using fuel cells and a re-liquefaction system is needed to be at least 1.7 times larger than an existing LNG tank carrier to deliver the same amount of energy.

2.4. Solutions for boil-off reduction

This section summarizes the technologies that already exist to minimize hydrogen boil-off. Active and passive methods for boil-off reduction are two approaches used to minimize the boil-off of LH₂. Active methods involve the use of external mechanisms that actively control the thermodynamics within or heat transfer through the cryogenic storage system to reduce boil-off. Passive methods rely on inherent properties of materials or systems to naturally reduce heat transfer and thereby, boil-off, without the need for external energy input or active control systems.

The presentation by James at NASA Kennedy Space centre explained about the active mechanism for boil-off reduction using Integrated Refrigeration and Storage (IRAS) heat exchanger, and passive mechanism involving evacuated glass bubbles thermal insulation system [48]. The evacuated glass bubbles system is a passive method that is used as a substitute for perlite powder in large scale LH₂ storage tanks. From the comparative tests conducted between glass bubbles and perlite powder, it was understood that glass bubbles had a significantly low effective thermal conductivity. Glass bubbles also showed the least insulation heat leakage at high vacuum compared to aerogel beads and perlite powder. It was concluded that glass bubbles gave 40-100% better performance when compared to perlite and the boil-off rate is estimated to be reduced by 50%. Another study by NASA on the LH₂ storage tank at the Launch Complex-39, Kennedy Space Centre, obtained a 30% reduction of the boil-off rate by using glass bubbles instead of perlite [49]. Table 2.1 shows the performance test results of each insulation on boil-off rate for perlite and glass bubbles at 80% LH₂ fill level:

Table 2.1: Insulation performance of baseline perlite and glass bubbles based on observed boil-off rate, showing a 44% boil-off reduction when glass bubbles are used instead of baseline perlite [48].

	Baseline Perlite	Glass Bubbles	
Normal Evaporation Rate (%/day)	0.18	0.10	44% reduction
Boil-off rate (L/day)	386	216	
Vacuum Pressure (Pa)	4.5	1.3	

IRAS on the other hand, is an active method which consumes power and provides a complete controlled storage capability. It is a zero boil-off solution which is the capability to store a cryogenic liquid without the need for venting and without any loss of the product for an unlimited duration [48, 50, 51]. Study by Federico, Notardonato and an article from NASA demonstrate that the power consumption of IRAS system is cheaper than the loss by dispersing hydrogen into the atmosphere [19, 52]. IRAS systems for both small-scale (150 L) and large-scale LH₂ tanks that were 700 times greater in the volumetric capacity of small-scale tanks were successfully tested with the collaboration of Kennedy Space Center (KSC) and The Florida Solar Energy Centre (FSEC). For the smaller tank, a Gifford McMahon cryocooler was integrated with the tank using heat pipes that provided the cold to the copper straps submerged in the liquid region. The following Figure 2.10 shows a schematic of the components of the IRAS system used in the 125000 L tank at the Ground Operations Demonstration Unit [51].

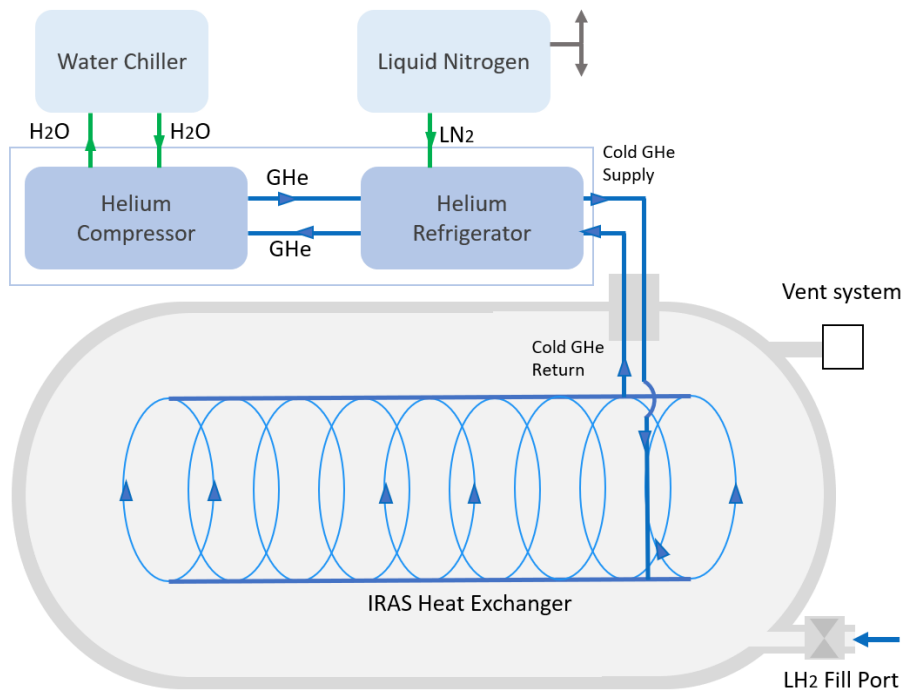


Figure 2.10: Components of IRAS tank system, showing a cooling coil inside the LH₂ tank. A water-cooled Helium compressor drives the Helium Refrigerator. The He gas is pre-cooled using LN₂. The illustration was reproduced from [51].

The large scale IRAS tank system uses a Linde refrigerator working on Brayton cycle with refrigerant as gaseous helium. The rated capacities of the refrigerator at 20 K is 880 W with liquid nitrogen (LN₂) pre-cooling and 390 W without the pre-cooling. The refrigerator unit is controlled independently. The helium compressor shown includes the oil-separation and the gas management system [51].

To minimise the effect of sloshing of cryogenic liquid on the inner walls of the carrier tank, Saif et al. [1], suggested the installation of baffles inside the tank. Other methods that were applicable to general cryogenic fluid behaviour, were also tested using other cryogenic fluids such as LNG, for instance, by requiring minimum fill levels for vessels before the transportation begins. However, even if this method is effective for LNG transport, it may not be adequate for transporting LH₂. This is because LH₂ has a higher rate of boil-off compared to LNG. Zuo and Jiang [53] studied the gravity level, fill level of the cryogenic fluid, the orientation and gaps of the baffles on the thermal stratification and pressurization of the cryogenic fluid inside the container. It was understood that baffles work better at mitigating the pressurization of the vessel when they are fully submerged into the liquid.

Pre-cooling the cryotank with liquid nitrogen prior to fueling minimizes the temperature gap between the cryotank walls and the LH₂. This approach served as a means to minimize boil-off losses during the fueling process in [32]. However, the issue of nitrogen freezing at the temperature of LH₂, along with other practical and economic aspects of the method was not taken into account and further consideration of pre-cooling methods was advised. The larger the tank size, the lower the boil-off. Spherical shaped tanks have lower boil-off than cylindrical tanks. The study also showed that using Aluminium as the cryotank material rather than Stainless steel resulted in the least amount of boil-off losses thereby requiring the least amount of LN₂ for pre-cooling. Significant reductions in boil-off losses during fuelling, that is between 38% to 60% of the total fuel mass (2.58 - 4.14 kg) when simulated, can be achieved by pre-cooling the cryogenic tank with LN₂. To validate the outcomes of the 'Fuelling Model', it is essential to gather experimental data. Furthermore, it is imperative to compare various approaches for minimizing boil-off losses during fueling, such as capturing and either re-liquefying the evaporated hydrogen or utilizing it for electricity generation. Other strategies that are to be assessed include filling the cryo-tank from the top and lowering the temperature of incoming LH₂ through the use of a sub-cooler.

Linde developed a cryogenic coupling for transport of LH_2 , while fuelling through transfer cables, that provided an effective way to vent out the pressurized BOG while filling. Conventional couplings have drawbacks such as freezing of the two cable lines (fuel station side and vehicle side) which again takes time to dismantle, and specialized equipment such as goggles and gloves are required to handle such couplings. This novel technology maintained the flexibility of the cable along with adequate insulation, and made the cable easier to mount and dismount. Both the counterparts (fuel side and vehicle side) has a normally closed ball valves. The valves open simultaneously when the both the counterparts are connected. When the valves open, there is a common air tight volume that is created that is thermally isolated from the environment. A 'cold finger' is inserted into this connecting space from the fuel station side. The connection is in the form of a co-axial cable with insulation on both the inner and the outer line. The innermost line transfers the LH_2 from the station to the tank of the vehicle. The outer cable is to guide the vent gas back to the station. Once filled, the cold finger is retracted back, causing the ball valves to close and disengage the coupling. To clean the common volume between the counterparts, gaseous helium is flushed manually [54].

While all the previously developed methods provide possible solutions to minimize boil-off, a comparative analysis will help identify the most effective method based on cost, efficiency and possibility to install in major applications [32].

2.5. Boil-off and Cryogenic energy integration schemes

Energy integration is characterized as an approach to harness the existing energy within a process to either heat or cool process streams. This approach enables a decrease in operational costs by minimizing the dependence on external utilities [55]. This section provides various methods of boil-off energy integration with other systems that require cooling.

Based on the present focus on hydrogen technology, seaborne shipping is considered as a possibility for transporting LH_2 in large scale. Considering the increased boil-off losses due to sloshing as explained in section 2.3.2, utilization of the boil-off energy is necessary. Donghoi and Stian [56] suggested the use of a Boil-off gas Handling System (BHS) that uses a fraction of the boil-off gas (BOG) as fuel for the ship and liquefies the remaining fraction using a Claude cycle based liquefaction system. Figure 2.11 shows the BHS integrated with the carrier LH_2 tank of the ship. It is assumed that this carrier is powered by a Proton Exchange Membrane Fuel Cell (PEMFC). Based on the feed requirement of the PEMFC, the remaining fraction is directed to a re-liquefaction system. The refrigeration system is also operated by a fraction of power generated by the PEMFC, thus avoiding the requirement of any additional power supply. It was observed that for low boil-off gas to fuel ratios, the liquefaction process consumed the majority of the total power generated, than the fuel compression system.

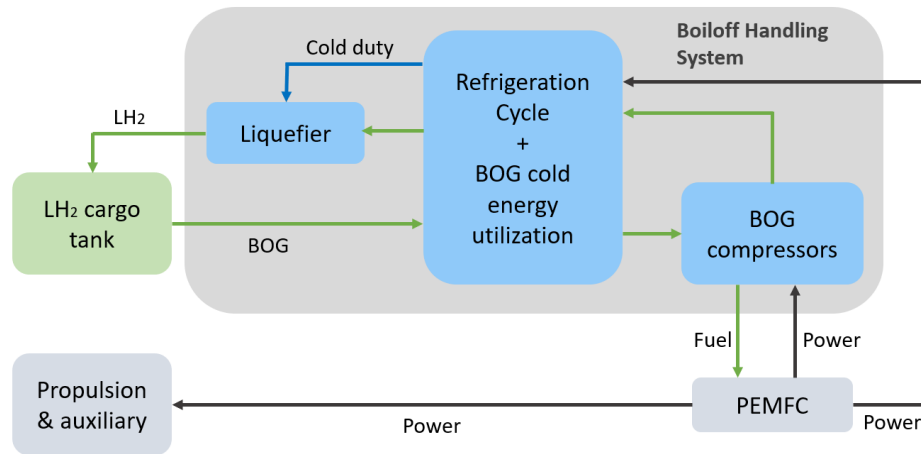


Figure 2.11: The boil-off handling system of an LH₂ carrier ship. The BOG energy is used as a cold utility in the refrigeration system. The BOG is then compressed. Part of the compressed BOG is fed to the PEMFC and the other part is re-liquefied. The illustration has been reproduced from [56].

When a H₂ vehicle having an LH₂ tank doesn't run for a while, the boil-off losses can be significant as the pressure keeps building over time to an unacceptable limit. Another technology by Linde involved a novel re-cooling system which they named 'CoolH₂' to utilize the cold energy of the boil-off. The surrounding air is sucked in, dried and liquefied by the released energy of the hydrogen when it gains heat. The liquid air then flows through a water-cooling jacket that surrounds the inner tank, acting like a refrigerator. This delays the temperature rise of the LH₂, and helps in utilizing the energy which would otherwise get lost with the boil-off. The tank size is not affected as this cooling jacket is adjusted in the insulation layer [54].

Another integration strategy, but for mitigating CO₂ emissions from industrial processes has been implemented by Air Liquide and Air Products, called the PORTHOS (Port of Rotterdam CO₂ Transport Hub and Offshore Storage) project. This involves capturing carbon using a cryogenic process named as Cryocap technology, and subsequently transporting it to designated CO₂ storage sites. The Cryocap technology involves a Pressure Swing Adsorption System that enriches the CO₂ from flue gas and then liquefies the CO₂ using a cryogenic process, the capture rate of CO₂ being 85-90% [57]. By adopting this approach, they aim to significantly reduce the environmental impact of their operations and contribute to sustainable practices in the industry. The PORTHOS project will help minimize emissions by 2.5 million tons of CO₂ per year, equivalent to 10% of the CO₂ emissions currently in the Rotterdam industry [58–60]. Although the fluid worked upon is CO₂ rather than H₂, the integration scheme of the cold energy derived from CO₂ boil-off, as a cold utility in this project can be applied, which has the potential to significantly decrease the overall energy consumption in the liquefaction process of CO₂.

2.5.1. Schemes for hydrogen boil-off capture

So far, the solutions were based on utilizing the cold energy of the BOG. However, there is still a significant quantity of pure H₂ that is lost, which could be stored for future and used as per requirement, such as in fuel cells. This section provides information on the previous research on the storage of the BOG for real time and future use.

The most obvious method to reduce the boil-off losses is by re-liquefaction of the BOG. The type of re-liquefaction process depends on the amount of BOG produced, the price of LH₂, requirements and availability of fuels, industrial gasses and electrical power, thermal energy, process complexity, operation of plant and vehicles, CAPEX and OPEX [18]. In all re-liquefaction processes, the BOG is initially compressed and precooled in a counterflow heat exchanger 'HX-1' as shown in Figure 2.12, using BOG from the reservoir and the Separator tank, to reduce the liquefaction work. The compression occurs at multiple stages with intercooling. After the final stage of compression, it is cooled back to ambient temperature using chillers, and then fed back to HX-1, where the pre-cooling takes place. An additional

refrigeration cycle is used to fully re-liquefy the BOG. The final step involves expansion using either a Joule Thomson expansion valve, that is shown in Figure 2.12, or an expansion turbine [18].

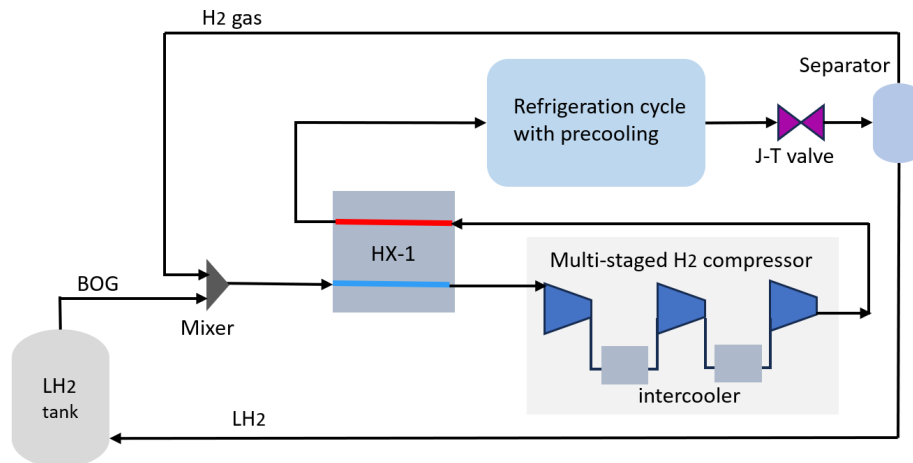


Figure 2.12: Re-liquefaction using Joule Thomson (J-T) expansion valve. A three staged H₂ compressor with intercooling is illustrated, that was reproduced from [18].

So far the methods discussed are feasible for boil-off capture in large scale stationary storage vessels, however there is a gap in the past research for capturing the boil-off in small scale transportable vessels such as for fuel tanks in aviation, on-road vehicles and sectors where LH₂ can be used as a fuel, with a compact and light boil-off management system.

2.6. Application of Hydrogen as an Aviation Fuel

In this thesis, the application of LH₂ as a fuel for aircraft propulsion is focused. There are currently two ways of generating power for propulsion in an aircraft: using solely internal combustion engines, solely fuel cell stack systems, or using a hybrid of the two. Airbus aims to launch the world's first hydrogen-powered commercial aircraft by 2035. The ZEROe project is exploring various configurations and technologies while also developing the necessary H₂ production and supply ecosystem [61]. The configurations involved are:

- Turbofan: Two hybrid-hydrogen turboprop engines provide the thrust, with the LH₂ storage and distribution system located behind the rear pressure bulkhead.
- Two hybrid-hydrogen turboprop engines with eight-bladed propellers are used to provide thrust. The LH₂ storage and distribution system is located behind the rear pressure bulkhead.
- Blended-Wing Body: Its wide interior offers various options for hydrogen storage and distribution. In this design, LH₂ tanks are located under the wings, and two hybrid-hydrogen turboprop engines provide thrust.
- Fully electrical concept: Revealed in the year 2020, this design is based on a fully electric propulsion system which is powered by fuel cells.

All four of the aircraft configurations designed under the ZEROe concepts are powered by hydrogen. In the case of hydrogen combustion, gas turbines will involve modifications in fuel injectors and the fuel systems are powered with hydrogen in a similar manner to how current aircraft are powered. The second method, hydrogen fuel cells, generates electrical energy which then powers electric motors that spin a propeller or fan. This is a fully electric propulsion system, different from the current propulsion systems on aircraft [61].

Hydrogen combustion engines operate by burning hydrogen in an internal combustion engine chamber modified to handle hydrogen's high-speed combustion. They function similarly to diesel engines but require specialized technologies, such as unique fuel injectors and ignition systems, to manage hydrogen's distinct properties effectively. For direct injection of hydrogen into the combustion chamber of the engine, a pressure greater than 100 bar is required to overcome the high in-cylinder pressure [62].

For this hydrogen compressors are required which would add extra weight and parasitic load on to the aircraft. Hydrogen fuel cells are more efficient than conventional internal combustion engines because they convert chemical energy directly into electrical energy, minimizing energy loss from heat [63].

Internal combustion engines typically have an efficiency of around 20%, whereas fuel cells can reach efficiencies between 40-50% or even higher under specific conditions. Therefore, assuming a 40% efficient PEMFC stack, we would only need to carry half as much fuel to power an aircraft with the same performance and range [64]. Fuel cells, particularly PEMFCs contain polymer electrolytes that operate efficiently at low temperatures, enabling rapid startup of PEMFCs. The thin membrane electrode assemblies allow for the fuel cells to be compact. Additional benefits include the absence of corrosive fluid hazards and the capability to function in any orientation. These features make PEMFCs particularly-suited for vehicular and portable applications [65]. PEMFCs can be categorized as per its operating temperature range, where Low Temperature Proton Exchange Membrane Fuel Cells (LT-PEMFC) operate between 323K-363K, and High Temperature Proton Exchange Membrane Fuel Cells (HTPEMFC) operate between 393K-473K, with operating pressures between 1-6 atm [66]. Under pure hydrogen operation, at lower atmospheric pressure operations and practically operable cell voltage between 0.5-0.7, LTPEMFC show a greater performance than HTPEMFC [67]. HTPEMFCs have a higher temperature range and a greater ΔT with the ambient, and research on their application in aviation is not as advanced as that for LTPEMFCs [68]. Therefore, only LTPEMFCs have been focused in this thesis.

In June 2023, Airbus announced the successful completion of its hydrogen fuel cell system test campaign, which achieved a full-power level of 1200 kW. The test involved an iron pod that contained the electric motors that spin the propellers and power the control and cooling systems. This milestone represents the most powerful fuel cell test ever conducted in aviation for large-scale aircraft, and setting the scope for the next major step which is to integrate the entire propulsion system with the electric motor. The tests will continue in the iron pod throughout 2024, and after completion the next step would be to size, optimize and qualify the propulsion system as per flight specifications [69].

Following Table 2.2 provides the details of a PEMFC obtained from the paper by Ryan.

Table 2.2: LTPEMFC Composition and operating parameters obtained from [70].

Parameters	PEMFC
Electrolyte	Nafion Polymer membrane
Charge carrier	H ⁺
Catalyst	Platinum
Cell Components	Carbon based
Operating temperature range (K)	323 - 363
Operating pressure (bar)	1.5
Average Cell voltage (V)	0.7

The half equations at the anode and cathode involved in the electrochemical reactions are shown below in equations 2.18 and 2.19 respectively. The electrons released in the anode are transferred through the electrical circuit and the H⁺ ions are transported through the polymer membrane electrolyte towards the cathode where they combine with the oxidant to form water.



Multiple fuel cells are serially joined to form a stack as shown in the cut section of the fuel cell stack in Figure 2.13 that was reproduced from [71]. There are cooling channels where the coolant passes in between the bipolar plates connecting two consecutive fuel cells. The gas diffusion layer, which is a porous structure on both sides of the cell ensures that the reactant gases (hydrogen and oxygen) are uniformly distributed across the catalyst layer. This uniform distribution is responsible for efficient operation of the fuel cell, as it ensures that the electrochemical reactions occur consistently across the entire active area of the cell.

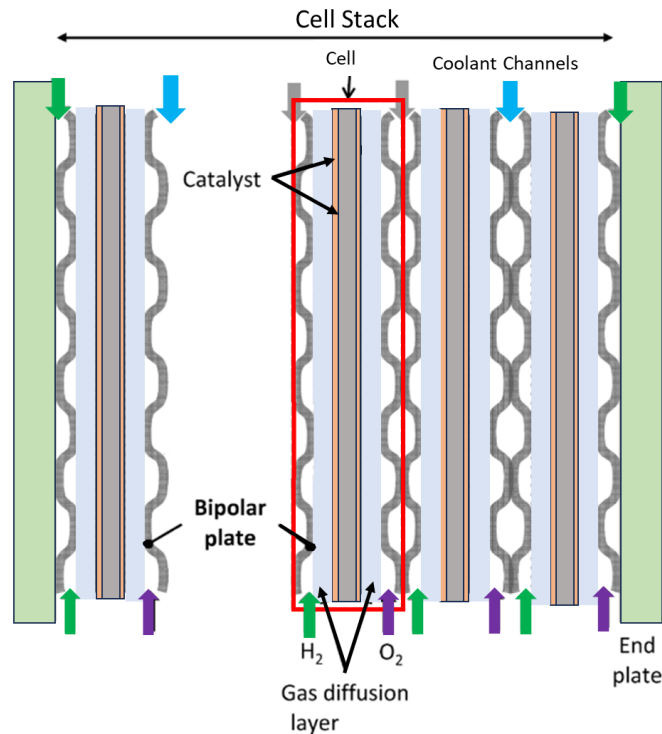


Figure 2.13: Illustration of cut section of the fuel cell stack showing the membrane electrode assembly. The coolant channels are in between the reactant channels, inside the bipolar plates of 2 consecutive cells.

When it comes to fuel cells, its performance depends on Gibbs free energy. This is basically the available energy to do external work, without considering any work caused by changes in pressure or volume. Within the operating range of the fuel cell, the performance improves when the operating temperature is near its higher limit for a fixed operating pressure and higher operating pressures for a fixed operating temperature. The performance of a fuel cell can be understood from its polarization curve, where the average cell voltage is empirically obtained at different current densities for a set of operating pressures at a fixed operating temperature. The current density is obtained by normalizing the current per unit area. High altitude conditions affect the performance of a fuel cell through a complex set of chemical, physical and electrochemical processes [72]. The Figure 2.14 shows the polarization curve of an LTPEMFC operating at 353K for a range of operating pressures between 1 bar and 4 bar and the corresponding fuel cell heat flux generation with respect to the current density, which was reproduced from [72, 73]. Practically sub-atmospheric operating pressures of fuel cell is avoided through the compression of air and fuel. Understanding the effect of higher flight levels on fuel cell performance is important due to the complexity of the electrochemical and physical processes that can be related to the cell voltage, as stated in the Appendix section A.3.

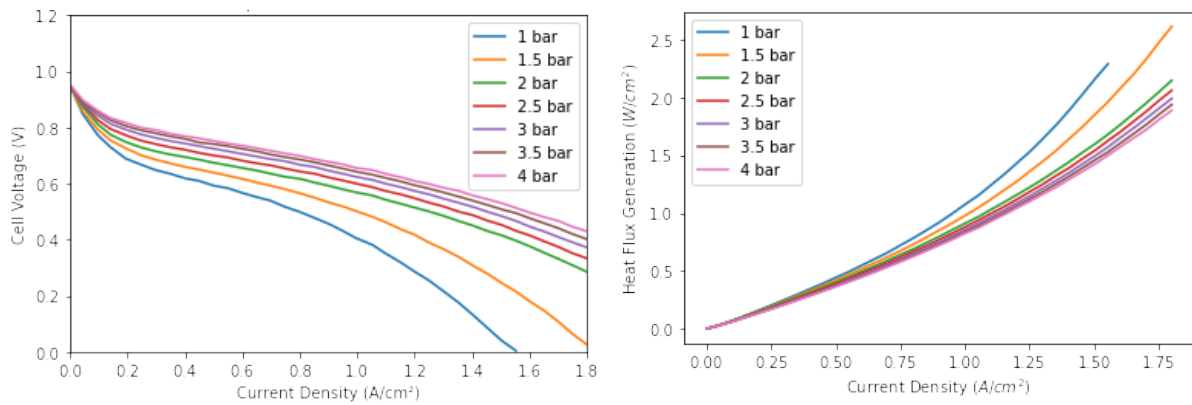


Figure 2.14: Fuel cell performance variation with pressure at 353 K operating temperature, showing a high cell voltage at higher pressures. The left image shows the polarization curve of fuel cell giving the average cell voltage (V_c) for different operating pressures at cell temperature of 353K, reproduced in Python environment [73]. The right figure shows the fuel cell heat flux obtained using the heat generation equation [$\dot{q} = (V_{\max} - V_c) \cdot \dot{I}$] of a fuel cell with respect to current density (\dot{I}) with units in (A/cm^2), where (V_{\max}) is the maximum cell voltage. The equations were obtained from the book in [65].

The voltage output of a real fuel cell is less compared to the thermodynamically predicted voltage output, the fraction of which is released as heat, due to entropic heat of reactions and irreversibilities. Some of them include activation losses, Ohmic losses and concentration losses. Activation losses are linked to electrochemical reaction kinetics and the necessity of charge buildup at the electrode reaction site to propel the reaction forward. The energy needed to initiate the charge transfer process at the reaction site is lost and does not contribute to the actual voltage achieved [74]. Ohmic losses are due to electronic resistances through conductors and ionic resistances against proton flow through the membranes. Concentration losses are due to mass transfer of hydrogen to the anode causing reactant depletion, when its requirement is more than supply. The amount of heat generation of a fuel cell is determined by comparing it with a fuel cell of 100% efficiency, that has a maximum voltage of 1.48 V based on the HHV of H_2 , that is when the product water is generated in liquid form, and 1.25V based on the LHV of H_2 , that is when the product water is generated in vapor form [75]. Internal combustion engines that use the lower heating value (LHV) of the H_2 , have high reaction temperatures that make it evident for the product water to be vaporized. However, when it comes to LTPEMFC having operating temperatures below the boiling point of water, there are chances of the product being in liquid phase more than in vapor phase. That increases the cooling requirement of the fuel cell because the possibility of cooling provided by product removal due to the latent of vaporization of water is diminished.

2.7. Research Gap

To conclude, this literature survey revealed a diverse range of methods and technological advancements that were aimed at mitigating liquid hydrogen boil-off and utilizing the boil-off energy. A significant research gap was noticed in reducing H_2 losses during storage in liquid form:

- There is a requirement of novel ideas for cryogenic cold integration in aviation systems which will involve the design of effective energy integration techniques such as customized heat exchangers that are compact and efficient for capturing cryogenic cold.
- More compact and efficient zero boil-off systems are required in the aviation sector rather than using heavy and power consuming active cooling methods.
- An integration method for boil-off is required that can prevent the venting of the hydrogen due to pressurization of the tanks.
- Better boil-off models need to be implemented to involve each phenomenon occurring in the tank such as thermal stratification and dynamic phenomena in detail such as dynamic condensation blocking.
- Further applications are needed to be explored for the utilization of the cold energy of the BOG such as a heat sink.

As the search continues, this section will serve as a base for the upcoming research work.

3

Methodology

This section presents a methodology for predicting the boil-off rate, and designing a system to utilize LH₂ as an aviation fuel, focusing on the possibility of novel integration of boil-off vapor and the fuel's cryogenic cold into the thermal management system of the LTPMFC. Figure 3.1 presents a flowchart with the steps followed to reach the research objectives of this thesis.

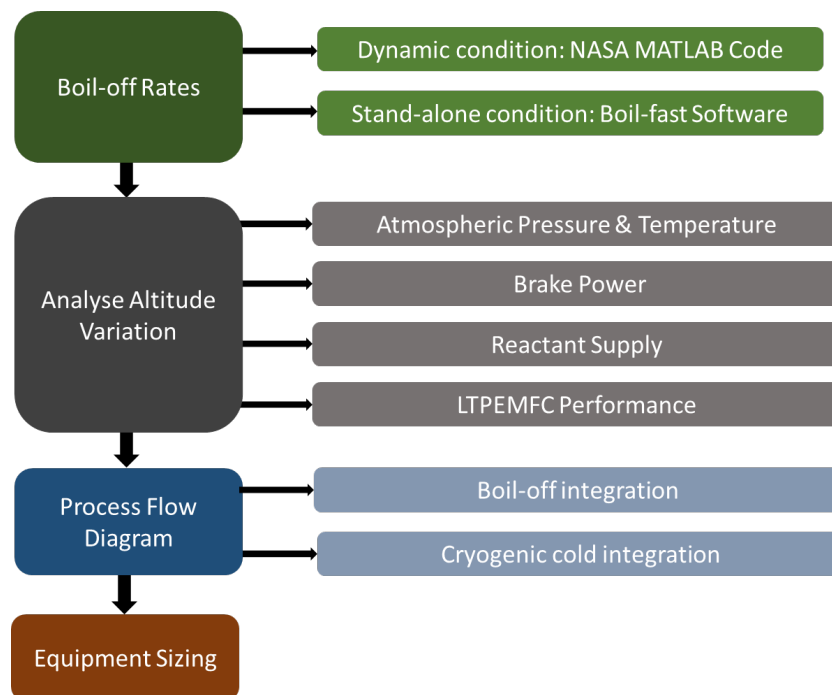


Figure 3.1: Flowchart showing steps undertaken for the boil-off capture and cold integration. Starting from predicting the boil-off, understanding the fuel cell performance and heat load and selecting the worst case scenario (maximum fuel cell operating point during take-off), designing systems for capturing the boil-off vapor and integrating the cryogenic cold, sizing the components involved in the cryogenic cold integration.

The design was initiated by quantifying the most uncontrolled phenomenon which is the boil-off rate. Ambient was considered to be the highest temperature recorded, 55°C as during a heat wave of 55°C experienced in Africa in 1931, 54°C in Iran back in 2017 [13], 52°C in New Delhi, India in 2024. Since the boil-off rates in a dynamic tank differ from a stationary tank, they were individually obtained. The dynamic condition was only considered during tank filling and a stand-alone tank was considered for the entire journey.

3.1. Hydrogen Supply

Unlike compressed gaseous storage at nearly 700 bar, LH₂ is stored at a lower pressure of around 1.5 bar, which reduces the gravimetric index of the fuel tank as higher operating pressure requires thicker pressure vessel walls to withstand the increased structural loads, resulting in heavier pressure vessels and a greater overall system weight [76]. This thesis considers a supply pressure of 1.5 bar, which is same as the operating pressure of the LTPEMFC, to reduce pumping power. An LH₂ fuel tank not only stores potential chemical energy for the fuel cell reaction, but also thermal energy (cryogenic cold) that can be obtained from the supply stream. It therefore satisfies two roles: as a reactant supply to the LTPEMFC, and as a partial heat sink in the thermal management system of the LTPEMFC. Although the supply pressure of hydrogen matches the operating pressure of the LTPEMFC, the hydrogen is still at its cryogenic state after it is tapped from the LH₂ tank. As the operating temperature of the LTPEMFC is 353 K, the hydrogen needs to be heated to its operating temperature. Rather than using a separate heating system that would consume power during the journey, the heating is provided by the thermal management system of the fuel cell.

A vertical cylindrical tank of volume 5m³, with height of 1.5m and diameter of 2.06m was selected, that would fit inside a standard flight fuselage. The tank shape selected is a cylinder because it has a larger surface area to volume ratio than a sphere, resulting in greater heat ingress and a high boil-off rate for the system design to robust. Also, when a vertical cylinder is used, it is less complex to model the pressure balance of the tank through vaporizer as the drop in fuel level during supply is directly measurable due to the uniform cross section along cylinder height. For maximum gravimetric efficiency, the number of tanks in an aircraft should be minimised and their geometries should be close to spherical or low aspect ratio cylinders for thermal and structural advantages [77].

As boil-off is continuous, the BOG integration applied here is only possible for H₂ fuel based transport where the fuel is in continuous use, such as for a particular journey of an LH₂ powered aircraft. The conditions that need to be satisfied for the integration system to work are that the entire fuel should be used up in 1 journey or the residue will need to get vented/ redirected to a separate storage, the tank will need to get refilled before start of next journey, and the transport should not be parked for more than the dormancy time of the fuel tank for the set pressure relief threshold. Dormancy time refers to the duration it takes for the tank to reach a specified pressure when there is no fuel flow into or out of the tank [77]. The aviation industry would be particularly suitable to apply the work of this thesis. If this system is considered for the maritime industry, a separate study needs to be considered on the effect of sloshing and its management as it is more dominant in cargo ships and the travel journeys are longer causing greater LH₂ holding times.

3.1.1. Modelling boil-off while tank filling

The dynamic conditions of the tank were modelled in MATLAB version R2023b. This was achieved by scaling down a large 12.5m³ LH₂ storage dewar situated at the Lawrence Livermore Cryogenic Hydrogen Test Facility, to a 5m³ aircraft fuel tank as shown in Figure 3.2, using an existing code provided by Petitpas in [23]. This code was a modified version of a MATLAB code originally developed by NASA. It is used to simulate the thermodynamic changes of two tanks (horizontal cylindrical transferring trailer named 'ST' in the code and vertical cylindrical receiving dewar named 'ET' in the code), during the transfer of LH₂ to the dewar. The code was applied in the fuel tank filling system by considering the receiving dewar to be the fuel tank.

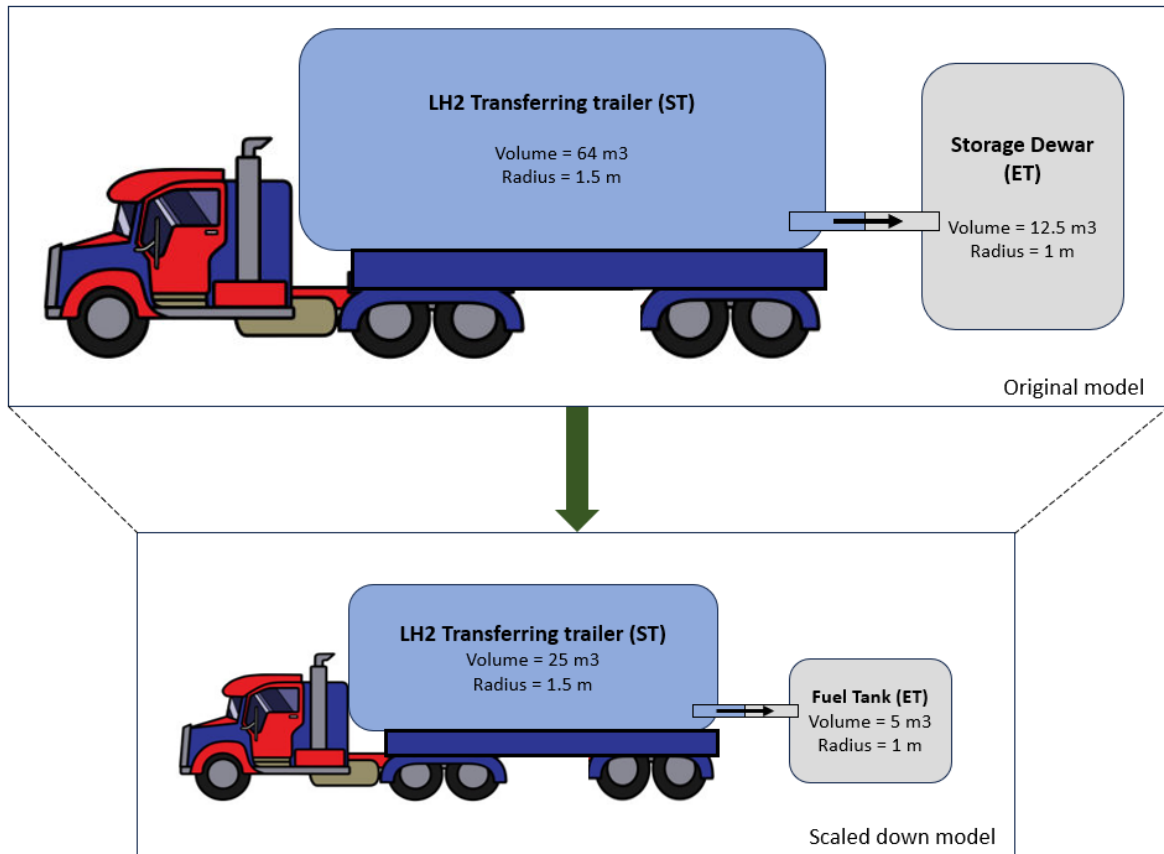


Figure 3.2: Illustration of the models of LH₂ transfer used in the original code and the scaled down version used for aviation. Original model shows the transferring and receiving vessels involved in large scale stationary storage of 12.5m³ used in the Petitpas's original code. Scaled down model shows the transporting trailer and receiving fuel tank of the aircraft.

The Petitpas's MATLAB code used Benedict-Webb-Rubin real gas equation of state and the transport properties of the fluids were obtained by connecting REFPROP database with MATLAB [23]. No modifications were further made in the equations of states since it would be difficult to validate the model. The code manually inputs initial conditions such as initial tank pressure, liquid, wall and vapor saturation temperatures, total liquid mass level and also conditions that are derived from REFPROP such as the initial thermophysical and material properties like density. The geometrical parameters, properties and constants are provided in Table 3.1, the initial conditions are provided in Table 3.2, and the boundary conditions are provided in Table 3.3.

Table 3.1: Geometrical and grid parameters of the transferring vessel and the fuel tank that were changed in the MATLAB code to suit the requirement for obtaining boil-off rate in 5m³ fuel tank. Based on the original code, the nomenclature of the vessels are: ST = Transferring trailer, ET = Fuel tank.

Numerical Parameters	ST	ET
Volume (m ³)	25	5
Radius (m)	1.5	1
Length (m)	3.5368	1.5915
number of grid in liquid (m)	5	5
number of grid in vapor (m)	5	6
Liquid grid time constant (s)	0.01	0.001
Vapor grid time constant (s)	0.01	0.001

Table 3.2: Initial conditions of the transferring vessel and the fuel tank that were changed in the MATLAB code to suit the requirement for obtaining boil-off rate in 5m³ fuel tank. ST = Transferring trailer, ET = Fuel tank.

Initial Conditions	ST	ET
Initial pressure (bar)	1	1.49
Liquid temperature (K)	20.4	20.4
Total mass of liquid and vapor (kg)	1586	0
Initial wall temperature (K)	-	21
Initial liquid volume (m ³)	22	0

For flow to take place from the trailer (ST) to the fuel tank (ET), a pressure difference needs to be created. This can either be done mechanically using a pump or thermodynamically by increasing the vapor pressure of ST. The code creates the flow pressure thermodynamically using an inbuilt vaporizer in the trailer. The initial pressure of the trailer (ST) is shown as 1 bar which is below the initial pressure of the fuel tank (ET) because at the start of the simulation, the vaporizer in ST had not yet built up the flow pressure. The initial fuel tank's pressure (ET) was kept just below 1.5 bar which is the final pressure of the tank after completing supply to the fuel cell at the end of the journey and before the tank gets refilled. The grid parameters such as grid size and time constant were initially set up as per the original code, which caused failure in convergence of the results. One at a time, the time constant was reduced by a factor of 10 and the grid number was increased by a factor of 1 and checked for convergence. Manual input of grid parameters is one of the drawbacks of the code and gave numerical errors when the time constant was larger than 0.001 and the number of grids less than 6 for ET. The step size was then selected when the results showed a similar trend when compared to the original code results, and changed no more when the parameters were further altered. The model does not account for the tank insulation and the energy balance is conducted in the tank after the heat flux has crossed the insulation. A fixed heat flux condition that is a Neumann boundary condition was imposed by first obtaining the maximum of the heat flows during summer time, that is 70 W from the ambient heat variation graph provided in [23]. The heat flow was divided by the surface area of the large storage tank of 12.5 m³ to get the heat flux, and this same flux was multiplied by the surface area of the 5 m³ fuel tank to obtain the total ambient heat flow of 36.64 W into the fuel tank.

Table 3.3: Boundary conditions of the transferring vessel and the fuel tank that were changed in the MATLAB code to suit the requirement for obtaining boil-off rate in the 5m³ fuel tank. ST = Transferring trailer, ET = Fuel tank.

Boundary Conditions	Value
Pressure Relief Upper threshold (ST) (bar)	4.2
Pressure Relief Lower threshold (ST) (bar)	4.13
Final venting pressure (ST) (bar)	2
Pressure regulator Set pressure (ET) (bar)	1.7
Pressure regulator Lock-up pressure (ET) (bar)	1.9
Heat flux (W/m ²)	2.27
Heat flow (W)	36.64
Maximum fraction of ET to complete fill	0.9

For the case of a pressure relief valve settings of the trailer (ST), the upper threshold is the set pressure at which the pressure relief valve opens to release excess pressure. It is designed to protect the system from over-pressure by allowing fluid or gas to escape when the pressure exceeds this limit. The lower threshold also called as the reset pressure is at which the pressure relief valve closes after having opened to release excess pressure. It is usually set slightly below the set pressure to ensure that the valve does not continuously cycle open and close, which could lead to wear and failure. There are 2 pressure regulator valves connected to the fuel tank as shown in Figure 3.3. The pressure regulator valve in Table 3.3 that opens during the fill of the fuel tank (ET) is the valve located in the BOG retrieval line (5). The set pressure is 1.7 bar which is the desired outlet pressure that the regulator is adjusted to maintain. This will again depend upon the downstream system which follows line (5) to capture and store the dynamic hydrogen boil-off. As this section provides details on the MATLAB model, for explanation on the design of the entire fuel supply system, the sub-section 5.2.1 can be referred.

①	LH2 Fuel tank
②	LH2 Charging port
③	Pressure relief valve
④	Pressure Regulator valve
⑤	BOG retrieval line during tank Filling
⑥	Vaporizer valve
⑦	Pressure and Temperature Sensors
⑧	LH2 Transfer Line valve
⑨	Optional LH2 Pump
⑩	LH2 Vaporizer
⑪	Hydrogen vapor Mixer
⑫	Non-return valve
⑬	Manually controlled valve
⑭	Flowmeter
⑮	Isolation valves

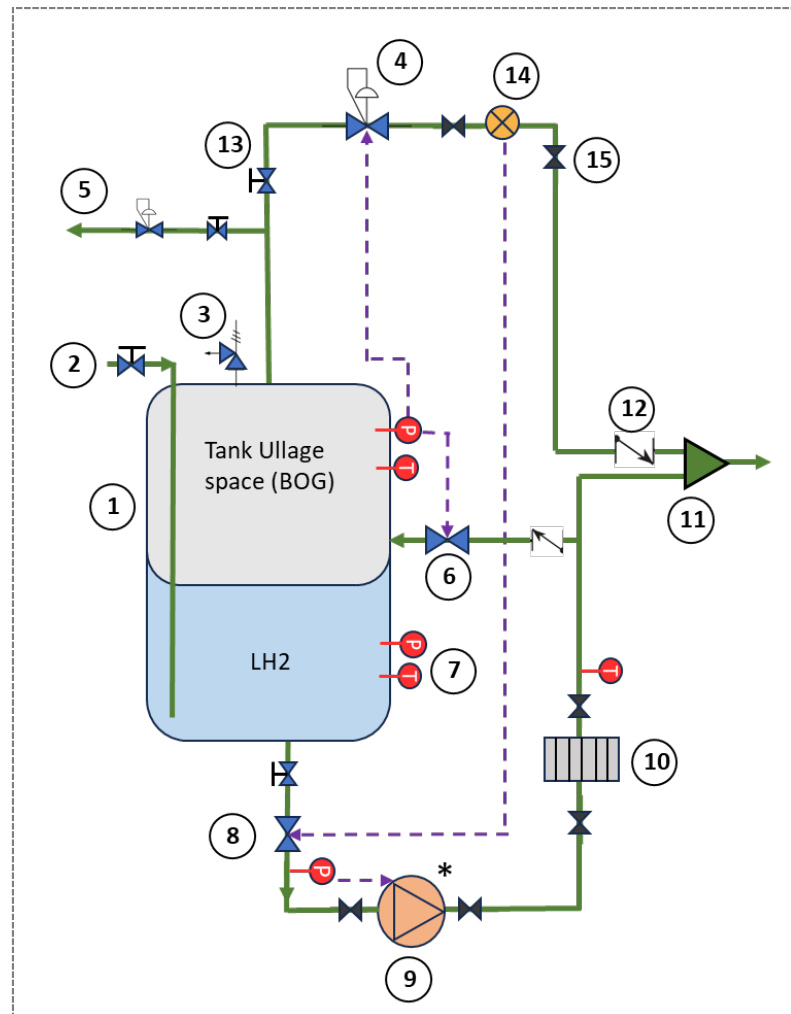


Figure 3.3: Fuel supply system of the aircraft with Fuel tank (ET) shown as '1' that will be situated inside the fuselage. The path taken by the BOG during filling of the tank is through the pressure regulator shown in line '5', as the manual valve '13' is closed. The pressure relief valve '3' has a threshold higher than the lock-up pressure of the regulator.

The maximum fraction of the fuel tank's volume to complete filling is set to 0.9, meaning that the tank's ullage space at fully loaded condition is 10%. The fuel tank also has a pressure relief system set at a higher pressure than the lock-up pressure of the pressure regulator. As this system has a zero boil-off loss, it means that the pressure relief valve of the fuel tank will never open due to tank pressurization under normal ambient during the entire journey of the flight, and therefore it has only been provided as a safety measure. The final venting pressure in the transferring trailer was kept higher than the fuel tank's set pressure in order to maintain the flow while filling the tank.

The numerical solver used was an ordinary integro-differential solver ODE15s, where the differential part was used to find the rate of change of quantities such as the specific internal energies of liquid and vapor space, change in the temperature of the liquid, vapor and the wall of the fuel tank. The spacial discretization is done using the Central Difference method of the Finite Difference scheme inside the boundary layers. The integral part is an Explicit Time Integration scheme used to obtain the data of the new time step using the previous time step. The code uses a 0D (quasi-dimensional) model which does not account for temperature distribution, except within the boundary layers on either side of the saturation film. Additionally, the volume and mass of hydrogen in the pipes are not considered. The model assumes no pressure drops through the pipes and perfect insulation throughout the system. The wall temperature of the fuel tank is assumed as uniform.

There is always a possibility to edit the MATLAB code to obtain the boil-off rate for a stand-alone tank

system, by toggling off the switch that closes the transfer line between the trailer and fuel tank. However, altering a numerical code and relying on its boil-off rate results would lack validation. Therefore, another software called BoilFAST is used for obtaining the boil-off rate for the tank system after it has been filled with the fuel. BoilFAST is a specialized computational tool developed by the Future Energy Exports Cooperative Research Centre (FEnEx CRC) to simulate boil-off production by choosing from a range of available fluids, including equilibrium hydrogen, and by specifying tank designs with heat flow or insulation details. BoilFAST predicts the amount of boil-off generated over a specified period and its impact on critical operational parameters such as storage tank pressure, liquid and gas levels along with compositions, and venting rates. The model has been extensively validated against industrial tests and laboratory data published by NASA and the University of Western Australia for both hydrogen and LNG [78].

3.1.2. Modelling boil-off at Stand-alone Condition

This sub-section models the boil-off rate after the filling is complete and during the flight journey, when the tank is free of any dynamic effects. In this thesis, the effect of flight turbulence on boil-off rate has been neglected and is expected to be studied in upcoming research. The manual valve of BOG retrieval line (5) in Figure 3.3 is closed and the manual valve (13) is opened and the BOG passes through the pressure regulator (4) as a the fuel cell anode supply. The set pressure of the pressure regulator (4) is 1.5 bar, which is same as the fuel supply pressure. When the initial pressure of the tank is also 1.5 bar due to a specific holding time of the fuel after filling and before supply, the system acts like an open-tank configuration.

Predicting the boil-off rate without dynamic effects is conducted in a separate software called BoilFAST [v1.1.0]. Since this condition is met after the fuel is filled into the fuel tank and for the rest of the journey, the initial conditions of this simulation should match with the final tank pressure from the MATLAB simulation. The insulation thickness is fixed to a value of 0.01m. The boil-off rates using different holding times of the LH₂ in the tank is obtained, and the holding time which resulted in a boil-off rate lower than the minimum H₂ supply requirement in the fuel cell is noted. The boil-off rate results are presented under the section 5. Table 3.4 and 3.5 show the conditions used for simulating the boil-off using BoilFAST software. The initial liquid surface pressure refers to the pressure at the surface of the liquid fuel within the tank. This is equivalent to the vapor pressure of the liquid at the given temperature, assuming the tank is in equilibrium with the 10% ullage space above the liquid. The relief pressure settings mentioned in the BoilFAST GUI are used as the set pressure of pressure regulator (4). For the composition of the hydrogen, 100% parahydrogen is considered, as the ortho-para conversion occurs in the order of a few days, where as the duration of the flight is in the order of a few hours. The initial tank pressure was kept same as the pressure regulator set pressure.

Table 3.4: Conditions used in BoilFAST simulation showing a 100% parahydrogen composition with initial liquid surface pressure same as the regulator set pressure.

Parameters	Values
Fluid name	ParaHydrogen
Mass Fraction	1
Initial liquid surface pressure (bar)	1.5
Vapor Temperature (K)	Equal to Liquid Temperature
Pressure regulator set pressure (bar)	1.5

Table 3.5: Fuel tank dimensions considering vertical cylindrical tank with flat end caps and 90% loaded fuel.

Parameters	Values
Volume (m ³)	5
Initial liquid volume (m ³)	4.5
Inner diameter (m)	2.06
Insulation thickness (m)	0.05
Cylinder height (m)	1.5

The BoilFAST simulation was compared to the past research with 3 different laboratory case studies performed by ‘NASA Liquid Hydrogen Self-Pressurization Tests’ on a 4.8 m³ tank volume, using 3 different heat fluxes: 0.35, 2, 3.5 W/m². The values of the liquid-ambient and vapor-ambient heat transfer coefficients were recorded for each heat fluxes. The liquid-vapor heat transfer coefficient was considered as 1.04 W/m² for all cases, therefore it was also kept same for this simulation. The heat flux exposed by the fuel tank was calculated at 55°C ambient by interpolating the results from Figure 3.4 and the heat transfer coefficient was obtained. The heat transfer settings are provided in Table 3.6.

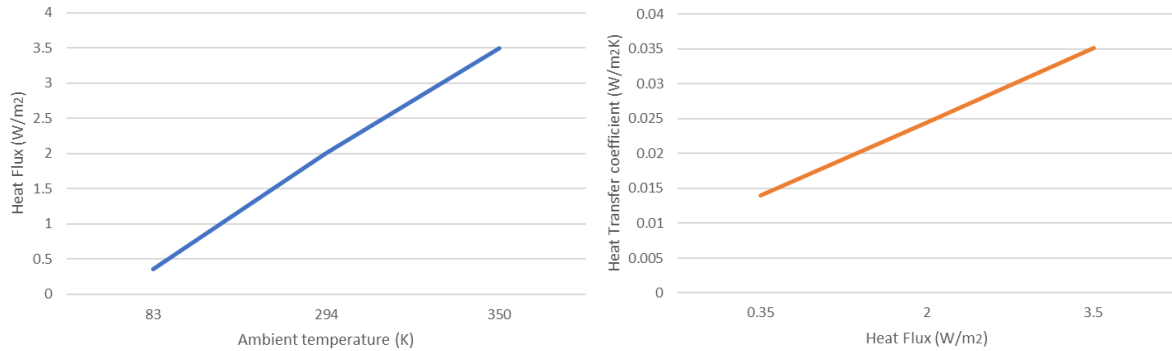


Figure 3.4: Graphs showing trend of heat flux (left image) and heat transfer coefficients (right image) used in BoilFAST LH₂ self-pressurization tests conducted by NASA at different ambient conditions. A linear trend shows that linear interpolation is valid to find the heat transfer coefficient.

Table 3.6: Heat transfer settings used in the BoilFAST simulation after interpolating the results from NASA Liquid Hydrogen Self-Pressurization Tests.

Parameters	Values
Ambient Temperature (K)	328
Heat transfer coefficient liquid-ambient (W/(m ² .K))	0.0309
Heat transfer coefficient vapor-ambient (W/(m ² .K))	0.0309
Heat transfer coefficient vapor-liquid (W/(m ² .K))	1.04

The simulation time duration was considered for 1 hour with time steps of 10 seconds, based on a short ranged flight duration which is the amount of time that 319 kg of LH₂ with density 70.85 kg/m³, stored inside the 5m³ tank can supply at a certain rate for the entire duration. The rate of hydrogen supply requirement is provided under sub-section 3.2.

3.2. Power Generation

For the propulsion system used in this study, the aircraft of Bombardier Dash 8 Q300 specifications were selected, whose dimensions have been provided in Section A.6. There are 2 Pratt & Whitney PW123 turboprop engines. 1800 kW brake power is delivered by each engine. Each of the two propulsion units, contain 4 fuel cell stacks of 600 kW gross power per stack, 2 of which are cooled by ram air heat exchangers, assuming that the heat exchangers are attached on both sides of the aircraft nacelle (outer casing or housing of the engine). 12.5% of the full stack power (300kW at maximum operation) is considered for balancing the parasitic power to run auxiliary systems. It means that the allowable parasitic load is 300 kW, which is to provide power to the power consuming components like compressors, pumps and other avionics. The remaining 2100 kW is left to compensate for a minimum brake thermal efficiency of 85.7% to deliver the required propulsion power. Availability of excess power at lower loads can be used up by the 2nd propulsion unit or in auxiliary components.

A work carried out in a Master of Science Thesis from the Aerospace Department of TU Delft, supervised by Prof. Dr. Ir. P. Colonna and Dr. Ir. C.M. de Servi [79], involved the design of these ram air cooled heat exchangers. As it has already been designed, this thesis will only involve ways to

incorporate the cryogenic cold in reducing the parasitic load and weight of the ram air-cooled thermal management system. As the cryogenic cold of the entire H₂ reactant stream for one propulsion unit is utilized, the mass flowrate of the supply H₂ is considered based on the total power generation of the fuel cell stacks in the propulsion unit (2400 kW), and the heat load calculations are done based on the gross power of the ram air-cooled stacks (1200 kW).

For this study, considering the maximum power generation during takeoff, the reactant supply calculations are done based on the total fuel cell stack power output for each propulsion unit $P_{out} = 2400000$ W. A simple fuel cell reaction shown in equation 3.1 uses stoichiometric quantities of reactants to obtain just the right amount of products. However in practical cases, the stoichiometric ratio of hydrogen (λ_{H_2}) is kept between 1.2 to 1.5 with a recirculation stream, and the stoichiometric ratio for air (λ_{air}) is 2, based on the information provided in [80].



Since 4 electrons are transferred for each mole of O₂, the mass flowrate (kg/s) of oxygen is obtained by the following equation.

$$\dot{m}_{O_2} = \frac{M_{r(O_2)} \cdot P_{out}}{4 \cdot V_c \cdot F} \quad (3.2)$$

Since the fuel cell used is an air-breathing system, it is more practical to calculate the mass flowrate (kg/s) of air supply.

$$\dot{m}_{air} = \frac{\lambda_{air} \cdot M_{r(air)} \cdot \dot{m}_{O_2}}{M_{r(O_2)} \cdot x_{O_2}} \quad (3.3)$$

where M_r is the molecular weight (kg/mole) of the substance provided in its subscript, x_{O_2} is the fraction of O₂ present in air, which for ground case would be nearly 0.21. Due to the non-stoichiometry, the mass flowrate of unused exit air removed is as follows:

$$\dot{m}_{air(unused)} = \dot{m}_{air} - \dot{m}_{O_2} \quad (3.4)$$

The required quantity of H₂ fuel supply (kg/s) is calculated by:

$$\dot{m}_{H_2} = \frac{\lambda_{H_2} \cdot M_{r(H_2)} \cdot P_{out}}{2 \cdot V_c \cdot F} \quad (3.5)$$

where V_c is the average cell voltage which ranges between 0.6 - 0.7 V [65], which in this study is considered to be 0.7 V. F is the Faraday's constant considered as 96500 C/mol.

The fuel cell humidification system design is not within the scope of this thesis. The results for the reactant supply requirements at maximum operating point for a power generation of 2400000 W have been provided in Table 5.1 under section 5.1.

3.2.1. Fuel Cell Heat Release

The exothermic reactions involved in the electrochemical processes and irreversibilities of the fuel cell such as due to inefficiencies in the fuel cell system, including the over-potential at the anode and cathode, as well as the resistive losses in the membrane and other cell components, as mentioned in the section 2.6, release a significant amount of heat that can alter the temperature of the fuel cell beyond its operating temperature. Effective heat management is crucial in LTPMFCs to maintain optimal performance and prevent thermal degradation of the cell materials. Figure 3.5 illustrates a Sankey diagram that can be used to visualize and compare the energy generated by the fuel cell, and the fraction of the energy that is available for propulsion and lost as heat.

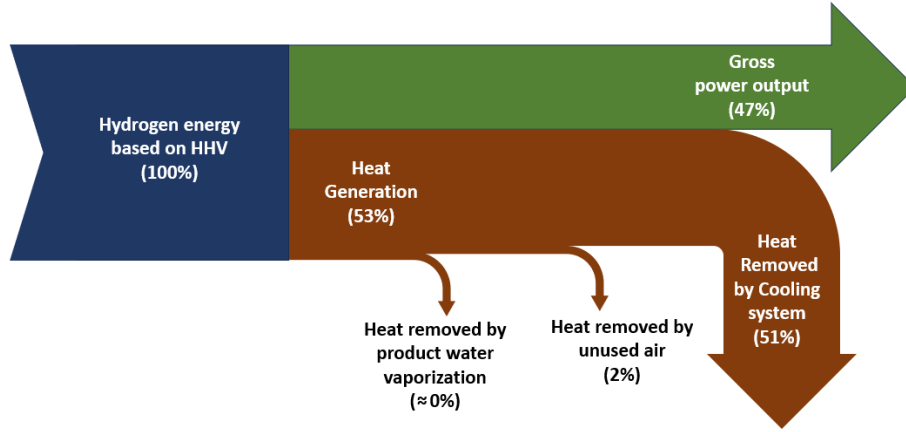


Figure 3.5: Sankey diagram illustrating the fraction of energy that flows from fuel cell energy generation to gross power output of 47% that is equivalent to the fuel cell efficiency, and 53% as heat, out of which 2% heat is removed by the unused air. The heat removed by vaporization of water is considered near to 0% as for an LTPEMFC the product water is expected to be in liquid state with negligible sensible heat removal.

While a fuel cell performs better at higher temperature, excess heat can cause thermal degradation of the fuel cell. The heat generation also depends highly on the state of the product water being formed. Water formation can occur in two possible energy states: (i) the higher heating value (HHV), where the product water is in liquid form, and (ii) the lower heating value (LHV), where the product water is in the form of uncondensed vapor or steam. The difference between these values represents the latent heat of evaporation of water. In the fuel cell reaction, the HHV is approximately 18% higher than the LHV . In an LTPEMFC, the product water is generally liquid [81]. Therefore water as 100% liquid will give the maximum heat generation of the fuel cell.

$$P_{\text{stacks}} = V_c \cdot I \cdot n \quad (3.6)$$

where n is the number of cells in a stack, range from 400 to 600 usually for automotive applications [82]. Since this stack power P_{stacks} is obtained from the average measurable cell voltage of 0.7 V, which is the voltage when the cell works at a 47% efficiency, and which is less than the 100% efficient cell voltage of 1.48V, the cell efficiency is taken into account in the equation 3.6. To obtain the brake power that spins the propeller, the shaft efficiency is applied as a factor of the fuel cell output power. This shaft efficiency is not involved in the fuel cell heat generation but is involved in the frictional heat developed in the shaft. As this thesis is concerned about only the thermal management system of the fuel cell stack, only the cell efficiency is taken into account and not the shaft efficiency.

The heat generated by the fuel cell considering the HHV value is as follows:

$$Q_{\text{stacks}(2)} = P_{\text{stacks}(2)} \cdot \left[\left(\frac{HHV}{V_c} - 1 \right) \right] \quad (3.7)$$

where $P_{\text{stacks}(2)}$ is the maximum power generated by 2 of the ram air-cooled stacks (1200 kW). A part of the heat generated is taken out directly by the unused air by its changing enthalpy. Assuming at ground level the inlet temperature of the air is same as the high ambient of 328K, and the outlet temperature of the unreacted air is same as the operating temperature of 353K, then the enthalpy removed by the unused air is:

$$Q_{\text{air(used)}_2} = \left(\frac{\dot{m}_{\text{air(used)}}}{2} \right) \cdot C_{p(\text{air})} \cdot (353 - 328) \quad (3.8)$$

where $Q_{\text{air(used)}_2}$ is the amount of cooling provided by air entering in the 2 ram air-cooled stacks out of the 4 stacks. The resultant cooling load required to cool the fuel cell to its operable temperature is given by:

$$Q_{\text{stacks(net)}} = Q_{\text{stacks}(2)} - Q_{\text{air(used)}_2} \quad (3.9)$$

where $Q_{\text{stacks}(\text{net})}$ in (W) is the cooling load required in the fuel cell stack. This $Q_{\text{stacks}(\text{net})}$ will be used as the evaporator load in the thermal management systems worked upon in the upcoming section 3.3.

3.3. Thermal Management System

This section involves a comparison of different cooling methods used for thermal management of the LTPEMFC, considering the calculations for a basic vapor compression refrigeration system with maximum operating condition as the reference. The existing heat exchangers in all the cooling methods used for both phase change and single phase coolant circulation are ram air-cooled heat exchangers that will be situated in the aircraft nacelle.

The Master of Science Thesis from the Aerospace Department of TU Delft [79], as previously mentioned in 3.2 in [79], focused on 3 cooling methods: Vapor compression refrigeration cycle (VCRS), pumped multiphase cooling and single phase cooling, in which, for the first two methods, 3 different compressor outlet pressures (2.56, 3.54 and 4.8 bar) were used. Remaining available fuel cell power after considering effects of system weight, system power consumption, aircraft drag and available additional thrust due to ram effect, the results obtained from the previous thesis was that the pumped multiphase system led to 13% more available power, and 0.47% more weight. It was understood that even when a compressor is replaced by a pump, the main contributing component in the pumped multiphase system weight is the ram air-cooled heat exchanger which is 65% heavier due to its lower temperature difference with the ambient. The other disadvantage of using a pumped multiphase system compared to other cooling method is shown in the upcoming section 3.3.2, Table 3.8.

Along with the addition of the cryogenic H_2 fuel cooled heat exchanger (FCHX), the difference between the thermal management system components used in this work and the previously mentioned thesis is that, this thesis does not include a separate internal heat exchanger for condenser subcooling and compressor superheating, and allows the refrigerant to be superheated in the cooling channels of the fuel cell to +10K, eliminating the need of a separate pump and a phase separator. From a separate research on single phase serial cooling of fuel cell that divided the entire stack into smaller units with different operating temperatures and allowing a coolant temperature difference of ± 5 K across each unit, it was observed that the penalty on the efficiency of the fuel cell due to this ΔT is not significant [68].

Applying the cryogenic cold from the hydrogen supply will not only improve the thermal management system performance, but will also provide a heat source for the fuel cell anode reactant (H_2) to be supplied at the operating temperature. To get a starting value of condenser pressure for the basic VCRS system design, the higher value of 4.8 bar was selected as a reference and compared with other pressure values in the upcoming sub-section 3.3.1. The fuel cell operating pressure is kept constant as 1.5 bar throughout this thesis. Before the propulsion power generation begins, and right when the initial hydrogen supply is started, the fuel cell stack may not yet have generated sufficient heat to heat up the hydrogen to the fuel cell operating temperature. Therefore, an external on-ground heater must be connected to the hydrogen supply to raise its temperature to the fuel cell's operating range only for a short period before the thermal management system of the fuel cell is switched on. This heater will be used only for system startup and will be disconnected prior to flight, thus it is not included in the process flow diagrams. Drag effects and the additional thrust produced by the ram-air ducts at the maximum operating point, which is during the take-off are not included in this design.

3.3.1. Basic Vapor Compression Refrigeration system

This system incorporates components similar to those in a conventional vapor compression refrigeration system. The evaporator's function is managed by coolant channels between the bipolar plates of the LTPEMFC, and the condenser is ram air-cooled, which is located at both the sides of the aircraft nacelle. The coolant was chosen by providing conditions to CoolProp in Python environment, by first obtaining a list of refrigerants that had a saturation pressure between 1 and 3 bar at the saturation pressure of 343K (evaporator's phase changing temperature). The pressure was kept within this range to prevent a large pressure difference between the refrigerant in the bipolar plates of the fuel cell and the outside components, that could result in coolant leakage. After obtaining the list of compatible refrigerants, the one with the maximum latent heat of vaporization was chosen which was of methanol,

equal to 1085 (kJ/kg), making it a compatible refrigerant. Figure 3.6 shows the temperature-entropy diagram of a basic VCERS system.

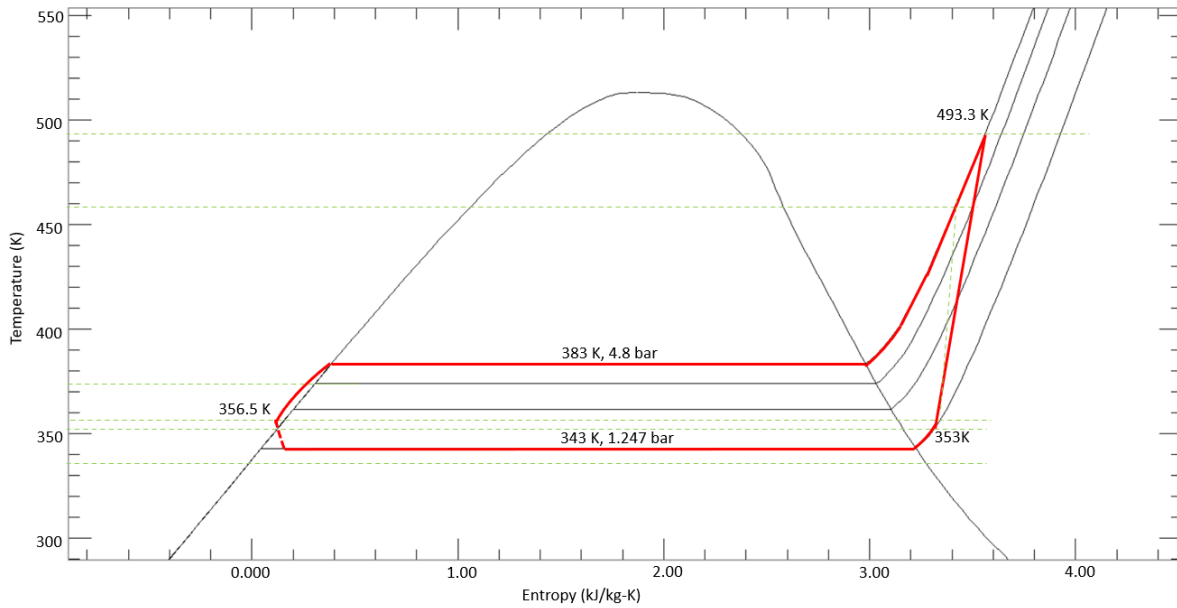


Figure 3.6: Temperature-entropy diagram of a basic methanol based vapor compression refrigeration system, with compressor efficiency 0.75 and pressure ratio of 3.85. The inlet vapor quality is 0.1.

The compressor pressure ratio used was set to 3.85 bar. The evaporator pressure is 1.247 bar, corresponding to the saturation pressure at the fuel cell’s operating temperature of 343 K. Based on these selections and assuming a compressor efficiency of 75%, the minimum allowable mass flow rate is calculated to be 1.3 kg/s, with a minimum compressor power (parasitic load) of 335.5 kW. In the condenser, as the refrigerant pressure is increased for a specific flowrate, the saturation temperature also rises, which helps maintain a high ΔT with the ambient. Additionally, the latent heat required for condensation is lower, allowing for a relatively small condenser size. The effect of increasing and reducing the condenser pressure is compared in the following Table 3.7.

Table 3.7: Effect of compressor pressure ratio on condenser size, considering ambient temperature as 328 K, evaporator pressure as 1.247 bar. It is observed that the required condenser area increases when the compressor pressure ratio is reduced, due to a smaller difference in condenser saturation temperature with ambient.

Compressor Pressure ratio	Condenser Heat rejection (kW)	Condenser Heat rejection (%)	Condenser $T_{Saturation}$ (K)	ΔT with ambient (K)	Resultant Condenser Heat transfer area (%)
3.85	1645.3	100	383	55	100
1.6	1417.6	86	355.96	27.96	164

The comparison of condenser size was made for 2 different compressor pressure ratios. The pressure ratio of 3.85 giving a condenser pressure of 4.8 bar was used as the reference. When the pressure ratio is reduced and the power consumption by the compressor is lower, the condenser heat rejection requirement reduces by 17.5%. As the condenser saturation temperature is 355.96 K at 2 bar (at pressure ratio of 1.6), the temperature difference between the condenser and the 328K ambient reduces by about 50%. For a fixed heat rejection load, the required condenser area to reject the same heat with a 50% drop in ambient ΔT would be twice. The resultant increase in the condenser heat transfer area would be by a factor of 1.64 due to drop in ΔT with ambient, and a drop in heat rejection load.

3.3.2. Pumped 2-phase cooling

Although the mass flow requirement is much less than single phase cooling and comparable to the vapor compression refrigeration cycle, installation of a pump in the liquid side of the circuit would mean that the flow direction in the T-S diagram will be clockwise (reverse of VCRS) as shown in the Figure 3.7. This would mean that the condenser pressure would be lower to that of the evaporator pressure. At the condenser pressure, the latent heat would be higher than the latent heat in the evaporator, meaning that the amount of heat needed to be rejected per kg of the refrigerant to get condensed would be higher. Also, since the saturation temperature at the condenser pressure is lower, it means that the ΔT with high ambient conditions would be lower, further increasing the condenser size. The pump accounts for compensating the allowable pressure drops in each component as well as hydraulic losses in the pipelines.

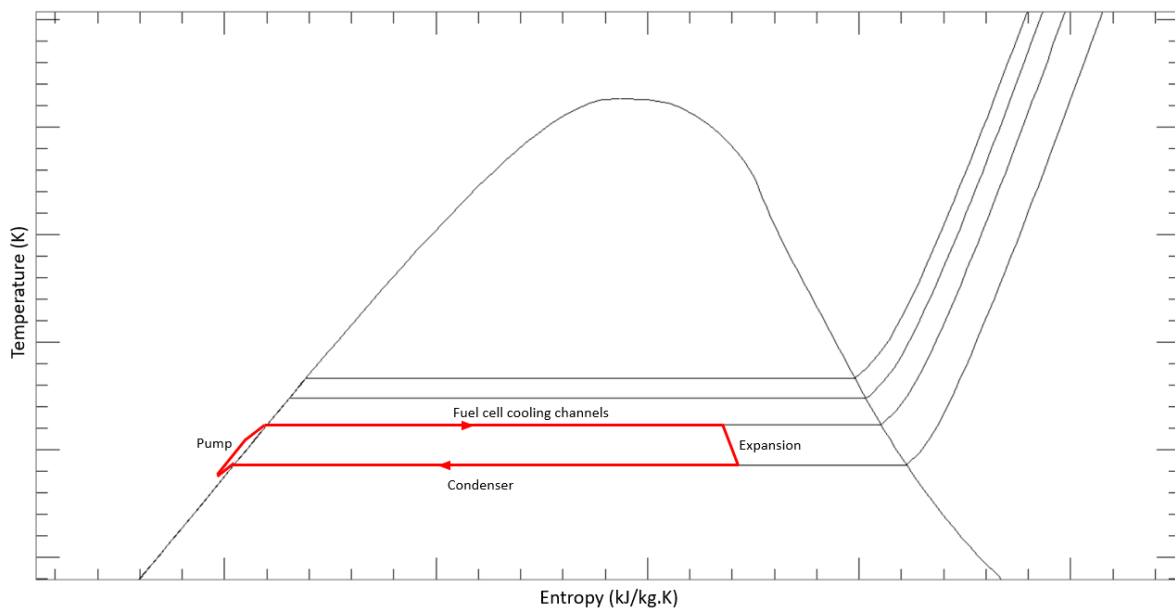


Figure 3.7: Temperature-entropy diagram of methanol based pumped 2 phase cooling system showing that the condenser operating temperature is below the evaporator operating temperature. This method can only be applied for HTPEMFCs with very high operating temperatures.

3.3.3. Single Phase cooling

The single phase cooling circuit involves a coolant pump and a heat exchanger. The coolant gains sensible heat from the fuel cell with a temperature gradient within the operating temperature range of the fuel cell, and the extracted heat is exchanged in a heat exchanger which is ram air-cooled in the nacelle of the aircraft. The coolant pump consumes much less power than a compressor since it is only the static pressure of the fluid that needs to be overcome, unlike in a compressor where both the compression work along with static pressure of the fluid is worked upon. This results in a negligible parasitic load on the aircraft when a pump is installed in the thermal management system.

When only using single phase cooling to cool the entire stack load, the calculated mass flow rate for cooling an LTPEMFC using a coolant with a high specific heat capacity (up to 3490 J/kg-K), such as with a 52% ethylene-glycol water solution, for an allowable $\Delta T = 10$ K is at least 37.5 kg/s. Given that the fuel cells in an aircraft are located in the wings, the traveling distance of the coolant to complete one circulation in the circuit would be considerable, depending on the circuit's positioning. This could increase the total coolant weight needed to deliver the required mass flow, thereby increasing the overall system weight.

The same problem arises with the sizing of the heat exchanger. As the ΔT between the exit flow temperature of the fuel cell and the ambient is low (worst case 35K), the heat transfer area requirement

for the single phase ram air-cooled heat exchanger would be larger than for the same heat exchanger used as a condenser in VCRS system. A basic comparison of each cooling method has been provided in the following Table 3.8:

Table 3.8: Comparison of different fuel cell liquid cooling methods, keeping ambient as 328 K. The heat exchanger size of pumped 2 phase system due to ambient $\Delta T(\%)$ is greater than of single phase cooling heat exchangers because there is a possibility of condenser saturation temperature to go below ambient, due to low operating temperature of LTPEMFCs causing system damage.

Parameter	Basic VCRS	Single Phase Cooling (Evaporator $\Delta T = 10K$)	Pumped 2 phase cooling
Coolant type	Methanol	30% Ethylene-Glycol Water	Methanol
Coolant mass flowrate (kg/s)	1.3	37.5	1.3
Parasitic load (kW)	335.5	0.923	0.142
HX load (kW)	1645.3	1310.7	1309.9
HX size due to load (%)	100	79.67	79.61
HX ΔT Ambient (K)	55	25	25
HX size due to ambient $\Delta T(\%)$	45.5	100	>100

It can be understood from Table 3.8 that although the increase in condenser size due to parasitic load for a VCRS is 26% higher, the condenser size drop due to the higher ΔT between the condenser temperature and the ambient is 54.5%. Although pumped 2 phase cooling requires a comparable coolant mass flowrate and with a negligible power consumption as to a VCRS system, based on a design point of view, when the system experiences the worst case scenario, on ground before take off; the maximum fuel cell power generation and high ambient would result in an increase in heat transfer area requirement for heat rejection. And if the pressure drop in the heat exchangers are significant, then the pressure in the ram-heat exchanger can go to sub-atmospheric conditions. Even though atmospheric temperatures drop down below 233K at cruise level, the fuel cell heat generation is also lower. Therefore design consideration at cruise level would not suffice to design these systems. For fuel cells with lower operating temperatures such as 333K, and with a significant pressure drop in the heat exchangers, the heat rejection temperature could also go below ambient causing reversed heat transfer. This cooling method can only be applied to HTPEMFCs, when the fuel cell operating temperature is high at around 473K and therefore allowing a relatively high condenser temperature with respect to ambient. Understanding all possibilities, the VCRS system has been worked upon in this thesis, with the objective towards reducing the parasitic load and integrating the reactant's cold energy for improving the COP and compactness of the thermal management system.

3.3.4. Serial cooling using single phase circuit

The serial cooling concept described in the paper by [68] involves fragmenting the total fuel cell into smaller units with serially increasing operating temperatures within the operable range. When applied to the current thermal management system, this approach solely (by eliminating the ram air-cooled VCRS) would still result in a comparatively high coolant mass flowrate of 9.38 kg/s, due to the high heat generation by the cell stack and low operating temperature range of LTPMEMFC (323-363 K). Therefore, one of the methods to integrate the cryogenic energy of the fuel is using a separate single phase cooling circuit operating simultaneously with the VCRS system by circulating a coolant with high specific heat capacity like 52% ethylene glycol solution with water. The allowable temperature change in the fuel cell by the sensible heat of the coolant is $\Delta T = \pm 5K$ of the fuel cell unit's operating temperature.

The German Aerospace Center worked on a Serial cooling concept of HTPMEMFC, by segregating the fuel stack of the same power output into smaller units with different operating temperatures [68]. Inspired by this serial cooling concept of HTPMEMFC that has a high operating temperature range than an LTPMEMFC, the possibility of involving the serial cooling concept for an LTPMEMFC is explored in this section and its impact in the parasitic load reduction and improvement in compactness of the thermal management system is explored further in the thesis.

The total available cryogenic cold for the entire propulsion unit is utilized for the single phase cooling circuit. The hydrogen supplied to the propulsion unit is to be divided into 4 equal streams, as illustrated later in Figure 5.3 of chapter 5, and directed to 4 small FCHXs to extract the cold from each. Each stack of 600 kW is divided into 2 Units, running at a different operating temperature with a difference of 10K. The units of the ram air-cooled stacks are illustrated in Figure 3.8. A coolant that has a high specific heat capacity (to extract greater amount of heat from the fuel cell before raising its own temperature), low freezing point far below the operating range (to prevent blockage in circulation), and a high density (for system compactness) is circulated through alternate the coolant channels present between the fuel cell bipolar plates. The other half of the cooling channels will have the existing methanol circulation for the VCRS.

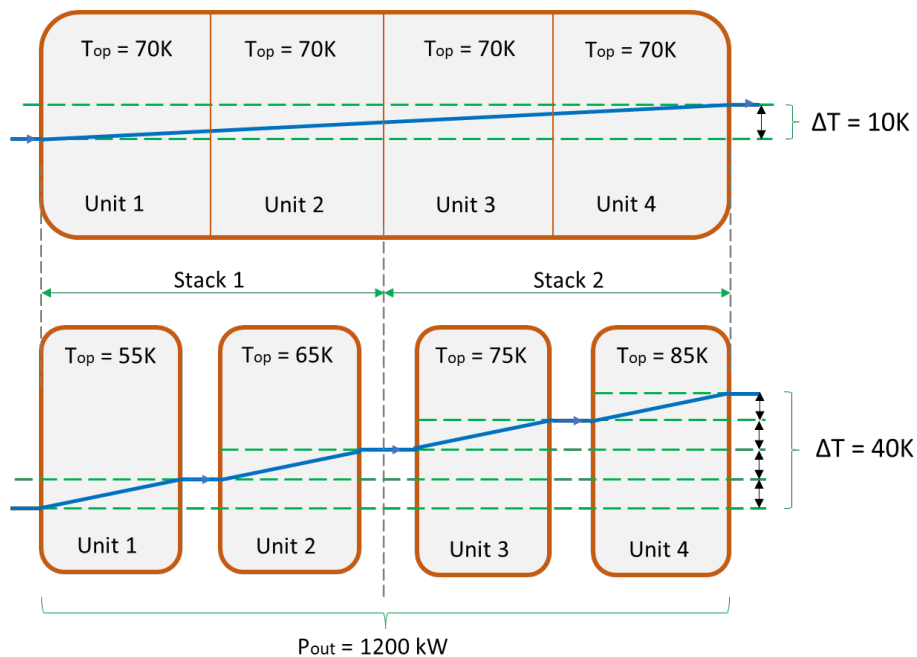


Figure 3.8: Serial cooling concept on LTPMEMFC showing a higher allowable coolant ΔT when each stack has a different operating temperature within the allowable range for the same total power output. The operating pressure is kept same as 1.5 bar. The top image shows the 2 ram air-cooled stacks before serial cooling is applied (giving a low $\Delta T = 10K$, the bottom image shows the stacks after serial cooling is applied with a high $\Delta T = 40K$.

As efficiency improves with temperature in the fuel cell for the same operating pressure, the first 2 of the units will be under-performing and the last 2 of the units will be over-performing. This can create a difference in the individual stack efficiency, but the discrepancy will average out to give a negligible effect in the overall efficiency [68].

3.4. Effect of Altitude Variations on Thermal Management system

A typical mission profile is plotted in the Figure 3.9, based on a typical short ranged flight journey showing the altitude variation with respect to the time of the journey as obtained from [83], and the normalized brake power variation with respect to altitude was obtained from the technical memorandums [84, 85], which was then added to the plot of mission profile. It was understood that the atmospheric pressure and the normalized brake power reduces with altitude.

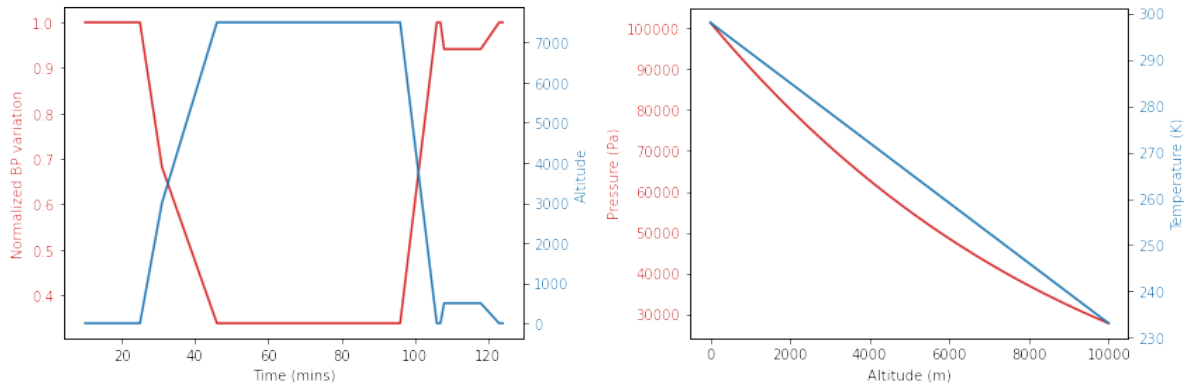


Figure 3.9: The atmospheric and normalized brake power variations with altitude. The left image shows a typical flight journey of a short ranged aircraft showing the altitude variation with respect to the time of the journey as obtained from [83], and the normalized brake power variation obtained from [85]. The right image shows the atmospheric pressure and temperature with flight altitude showing the drop in atmospheric temperature and pressure obtained from [86].

As the aircraft takes off, due to altitude variation, the ambient conditions change such as the atmospheric temperature, pressure, oxygen concentration, drag force. The drop in the ambient degrades the performance of the fuel cells. At high altitudes, during cruising speeds, the power generation requirements by the fuel cell is lower than while take off. This reduces the heat generation by the fuel cells and therefore the load in the thermal management system. For a fixed cooling channel design at low load conditions, the heat extracted by the refrigerant would reduce. After each cycle of the refrigerant and for a fixed compressor speed, there is a possibility for the cooling channels to eventually accumulate cold that can lead to drying up of the fuel cell and in worst case freeze. Therefore, to maintain the fuel cell temperature during variable load conditions, either the mass flowrate of the refrigerant can be reduced along with the compressor speed, or a false heat load can be provided to the cooling channel to compensate for the drop in heat load for a fixed compressor speed.

There are 2 ways of achieving this:

- by storing excess refrigerant in a liquid line receiver tank and reducing the compressor speed using a variable speed compressor.
- using a hot gas bypass from the compressor discharge line to the evaporator suction line with an equalizer line, when using a constant speed compressor.

The hot gas bypass valve is integrated into the system with its inlet connected via a tee to the discharge line, situated between the compressor outlet and the condenser inlet. The outlet of the bypass valve is connected to another tee located between the expansion valve and the before entry to the cooling channels of the fuel cell. To prevent liquid refrigerant from filling the line when the bypass is closed, and causing slugging upon bypass or compressor start-up, a check valve is installed in the hot gas bypass line before it enters the suction side of fuel cell cooling channels [87].

4

Design of Integrated System Components

This section involves the method in which the fuel tank and the cryogenic heat exchangers that are integrated into the system are designed. The fuel tank design involves its geometry, positioning, BOG integration and tank pressure balance and vaporizer mass balance. The heat exchanger design methodology is applicable for all single phase plate fin heat exchangers integrated into the thermal management system.

4.1. Fuel supply system

The components of the fuel supply system and the thermal management system are sized by considering maximum fuel cell operating condition.

4.1.1. Fuel Tank Configuration

The tank configuration which involves its shape, volume, valve setting and gravimetric index, depends on its location in the aircraft. Gravimetric index of the tank is the ratio of the mass of the fuel to the mass of the entire fuel system including the cryogenic tank [88]. Fuel, being one of the heaviest components of an aircraft is conventionally stored under the wings to accommodate a larger quantity of fuel for longer range flights. In the case of LH₂, for the same total volume of the fuel, if a single 5 m³ tank is split into two 2.5 m³ tanks and located at the wings, their surface area to volume ratio will increase by a factor of 1.26 for spherical tank, that will increase the amount of heat ingress into the cryogenic fuel and the gravimetric index of the storage system. Integrating the tank into the fuselage might need design modifications in the aircraft. Due to the low volumetric energy density of H₂, the overall tank volume would be larger than conventional kerosene-based Jet-A fuels for the same travelling range. The fuselage would need to be elongated to fit the same number of passengers, if the tank is located behind the passenger cabin, causing an increased overall take-off mass.

4.1.2. Tank pressure balance

To calculate the required mass flow input to the tank ullage adjusted by the vaporizer valve during the supply of LH₂, the thermodynamic processes in the tank can be segregated into 3 cases for a particular time step. Figure 4.1 shows the fuel tank with the transfer ports 'a' and 'b' for BOG and LH₂ respectively, and a receiving port 'c' for vaporized H₂ which are opened one at a time creating each case. For all the cases, the drop in LH₂ level due to the effect of boil-off rate is neglected.

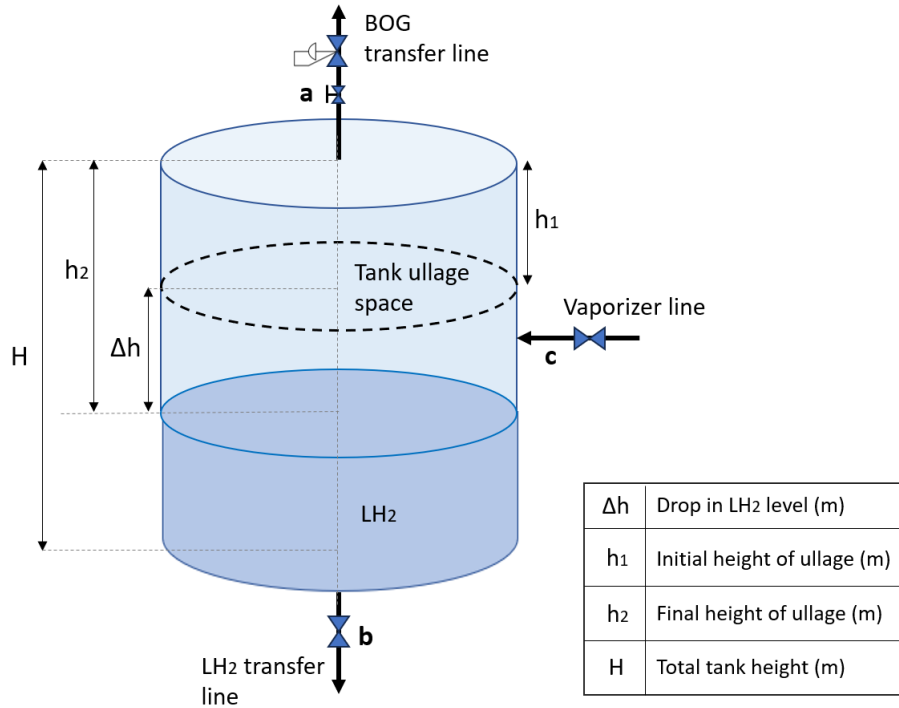


Figure 4.1: Tank vaporizer mass balance assuming a vertical cylindrical fuel tank shape. a = BOG pressure regulator, b = LH₂ transfer valve, c = vaporizer valve. (0 = closed, 1 = open).

Case 1: a=1, b=0, c=0; Case 2: a=0, b=1, c=0; Case 3: a=0, b=0, c=1.

Case 1: Initial tank condition right before LH₂ supply

In Figure 4.1, consider the isobaric case where 'a=1', 'b=0' and 'c=0'. By letting the BOG pass through the pressure regulator, the tank will maintain its pressure at $P_1 = 150000$ Pa. If the drop in liquid level due to the H₂ boil-off is neglected, the process can also be considered isochoric. For this constant ullage space at constant pressure and temperature, the mass of H₂ vapor in the ullage space (m_{v1}) is constant.

Case 2: Tank during supply

Now consider the case where 'a=0', 'b=1' and 'c=0'. When 'b' is open, the level of LH₂ drops from ' h_1 ' to ' h_2 ' by ' Δh ', isothermally. Considering liquid mass flowrate entering the ullage space due to boil-off to be negligible compared to the LH₂ supply mass flow rate \dot{m}_b in (kg/s):

$$\frac{\dot{m}_{\text{boil-off}}}{\dot{m}_b} \ll 1 \quad (4.1)$$

The calculations for mass and volume in the following are conducted with a time step of 1 second of flow. As the boil-off rate is neglected, the mass of vapor in the ullage space is constant even with the drop in liquid mass due to supply.

$$m_{v1} = m_{v2} = \frac{P_1 \cdot V_1}{R \cdot T_1} \quad (4.2)$$

$$R = \frac{\bar{R}}{M_{\text{H}_2}} = \frac{8.314}{0.002016} = 4124 \text{ J}/(\text{kg} \cdot \text{K}) \quad (4.3)$$

where m_{v1} and m_{v2} are the mass of vapor (kg) in the ullage space before and after supply per second, R is the specific gas constant. The following equations assuming ideal gas are considered for a vertical cylindrical ullage space.

$$V_1 = \pi \cdot r^2 \cdot h_1 \quad (4.4)$$

$$V_2 = \pi \cdot r^2 \cdot (h_1 + \Delta h) = \pi \cdot r^2 \cdot h_2 \quad (4.5)$$

where V_1 and V_2 are the initial and final tank ullage volume (m^3), r is the tank radius (m).

As the number of moles of H_2 vapor in the ullage space is constant, the ullage pressure drops due to ullage expansion caused by the drop in liquid level. Applying Boyle's Law, the relation of initial and final pressures with respect to their volumes were obtained.

$$P_1 \cdot V_1 = P_2 \cdot V_2 \quad (4.6)$$

Here P_2 is the pressure in (Pa) after expansion of the ullage space due to LH_2 supply. Substituting equation 4.4 and 4.5 into equation 4.6.

$$P_1 \cdot \pi \cdot r^2 \cdot h_1 = P_2 \cdot \pi \cdot r^2 \cdot (h_1 + \Delta h) \quad (4.7)$$

$$P_2 = \frac{P_1 \cdot h_1}{h_1 + \Delta h} \quad (4.8)$$

As $\Delta h > 0$, $P_2 < P_1$. The change in ullage pressure (bar), for the initial pressure of 1.5 bar is obtained as:

$$\Delta P = P_2 - P_1 = \frac{-1.5 \cdot \Delta h}{h_1 + \Delta h} \quad (4.9)$$

where the negative sign shows that there is a pressure drop. To bring the tank pressure back to normal, case 3 is considered below where the vaporizer valve 'c' brings the final tank pressure back to the initial tank supply pressure.

$$P_3 = P_1 \quad (4.10)$$

Case 3: During vaporizer supply

This is when 'a=0', 'b=0' and 'c=1'. The amount of H_2 fed through 'c' that is responsible in bringing the pressure of the tank back to P_1 , at the final ullage volume V_2 is denoted as ' $\Delta m_{v(c)}$ '. The following ideal gas relations are used considering an isochoric and isothermal case:

$$\frac{P_3}{m_{v3}} = \frac{P_2}{m_{v2}} \quad (4.11)$$

$$\Delta m_{v(c)} = m_{v3} - m_{v2} \quad (4.12)$$

where m_{v2} is the mass of hydrogen H_2 in ullage space before vaporizer feeds in, and m_{v3} is the final mass of H_2 vapor in ullage space after bring the pressure back to P_1 . Substituting equation 4.11 in equation 4.12, we get:

$$\Delta m_{v(c)} = \frac{P_3}{P_2} \cdot m_{v2} - m_{v2} = m_{v2} \left(\frac{P_3}{P_2} - 1 \right) \quad (4.13)$$

Substituting 4.10 and 4.8 in the above equation, the mass flow is obtained in terms of level of the liquid.

$$\Delta m_{v(c)} = m_{v2} \cdot \left(\frac{\Delta h}{h_1} \right) = m_{v1} \cdot \left(\frac{\Delta h}{h_1} \right) \quad (4.14)$$

The parameters in the equations above are converted to measurable quantities, as shown below:

$$\frac{m_b}{\rho_L} = \pi \cdot r^2 \cdot \Delta h \quad (4.15)$$

$$\Delta h = \frac{m_b}{\rho_L \cdot \pi \cdot r^2} \quad (4.16)$$

Substituting equation 4.2 and 4.16 into 4.14, the mass of hydrogen fed through the vaporizer valve 'c' per second to maintain the ullage pressure to P_1 can be obtained in terms of measurable quantities of the tank:

$$\Delta m_{v(c)} = \frac{P_1 \cdot V_1 \cdot m_b}{R \cdot T_1 \cdot h_1 \cdot \rho_L \cdot \pi \cdot r^2} \quad (4.17)$$

By conducting a mass balance in the vaporizer (10), whose function is explained in section 5.2.1, m_b is the sum of the hydrogen mass supply to the fuel cell (m_{H_2}) and the hydrogen supply back to the fuel tank through vaporizer valve (6).

$$m_b = m_{H_2} + \Delta m_{v(c)} \quad (4.18)$$

The equation 4.17 will then be expressed as:

$$\Delta m_{v(c)} = \frac{P_1 \cdot V_1 \cdot (m_{H_2} + \Delta m_{v(c)})}{R \cdot T_1 \cdot h_1 \cdot \rho_L \cdot \pi \cdot r^2} \quad (4.19)$$

In an example calculation, considering the initial fuel supply case from a 90% filled tank (4.5m^3) of radius $r = 1.03\text{m}$ and corresponding liquid level $h_1 = 1.35\text{m}$, having an amount of LH_2 transfer to the fuel cell during the first time step of 1 second as $m_{H_2} = 0.0538\text{ kg}$, the initial ullage pressure being $P_1 = 150000\text{ Pa}$, and ullage temperature $T_1 = 24\text{K}$, the amount of hydrogen supplied by the vaporizer valve would be:

$$\Delta m_{v(c)} = \frac{150000 \cdot 4.5 \cdot (0.0538 + \Delta m_{v(c)})}{4124 \cdot 24 \cdot 1.35 \cdot 70.85 \cdot \pi \cdot 1.03^2} \quad (4.20)$$

Rearranging and solving the equation 4.20 gives an amount of $\Delta m_{v(c)} = 0.001176\text{ kg}$ and $m_b = 0.05497\text{ kg}$ during that time step. This is equivalent to using up 2% of the amount of total LH_2 transfer in bringing back the tank ullage pressure. This is because, the same mass of LH_2 takes up more space when in gaseous state compared to liquid state.

4.2. Single phase heat exchanger design

In the design of heat exchangers, the two integration schemes (VCRS with intercooling and VCRS with separate single phase circuit) are considered separately. The design of the ram air-cooled condenser and the flow-boiling within the cooling channels of the fuel cell are not focused in this work. For detailed information on their respective designs, the MSc Thesis from the Aerospace Department of TU Delft, supervised by Prof. Dr. Ir. P. Colonna and Dr. Ir. C.M. de Servi, can be referred to [79].

Aluminium plate-fin heat exchangers (PFHE) are selected for aviation applications due to their efficiency of more than 90%, compactness shown by a high surface area density greater than $700\text{ m}^2/\text{m}^3$, capability to handle multiple gas streams and compatibility at cryogenic temperatures [89]. Plate-fin heat exchanger design calculations were carried out in Excel for three types of single-phase heat exchange applications: intercooling, de-superheating, and single phase cooling. The thermophysical and flow properties of hot and cold streams were obtained from REFPROP.

Following were assumed for the heat exchanger design:

- Negligible heat loss out of the heat exchanger system by proper insulation
- Steady state heat transfer
- Uniform heat flux throughout heat exchanger length
- Neglecting the possibility of fouling
- Refrigerant and air flow are one-dimensional homogeneous flows
- Heat conduction along axial direction and radiation heat transfer is negligible
- Thermophysical property variation of the fluids along heat exchanger length is neglected.
- No leakages between the fluid streams and both streams are unmixed
- No additional heat is generated or accumulated in the heat exchanger

Figure 4.2 shows nomenclature provided for the geometric parameters in the cross-section of a PFHE in a cross-flow configuration and Figure 4.3 shows the heat transfer surface areas involved in a single channel when fins are incorporated, that has been applied in the design.

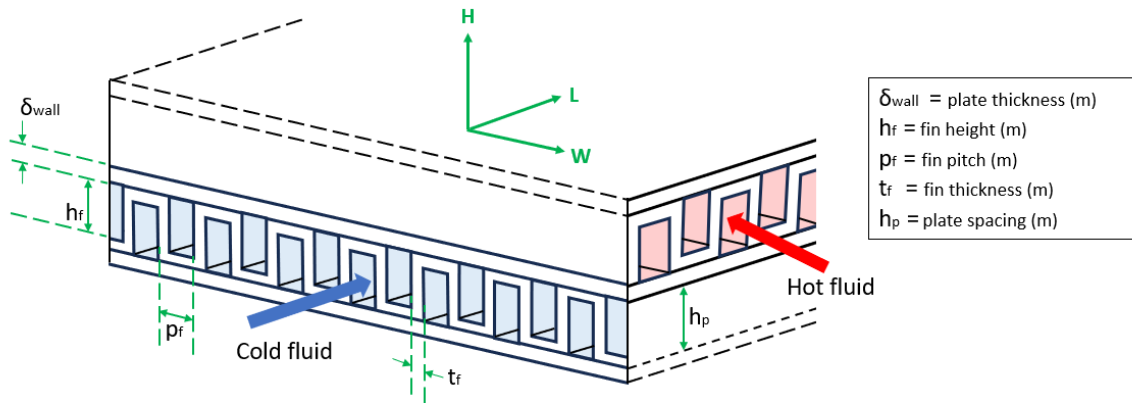


Figure 4.2: PFHE fin parameters shown for a cross-flow configuration, used in the intercooler and the de-superheater in the VCRS. For the case of counter-flow configuration used in the single phase circuit, the hot fluid entry is anti-parallel to the cold fluid entry (when the hot fluid side is rotated 90° anticlockwise).

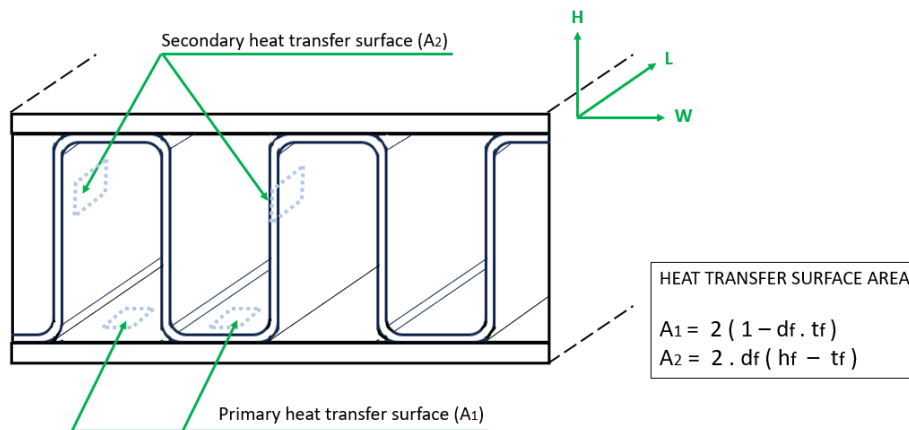


Figure 4.3: Primary (A_1) and Secondary (A_2) heat transfer area of PFHE at a single fluid passage. d_f = fin density (fins/m), t_f = fin thickness (m), h_f = fin height (m), Reference coordinates of heat exchanger W = width, L = length, H = height.

Not only heat exchangers, but any system component is preferred to be designed as per industrial standards, because customization would involve additional machinery and expenses. Therefore, to begin with the heat exchanger design, standard industrial plate fin configurations that are compatible for cryogenic fluids were selected. The core matrix material for the PFHEs selected is Aluminium alloy ASTM 3003/EN AW 3003, with lower temperature limit of 4K and a pressure limit up to 45 bars. The maximum temperature rating typically provided as 338 K, which allows manufacturers to use 5083K aluminium alloy piping, which is more economical. However, designs can accommodate temperatures up to 477K at low pressures, and design temperatures exceeding 338K are common [90, 91]. According to Towler [30], the maximum operable temperature for PFHE can be up to 423 K. Careful consideration is required, as methanol can aggressively corrode specific aluminium alloys [92]. Methanol being at the hot side has a possibility of corrosion with aluminium at higher temperature ranges. To minimise the effect of corrosion, the core material of the FCHX is expected to be chromium or titanium dioxide (TiO_2) coated. As the thickness of corrosion-resistant coatings is in the order of 10^{-6} m, the resultant effect of its lower thermal conductivity (94 W/(m.K) for Chromium and 8.4 W/(m.K) for Titanium dioxide) compared to aluminium fins and base plate (243 W/(m.K)) that is of thickness in the order of 10^{-3} m, is neglected.

Since the required temperatures, the cold load, mass flow rates and the thermophysical properties are the known parameters, Logarithmic Mean Temperature Difference method ($\Delta T_{LMTD(\text{counter})}$) is used to find the total heat transfer surface area.

$$Q_{PFHE} = U \cdot A \cdot \Delta T_{LMTD} \quad (4.21)$$

where Q_{PFHE} is the total heat transfer through the plate fin heat exchanger, U is the overall heat transfer coefficient ($W/(m^2K)$), A is the total heat transfer surface area. The logarithmic mean temperature difference of counter-flow configuration is obtained by first calculating the temperature differences at both the ends of the heat exchanger:

$$\theta_1 = T_{\text{ref}(\text{out})} - T_{\text{H}_2(\text{in})} \quad (4.22)$$

$$\theta_2 = T_{\text{ref}(\text{in})} - T_{\text{H}_2(\text{out})} \quad (4.23)$$

$$\Delta T_{LMTD(\text{counter})} = \frac{\theta_1 - \theta_2}{\ln\left(\frac{\theta_1}{\theta_2}\right)} \quad (4.24)$$

When the configuration selected is a cross-flow type PFHE, the LMTD of a cross-flow configuration ($\Delta T_{LMTD(\text{cross})}$) is by a factor (F) less than the counterflow LMTD, which can be obtained by substituting the fluid temperatures in the following equations:

$$P = \frac{T_{\text{H}_2(\text{out})} - T_{\text{H}_2(\text{in})}}{T_{\text{ref}(\text{in})} - T_{\text{ref}(\text{out})}} \quad (4.25)$$

$$R = \frac{T_{\text{ref}(\text{in})} - T_{\text{ref}(\text{out})}}{T_{\text{H}_2(\text{out})} - T_{\text{H}_2(\text{in})}} \quad (4.26)$$

The P and R constants were fit into the cross flow correction factor graphs available in [93] to obtain the LMTD correction factor (F) as provided in Figures A.2 and A.3. The corrected LMTD for cross-flow configuration is as follows:

$$\Delta T_{LMTD(\text{cross})} = F \cdot \Delta T_{LMTD(\text{counter})} \quad (4.27)$$

The standard fin geometric parameters are noted in the following table using by referring to existing industrial design parameters. The following geometric relations were applied from [94]:

$$p_f = \frac{1}{d_f} \quad (\text{m}) \quad (4.28)$$

where d_f is the fin density described by number of fins per unit width of the passage. The standard range of fin density is typically between 250 - 800 (fins/m) [95]. The cross-sectional area (m^2) of flow in a 1m of heat exchanger passage width is:

$$A_h = d_f \cdot (h_f - t_f) \cdot (p_f - t_f) \quad (4.29)$$

The corresponding perimeter of the flow passage per unit heat exchanger width (m) is:

$$P_f = d_f \cdot (2(h_f - t_f) + 2(p_f - t_f)) \quad (4.30)$$

The hydraulic diameter is obtained by:

$$d_{\text{hyd}} = 4 \cdot \frac{A_h}{P_f} \quad (4.31)$$

The sum of primary and secondary heat transfer surface area A_{sum} with units of (m^2/m) from Figure 4.3, of a unit heat exchanger passage width (m) is:

$$A_{\text{sum}} = P_f \cdot L = A_1 + A_2 \quad (4.32)$$

The overall heat transfer coefficient depends upon the thermophysical and flow properties of the fluid, the thermal properties of the core material of the heat exchanger and the fin efficiency. The thermophysical properties of the hot fluid and cold fluid were obtained from NIST database at their respective

mean temperatures. To keep the heat exchanger pressure drop within the allowable range, the mass flux (G) typically ranges within 10-300 kg/(m² · s) as mentioned in [93]. The average of this mass flux range was used as a starting point for the calculations and were adjusted to obtain a balance between the pressure drop and the total heat transfer surface area.

The Gnielinski correlation is a widely used empirical formula to determine the Nusselt number (Nu) for single-phase turbulent flow in circular tubes. It is extended to non-circular geometries, which in this case is the flow within rectangular channels in between 2 consecutive fins. The equations are modified based on the hydraulic diameter (d_{hyd}) of a rectangular channel, with the assumptions that the flow is fully developed and turbulent:

$$d_{hyd} = \frac{4 \cdot A_h}{P_{fin}} = \frac{4 \cdot (h_f - t_f) \cdot (p_f - t_f)}{2 \cdot (h_f - t_f) + 2 \cdot (p_f - t_f)} \quad (4.33)$$

The flow properties were obtained using dimensionless Reynolds number (Re), Prandtl number (Pr), friction factor (f).

$$Re = \frac{G \cdot d_{hyd}}{\mu} \quad (4.34)$$

$$Pr = \frac{C_p \cdot \mu}{k} \quad (4.35)$$

The minimum free flow area is obtained using:

$$A_o = \frac{\dot{m}}{G} \quad (4.36)$$

The performance of a duct of non-circular cross-section differs from a circular cross-section due to their geometrical dissimilarity. But for the case of turbulent flows, the friction factor f for non-circular cross sections can be evaluated by replacing the diameter by the hydraulic diameter d_{hyd} . The transition Reynolds number for rectangular channels is also approximately 2300, similar to circular ducts. The deviation in the f values is within about $\pm 8\%$ of the measured values according to [93]. Applying the Gnielinski correlation that is valid for $2300 < Re < 10^4$ and $0.5 < Pr < 2000$ obtained from [96–98]:

$$Nu = \frac{\left(\frac{f}{2}\right) \cdot (Re - 1000) \cdot Pr}{1 + 12.7 \cdot \left(\frac{f}{2}\right)^{\frac{1}{2}} \cdot (Pr^{\frac{2}{3}} - 1)} \cdot \left[1 + \left(\frac{D}{L}\right)^{\frac{2}{3}}\right] \quad (4.37)$$

where f is the Darcy friction factor, D is the channel diameter. For this case $D = d_{hyd}$ and L is the length of the channel.

$$f = \frac{1}{4} (1.82 \log Re - 1.64)^{-2} \quad (4.38)$$

The term $\left[1 + \left(\frac{D}{L}\right)^{\frac{2}{3}}\right]$ is the effect of the channel length on heat transfer. For PFHE, since it contains channel diameter in the order of 10^{-3} which is expected to be of a smaller order than the length of the PFHE (long channel), applying the assumption where $\frac{d_{hyd}}{L} \ll 1$ would make this term $\left[1 + \left(\frac{D}{L}\right)^{\frac{2}{3}}\right] \approx 1$. The Nu correlation would get simplified into the following:

$$Nu = \frac{\left(\frac{f}{2}\right) \cdot (Re - 1000) \cdot Pr}{1 + 12.7 \cdot \left(\frac{f}{2}\right)^{\frac{1}{2}} \cdot (Pr^{\frac{2}{3}} - 1)} \quad (4.39)$$

By substituting the Nu from equation 4.39 for the hot and cold side of the PFHE, the heat transfer coefficient for each side can be individually determined using:

$$h = \frac{Nu \cdot k}{d_{hyd}} \quad (4.40)$$

The purpose of the fins is to increase the heat transfer efficiency by increasing the available surface area density. The improvement in the overall heat transfer coefficient (U) is obtained by incorporating the fin efficiency.

$$\frac{1}{U \cdot A} = \frac{1}{h_{\text{cold}} \cdot A_{e(\text{cold})}} + \frac{\delta_{\text{wall}}}{k_{\text{wall}} \cdot A} + \frac{1}{h_{\text{hot}} \cdot A_{e(\text{hot})}} \quad (4.41)$$

where the individual effective contact areas are substituted by:

$$A_e = \eta_o \cdot A \quad (4.42)$$

The fin efficiency can be expressed as below:

$$\eta_f = \frac{\tanh M \cdot H'}{M \cdot H'} \quad (4.43)$$

where,

$$M = \sqrt{\frac{2 \cdot h_{\text{cold}}}{k_{\text{wall}} \cdot \delta_{\text{wall}}}}, \quad H' = \frac{h_f}{2} + \delta_{\text{wall}} \quad (4.44)$$

Once the fin efficiency (η_o) is achieved, the overall efficiency is obtained [99]:

$$\eta_o = \left[1 - (1 - \eta_f) \cdot \frac{A_2}{A_1 + A_2} \right] \quad (4.45)$$

Since the overall surface efficiency of hot and cold side takes into account the improvement in heat transfer surface area of hot and cold side respectively, the above equation can be converted into the following:

$$\frac{1}{U} = \frac{1}{\eta_{o(\text{cold})} \cdot h_{\text{cold}}} + \frac{\delta_{\text{wall}}}{k_{\text{wall}}} + \frac{1}{\eta_{o(\text{hot})} \cdot h_{\text{hot}}} \quad (4.46)$$

where h is the heat transfer coefficient, A is the heat transfer area the subscripts $_{\text{hot}}$ and $_{\text{cold}}$ are for the methanol and hydrogen side of the heat exchanger respectively. Once the U is obtained, the heat transfer surface area A can be calculated using equation 4.21.

The effect of fluid friction in a heat exchanger is important to determine pressure drop in hot and cold fluids. For thermal management systems, where single phase pumping of the liquid is carried out, the pumping power required to maintain the flow is determined by the pressure drop. For the VCRS system used here, the expansion valve pressure ratio is adjusted based on the sum of the pressure drops of all the heat exchangers. Apart from the major losses caused by fluid friction, minor losses are also present due to bends and fittings. These losses are based on the bend angle, sudden contraction or expansion, flow splitting and merging based on how the thermal management system has been designed. For the current case, only pressure drop due to the major losses is considered for single pass single phase flow. For rectangular channels of length L experiencing turbulent flow, the pressure drop per unit length ($\frac{\Delta p}{L}$) is calculated by:

$$\frac{\Delta p}{L} = 4 \cdot f \cdot \frac{1}{d_{\text{hyd}}} \cdot \frac{G^2}{2 \cdot \rho} \quad (4.47)$$

The value A involves the total heat transfer area involving both the fluid sides of the heat exchanger. Considering that the hot and cold fluids have been aligned alternatively in cross-flow and to obtain the heat transfer areas in contact with the individual fluid sides, the total heat transfer area A is divided into equal parts per fluid:

$$A_{\text{hot}} = A_{\text{cold}} = \frac{A}{2} \quad (4.48)$$

The heat transfer area A_{sum} in Table 5.5 is the amount of heat transfer surface area available in a single fluid passage per unit width, as illustrated in Figure 4.3, for $L = 1\text{m}$, $W = 1\text{m}$ and $H = (h_f + t_f + \delta_{\text{wall}})$.

Using this, the area density (β) with units (m^2/m^3) of hot and cold sides are individually obtained.

$$\beta_{\text{hot}} = \frac{A_{\text{sum}(\text{hot})}}{(h_{f(\text{hot})} + t_{f(\text{hot})} + \delta_{\text{wall}}) \cdot 1 \cdot 1} \quad (4.49)$$

$$\beta_{\text{cold}} = \frac{A_{\text{sum}(\text{cold})}}{(h_{f(\text{cold})} + t_{f(\text{cold})} + \delta_{\text{wall}}) \cdot 1 \cdot 1} \quad (4.50)$$

Using the area densities in equations 4.49 and 4.50, the total volume of the PFHE can be obtained:

$$V_{\text{PFHE}} = \frac{A_{\text{hot}}}{\beta_{\text{hot}}} + \frac{A_{\text{cold}}}{\beta_{\text{cold}}} \quad (4.51)$$

Based on the ALPEMA handbook on the standards of brazed plate-fin heat exchangers, the weight of the complete heat exchanger in practice varies between 650 - 1500 (kg/m^3), and a value in between of 1000 kg per unit core volume in (m^3) can be assumed [90].

5

Results

5.1. Reactant Supply and Fuel Cell Heat Release

Table 5.1 shows the mass flows through the fuel cell at its maximum operation point, and Table 5.2 shows the corresponding heat generation of the ram air-cooled fuel cell stack. It is observed that the heat generation of the stacks is greater than the power output of the stacks due to an efficiency lower than 50%, requiring a significant amount of cooling load. The cooling load of the 2 ram air-cooled stacks $Q_{\text{stacks(net)}}$ was used as the evaporator load in the thermal management systems.

Table 5.1: LTPEMFC mass flowrate calculations of reactant and products for a power generation of 2400000 W, assuming 21% O₂ concentration in air.

Parameter	Notation	Value
O ₂ Molecular weight (kg/mole)	$M_{r(O_2)}$	0.032
Air Molecular Weight (kg/mole)	$M_{r(\text{air})}$	0.02897
H ₂ Molecular Weight (kg/mole)	$M_{r(H_2)}$	0.00202
stoichiometric O ₂ mass flowrate (kg/s)	\dot{m}_{O_2}	0.284
stoichiometric air inlet mass flowrate (kg/s)	\dot{m}_{air}	1.225
Stoichiometric ratio of air	λ_{air}	2
non-stoichiometric air inlet mass flowrate (kg/s)	\dot{m}_{air}	2.43
unused air exit mass flowrate (kg/s)	$\dot{m}_{\text{air(used)}}$	2.166
stoichiometric H ₂ mass flowrate (kg/s)	\dot{m}_{H_2}	0.03588
Stoichiometric ratio of H ₂	λ_{H_2}	1.5
non-stoichiometric H ₂ inlet mass flowrate (kg/s)	\dot{m}_{H_2}	0.0538

Table 5.2: LTPEMFC mass flowrate calculations of reactant and products assuming 21% O₂ concentration in air. The values mean that the fuel cell is running at an efficiency of 47%.

Parameter	Notation	Value
Gross Power of ram air-cooled stacks (kW)	$P_{\text{stacks(2)}}$	1200
Total Heat released by the ram air-cooled stacks (kW)	$Q_{\text{stacks(2)}}$	1337.14
Cooling Load of the 2 ram-air-cooled stacks (kW)	$Q_{\text{stacks(net)}}$	1309.8

5.2. Integration of Intercooler and De-superheater

The cryogenic temperature range of the stored fuel during supply from the fuel tank, functioning as a heat sink, will not only regulate the heat generated by the fuel cell but also eliminate the need for an additional heating system for the hydrogen. This ensures that the hydrogen is supplied at the optimal operating temperature for the fuel cell. By utilizing the cryogenic properties of the fuel supply, the

thermal management system can improve its efficiency. Figure 5.1 involves the final integration of all the components of the H₂ supply system and the thermal management system of the LTPEMFC.

5.2.1. Hydrogen Supply Stream

The LH₂ fuel tank is a high energy density storage option for continuous Hydrogen supply to the fuel cell. It consists of a charging port, a pressure relief valve system for safety, a vaporizer line and 2 transfer lines: at the top of the tank for BOG integration and at the bottom of the tank for LH₂ transfer.

Initially on ground, the LH₂ is filled into the tank through the charging port. The BOG retrieval line (5) is open to retrieve the initial high boil-off due to the dynamic effects of the filling process. The vaporizer line (6), the manual valve (13) in BOG integration line and the LH₂ transfer line (8) is closed to prevent the excess initial high boil-off to be released into the aircraft fuel cell system while filling. The pressure regulator in line (5) is set to a pressure of 1.7 bar. The retrieved BOG can be directed back for re-liquefaction, or stored in a separate tank using a compressor to supply as a reactant to ground-based fuel cells to generate power for airport operations, thereby controlling boil-off during fuel charging.

After the filling process is complete, the charging port (2) and the BOG retrieval line (5) is manually closed and isolated from the external connections and the valve (13) is manually opened. The pressure regulator (4) is set to a pressure of 1.5 bar which is the required supply pressure of H₂ to the LTPEMFC. The adjustment of the pressure-regulator (4) is controlled by the vaporizer valve (6) that maintains the tank pressure, thereby allowing the BOG supply as per the optimum ullage pressure. The flowmeter (14) is used to measure the volumetric flowrate and using that, calculates the mass flowrate of the boiled-off hydrogen to the supply. It then signals the transfer line valve (8) and adjusts the LH₂ supply mass flowrate to fulfill the reactant requirement of the fuel cell. The LH₂ is then vaporized in (10) and supplied to the mixer (11), where the BOG is integrated to the vaporized LH₂. The superheat provided in the vaporizer is comparable to the BOG temperature so that the state of the two H₂ streams is thermodynamically same while mixing. The vaporizer uses either ambient heat or a separate negligible power consuming heat source to provide the latent heat to the LH₂. The vaporizer line (6) is to re-direct a part of the vaporized H₂ back to the tank to increase tank pressure to a level that will compensate the drop in tank pressure during LH₂ supply. The amount supplied back is nearly 2% of the LH₂ tapped from the transfer line (8), as explained in section 4.1.2. This will maintain the anode reactant supply pressure to the fuel cell, reduce additional boil-off that can happen due to pressure drop and eliminate the need of an external pump by generating a flow pressure to push the LH₂ to supply. A non-return valve (12) is placed in the BOG transfer line and vaporizer line to avoid back-flow of the hydrogen if there is a drop in the upstream pressure. The final H₂ stream is supplied to the FCHXs (intercooler (19) and de-superheater (16)), where it heats up to the LTPEMFC operating temperature of 343 K and provides its cold to reduce the load of the LTPEMFC thermal management system. A stream of H₂ (25) is re-circulated back as H₂ is supplied at a stoichiometry between 1.2 and 1.5 to the fuel cell. The pump (9) is kept as an optional component and will only be used if there is a variation in the supply pressure requirement or high pressure drops in the heat exchangers. All components that require frequent maintenance will require isolation valves on both sides to stop or re-direct the fluid flows while removing the component.

The pressure-relief valve (3) threshold depends upon the flight altitude, tank position and design pressure. It is provided as a safety measure to relieve a certain quantity of H₂ if the tank pressure rises due to sudden heat wave or excessive turbulence. For a set tank pressure, when fuel tanks are located under the wings and exposed to atmosphere, the drop in atmospheric pressure after take-off increases the pressure difference between tank and atmosphere. As the opening of the pressure-relief valve is triggered upon the pressure difference, the pressure-relief threshold needs to be higher than the difference between the maximum tank pressure and the minimum atmospheric pressure. For the case where the tank is located in a pressurized cabin of the aircraft fuselage, the pressure-relief threshold can be kept same as ground condition.

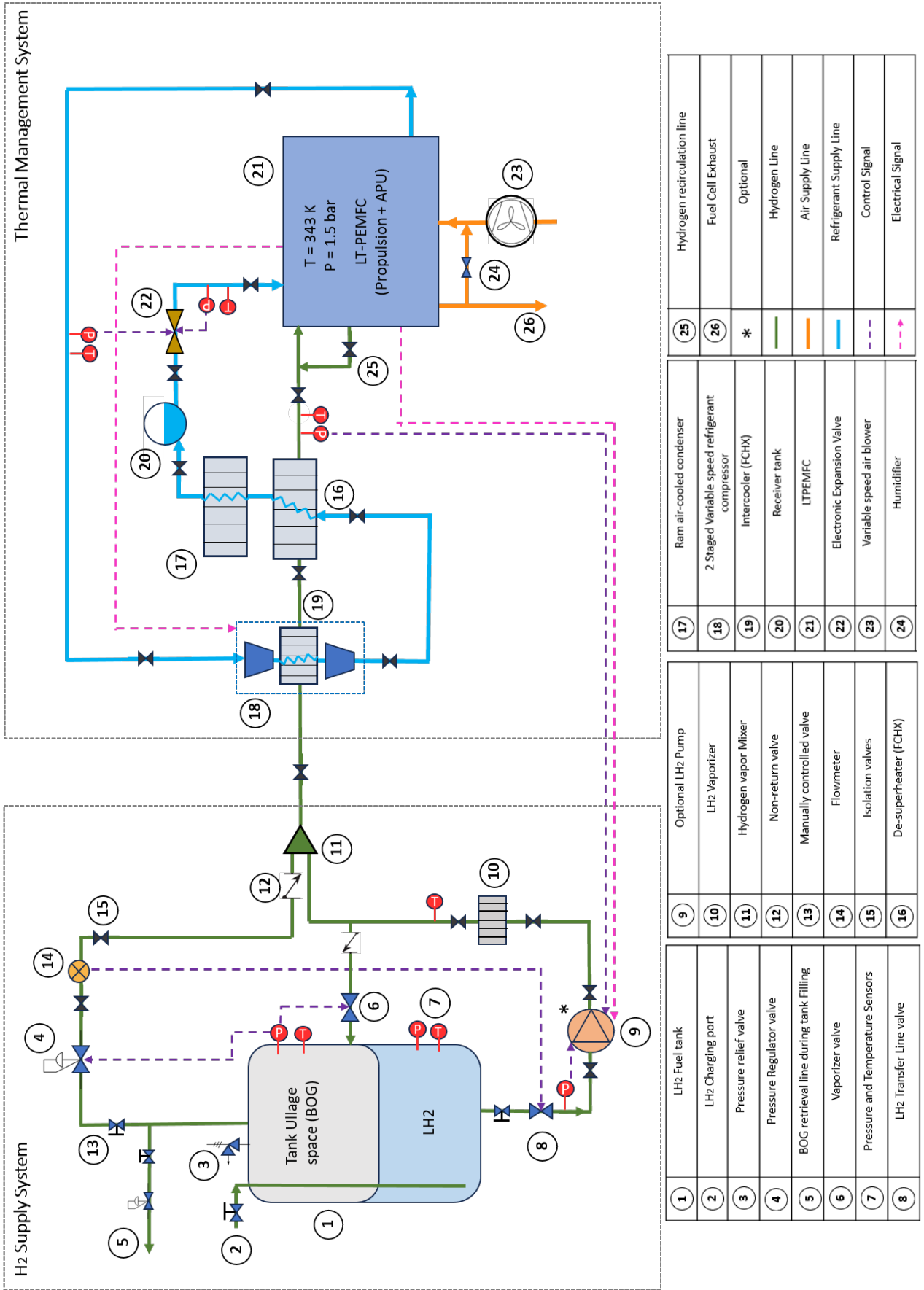


Figure 5.1: Complete Process Flow Diagram of Fuel Supply System and Thermal Management System with integrated cryogenic cold for intercooling and de-superheating in a VCERS. The box showing LTPEMFC involves 4 stacks generating power, but the ram air-cooled VCERS shown is only for cooling 2 of the stacks.

5.2.2. Thermal Management System

The heat rejection is segregated into 2 steps, where the ram air-cooled heat exchanger (17) is used as a condenser, the FCHX-(16) is used for de-superheating and the FCHX-(19) is used for intercooling, using the cryogenic cold from the H₂ supply. A receiver tank (20) stores the excess mass of the refrigerant during low load conditions. The electronic expansion valve inputs from the temperature and pressure sensors to adjust the orifice area to provide sufficient cooling at the evaporator inlet. The evaporator is replaced with cooling channels in between the bipolar plates in the fuel cell. A part of the fuel cell heat is removed by the unused air exhaust.

To reduce the parasitic load of the system and improve compressor efficiency, the single-staged compression is replaced with a 2-staged compression system with intercooling. As the calculations for the thermal management system design are based on the maximum operating point of the fuel cell, which occurs during the aircraft's takeoff phase, it represents the peak power demand, where the fuel cell operates at its highest power output. Figure 5.2 shows the corresponding temperature-entropy diagram of the integrated vapor compression refrigeration cycle with intercooled dual staged compression and de-superheater.

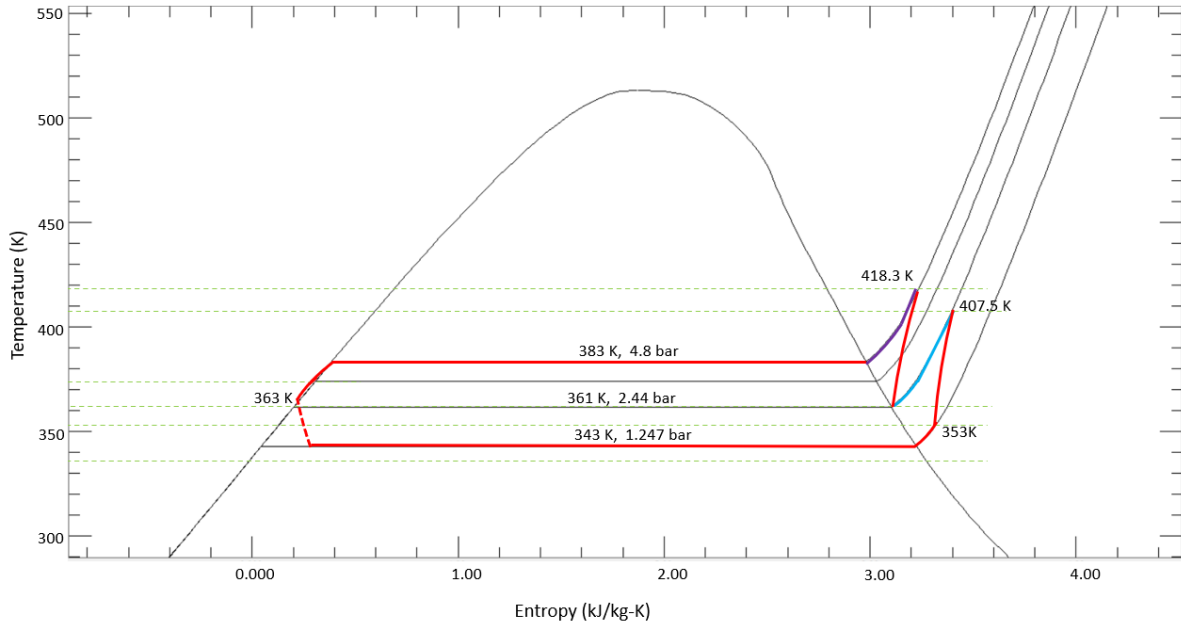


Figure 5.2: Temperature-entropy diagram methanol based 2-staged vapor compression refrigeration system with FCHX de-superheater (purple) and Intercooler (blue). Cooling channel inlet = 343 K 1.247 bar, cooling channel outlet = 353 K 1.247 bar, compressor stage 1 outlet and intercooler inlet = 407.5 K 2.44 bar, intercooler outlet and stage 2 inlet = 362 K 2.44 bar, stage 2 outlet and de-superheater inlet = 418.3 K 4.8 bar, condenser outlet and expansion valve inlet = 363 K 4.8 bar, (neglecting pressure drop in heat exchangers), evaporator superheating = 10K, condenser subcooling 20K.

The following equations were used for the calculations of each component.

Evaporator:

$$\dot{m}_{\text{ref}} \cdot (1 - x) \cdot H_{\text{vap, ev}} + \dot{m}_{\text{ref}} \cdot C_{p, \text{ev}} \cdot (T_{\text{superheat}} - T_{\text{op}}) = Q_{\text{stacks(net)}} \quad (5.1)$$

where \dot{m}_{ref} is the mass flow rate of the refrigerant, x is the evaporator inlet vapor quality of the refrigerant (fixed as $x = 0.1$ for all VCERS calculations), $H_{\text{vap, ev}}$ is the Latent heat of vaporization of refrigerant at fuel cell's operating temperature, T_{op} is the operating temperature of the fuel cell, $T_{\text{superheat}}$ is the degree of superheat in the evaporator (kept as 10K), $C_{p, \text{ev}}$ is the specific heat capacity of refrigerant for evaporator superheating and $Q_{\text{stacks(net)}}$ is the cooling load requirement of the fuel cell stacks.

Compressor stage 1:

Isentropic temperature rise of the refrigerant due to stage 1 compression can be obtained by the following equation:

$$T_{2s} = T_1 \cdot \left(\frac{P_2}{P_1} \right)^{\frac{\gamma-1}{\gamma}} \quad (5.2)$$

As compressors are not 100% efficient, the real temperature output from stage 1 compression is higher than in the isentropic case, which can be found out from the efficiency formula:

$$\eta_{c1} = \frac{W_{\text{isentropic}1}}{W_{\text{real}1}} = \frac{\dot{m}_{\text{ref}} \cdot C_{p_{c1}} \cdot (T_{2s} - T_1)}{\dot{m}_{\text{ref}} \cdot C_{p_{c1}} \cdot (T_2 - T_1)} = \frac{T_{2s} - T_1}{T_2 - T_1} \quad (5.3)$$

$$T_2 = \frac{(T_{2s} - T_1)}{\eta_{c1}} + T_1 \quad (5.4)$$

where η_{c1} is the stage 1 isentropic efficiency that typically ranges from 70%-90%, $W_{\text{isentropic}1}$ the compressor isentropic work, $W_{\text{real}1}$ the compressor real work, $C_{p_{c1}}$ mean specific heat of gas (assumed same for real work calculation), T_{2s} and T_2 are the isentropic and real temperature rise of refrigerant respectively.

Intercooler Hot side:

Intercooling is done by passing the refrigerant through a heat exchanger before entering the second stage of compression. The temperature of the refrigerant is brought down towards the saturation temperature at the intermediate (stage 1) pressure. The following equation will determine the cooling load required by the intercooler.

$$Q_{\text{intercooler}} = \dot{m}_{\text{ref}} \cdot C_{p_{\text{intH}}} \cdot (T_2 - T_{2'}) \quad (5.5)$$

where $C_{p_{\text{intH}}}$ is the specific heat capacity of hot side refrigerant in the intercooler, $T_{2'} = (T_{2(\text{sat})} + 1)$ denotes a 1 K superheat at the intermediate pressure. This is to practically prevent liquid traces from damaging the compressor during the 2nd compressor stage.

Compression stage 2:

The calculations are done in a similar way as Compression stage 1.

$$T_{3s} = T_{2'} \cdot \left(\frac{P_3}{P_2} \right)^{\frac{\gamma-1}{\gamma}} \quad (5.6)$$

$$\eta_{c2} = \frac{W_{\text{isentropic}2}}{W_{\text{real}2}} = \frac{\dot{m}_{\text{ref}} \cdot C_{p_{c2}} \cdot (T_{3s} - T_{2'})}{\dot{m}_{\text{ref}} \cdot C_{p_{c2}} \cdot (T_3 - T_{2'})} = \frac{T_{3s} - T_{2'}}{T_3 - T_{2'}} \quad (5.7)$$

$$T_3 = \frac{(T_{3s} - T_{2'})}{\eta_{c2}} + T_{2'} \quad (5.8)$$

Total Cryogenic cold:

The total amount of cryogenic cold from the H₂ supply stream which is meant to get completely utilized in the system is provided as follows:

$$Q_{\text{cold}} = Q_{\text{intercooler}} + Q_{\text{desuperheater}} \quad (5.9)$$

In equation 5.10 the cold load is segregated into two parts because the $C_{p_{\text{H}_2}}$ at mean temperature is different for each heat exchanger.

$$Q_{\text{cold}} = \dot{m}_{\text{H}_2} \cdot C_{p_{\text{H}_2}(\text{int})} \cdot (T_{\text{intercooler}(\text{out})} - T_{\text{BOG}}) + \dot{m}_{\text{H}_2} \cdot C_{p_{\text{H}_2}(\text{desup})} \cdot (T_{\text{OP}} - T_{\text{intercooler}(\text{out})}) \quad (5.10)$$

where \dot{m}_{H_2} is the mass flow rate of the H₂ supplied to the 4 fuel cell stacks, $C_{p_{\text{H}_2}}$ is the specific heat capacity of H₂ at its mean temperature in the component shown by the subscript, T_{OP} is the fuel cell

operating temperature which is equivalent to the outlet temperature of the H₂ from the de-superheater, $T_{\text{intercooler(out)}}$ is the intermediate H₂ temperature in between the Intercooler and the FCHX, T_{BOG} is the BOG temperature equivalent to the H₂ inlet temperature to the intercooler.

The integration of the de-superheater depends on the balance between the cold load provided by the H₂ supply and the cold energy requirement of the intercooler. Calculations show that the cold load of the H₂ supply stream (249.7 kW) exceeds the heat load of the intercooler (128.4 kW). This imbalance suggests that using a single heat exchanger solely for intercooling would result in a waste of the remaining 121.3 kW of cooling potential. To maximize efficiency, the cold energy is used first for intercooling and the remaining for condenser de-superheating in the FCHX. This ensures that the available cooling capacity of the H₂ supply is fully utilized and that the H₂ can then be provided within the fuel cell operating temperature range.

De-superheater Hot side:

The de-superheater cools the methanol from the compressed superheated state to the saturation temperature at the 2nd stage outlet pressure. The remaining cryogenic cold available in the de-superheater is:

$$Q_{\text{desuperheater}} = Q_{\text{cold}} - Q_{\text{intercooler}} \quad (5.11)$$

The de-superheating requirement by the condenser is as follows:

$$Q_{\text{CSH}} = \dot{m}_{\text{ref}} \cdot C_{p(\text{CSH})} \cdot (T_3 - T_{3(\text{sat})}) \quad (5.12)$$

where $C_{p(\text{CSH})}$ is the specific heat capacity in superheated state before entering condenser. If the available cryogenic cold in the de-superheater is more than the requirement for complete de-superheating, then a certain amount of methanol condensation is evident. The cold available for the condensation in the de-superheater is ($Q_{\text{cond-desup}}$) is:

$$Q_{\text{cond-desup}} = Q_{\text{desuperheater}} - Q_{\text{CSH}} \quad (5.13)$$

The percentage of the methanol mass flowrate that would be condensed in the FCHX is:

$$\dot{m}_{\text{cond-desup}} = \frac{Q_{\text{condensation(FCHX)}}}{\Delta H_{\text{vap}(c)}} \quad (5.14)$$

Based on calculations, it was observed that ($Q_{\text{cond-desup}} = 3.36\text{kW}$) of latent heat was provided by the de-superheater before entering the condenser, giving a 0.26% condensation in the de-superheater. This means that the methanol is now at a saturated state.

Condenser:

The condenser load is the sum of the heat removed by the evaporator from the fuel cells and the total compressor work input minus the total heat removed by the cryogenic cold.

$$Q_{\text{condenser}} = Q_{\text{stacks(net)}} + W_{\text{comp}} - Q_{\text{cold}} \quad (5.15)$$

$$W_{\text{comp}} = W_{\text{real}_1} + W_{\text{real}_2} \quad (5.16)$$

where $Q_{\text{condenser}}$ is the heat needed to be rejected by the condenser, W_{comp} is the sum of real staged compression works. The condenser heat rejection can be further segregated into 3 regions: condenser super heat rejection (Q_{CSH}), latent heat rejection (Q_{CLH}) and subcooled heat rejection (Q_{CSB}). Since the de-superheating is completely taken care of by the cryogenic cold, the resulting condenser load consists of:

$$Q_{\text{condenser}} = Q_{\text{CLH}} + Q_{\text{CSB}} \quad (5.17)$$

The 0.26% of condensation in the de-superheater is neglected and the entire latent heat for condensation is considered in the ram air-cooled condenser.

$$Q_{\text{CLH}} = \dot{m}_{\text{ref}} \cdot \Delta H_{\text{vap}_c} \quad (5.18)$$

$$Q_{\text{CSB}} = \dot{m}_{\text{ref}} \cdot C_{p(\text{CSB})} \cdot (T_{3(\text{sat})} - T_{\text{CSB}}) \quad (5.19)$$

where $T_{3(\text{sat})}$ is the saturation temperature at condenser pressure, ΔH_{vap_c} latent heat of vaporization at condenser pressure, $C_{p(\text{CSB})}$ is the specific heat capacity at subcooled region, T_{CSB} is the subcooled outlet temperature from the condenser. Since the vapor compression system operates in a closed cycle, the enthalpy before entering the expansion valve must be the same as before entering the evaporator, due to the isenthalpic nature of the expansion process. The degree of subcooling in the condenser is obtained in equation 5.20, which is then re-arranged to obtain the inlet temperature of the expansion valve.

$$\Delta T_{\text{CSB}} = \frac{Q_{\text{CSB}}}{\dot{m}_{\text{ref}} \cdot C_{p(\text{CSB})}} \quad (5.20)$$

5.3. Integration of Serial cooling circuits

The integrated thermal management system is shown in the process flow diagram in Figure 5.3. The different operating temperatures of the units will have a different saturation pressure for phase change cooling to take place in the VCRS part of the system.

5.3.1. Single phase cooling circuit

The coolant 52% ethylene glycol is chosen because it has a high specific heat capacity of 3.49 kJ/(kg.K), a low operable temperature limit of 233 K, and a high density of 1045 kg/m³ (for system compactness) obtained from [100]. Alternative fluids with high specific heat suitable for cryogenic heat exchange were looked upon such as helium, that has a higher specific heat capacity in the range of 5 kJ/(kg.K). However, having a liquefaction point of 4K, helium exists as a gas at the operating temperature range of this circuit, which would require additional helium compressors to circulate the coolant. Helium compressors are an expensive and power consuming equipment. Also gaseous helium, having a density of nearly 0.2kg/m³, would take up a significant amount of piping size at a certain mass flowrate.

The hydrogen is split into 4 streams with equal mass flowrates as each unit is assumed to be delivering equal amounts of power. Energy balances are conducted in each of the 4 FCHXs:

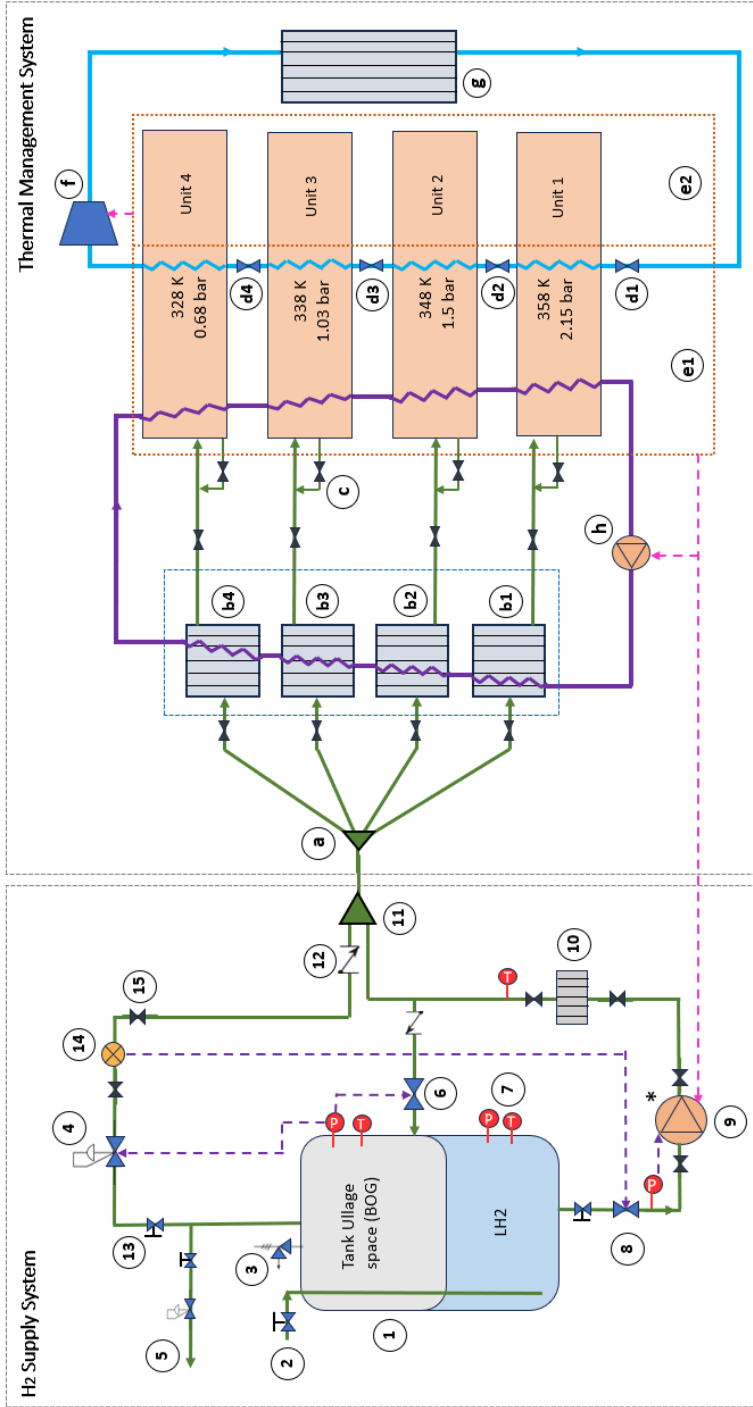
$$Q_{\text{FCHXs}} = \sum_{i=1}^n \left[\frac{\dot{m}_{\text{H}_2}}{n} \cdot C_{p_{\text{H}_2(i)}} \cdot (T_{\text{OP}(\text{unit}(i))} - T_{\text{BOG}}) \right] \quad (5.21)$$

where i is the counter, $T_{\text{OP}(\text{unit}(i))}$ is the mean operating temperature of the i^{th} unit, $C_{p_{\text{H}_2(i)}}$ is the specific heat at mean temperature of the hydrogen in i^{th} FCHX (obtained from REFPROP) and n is the total number of fuel cell units, which in this case is 4.

The total cold load Q_{FCHX} provided by the FCHX is equal to the total heat extracted by the coolant from the four units. Considering a $\Delta T = 10\text{K}$ temperature change is allowed in each of the units, the mass flowrate of the ethylene glycol can be obtained from:

$$\dot{m}_{\text{glycol}} = \frac{Q_{\text{FCHXs}}}{C_{p_{\text{glycol}}} \cdot n \cdot 10} \quad (5.22)$$

Even at high mass flowrates, there could be a tendency of frost formation if there are locations where fluid particles momentarily stop such as in stagnation zones within the heat exchanger channels of the hot fluid, due to high localized heat transfer. In practical cases, local thermophysical and material properties such as the local thermal conductivity of the plates separating the fluid can also vary along length and cause heat flux variations. This can be checked by conducting tests on the performance and compatibility of the FCHX for different flight durations. To avoid situations like blockages due to frost formation, deriming and de-frosting of the heat exchangers are needed at regular intervals, such as after every short-ranged flight journeys. If additional weight of around 1 kg is allowed in the aircraft, an extra single FCHX can be placed in tandem with one of the four FCHXs as shown in Appendix A.4, to bypass each of the hydrogen sub-streams one at a time, while defrosting. The next part involves the calculations for the VCRS part of the thermal management system.



a	Hydrogen stream Splitter
b (1, 2, 3, 4)	Fuel cooled heat exchangers (FCHX) 1,2,3,4
c	Hydrogen recirculation line
d (1, 2, 3, 4)	Isenthalpic Expansion Stages 1, 2, 3, 4
e1	ram air-cooled stacks divided into 2 Units per stack
e2	Other stacks of propulsion engine divided into 2 units per stack
f	Refrigerant compressor
g	Ram air cooled condenser
h	Coolant Pump
—	Single phase Coolant line
⋯	Line separating ram air-cooled stacks with other stacks of propulsion engine

Figure 5.3: Complete process flow diagram of fuel supply system connecting with the thermal management system, where the cryogenic cold is integrated in an additional single phase cooling circuit to reduce the evaporator load on the existing ram air-cooled VCRRS. The left box shows the boil-off integrated fuel supply system and the right box shows the thermal management system. This system differs from the intercooler and de-superheater configuration by involving 4 smaller FCHXs ('b1', 'b2', 'b3', 'b4') in a separate circuit, and serially varying fuel cell operating temperatures.

5.3.2. Vapor Compression Refrigeration System

As each of the 4 units work at a different operating temperature, the saturation pressure of methanol and the latent heat of methanol vaporization in each will also vary to extract fuel cell heat by vaporization. To bring it down to the saturation pressure from the condenser pressure, a stage-wise expansion is provided. A staged expansion is shown in the temperature-entropy plot in Figure 5.4 to bring down the pressure to the saturation pressure at the corresponding unit. Table 5.3 shows the operating temperature of each unit and its corresponding saturation pressure obtained from REFPROP.

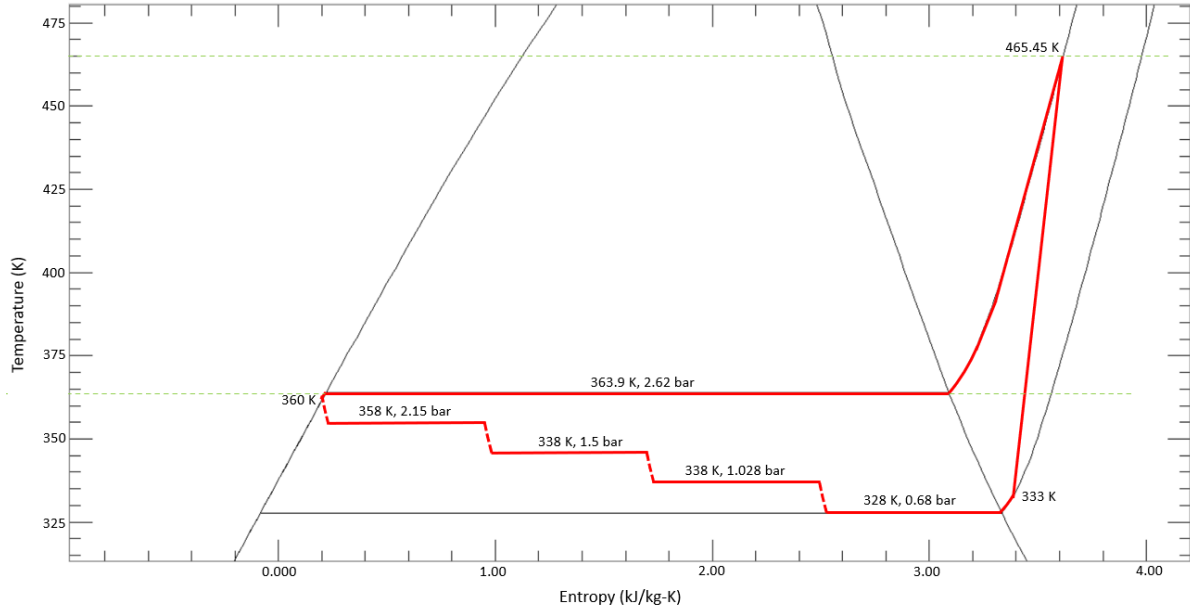


Figure 5.4: Temperature-Entropy diagram methanol based VCERS with stage-wise expansion. Pressure ratio of compressor kept same as the other system. Condenser subcooling is at 3K.

Table 5.3: Varying saturation pressures for the stage-wise expansion process at different fuel cell unit operating temperature ranges. It is observed that the higher the operating temperature, the lower is the latent heat of vaporization in the evaporator and higher is the saturation pressure in the evaporator.

Unit (i)	Operating temperature range (K)	Saturation pressure at mean (bar)	$\Delta H_{vap_{ev}}$ at mean (kJ/kg)
1	353 - 363	2.15	1058.4
2	343 - 353	1.5	1080.2
3	333 - 343	1.028	1100.4
4	323 - 333	0.68	1119.2

The inlet vapor quality in Unit 1 is kept as $x = 0.1$, and the overall compressor pressure ratio is same for all VCERS systems used in this thesis. It is also assumed that equal quantities of refrigerant is vaporized in each unit, and the average of all the $\Delta H_{vap_{ev}}$ at mean temperatures is considered for the energy balance in the entire **(e1)** shown in Figure 5.3. Also superheat provided before entry to compressor is 5K. Using the following equation 5.23, the mass flowrate of methanol can be obtained.

$$\dot{m}_{ref} \cdot (1 - x) \cdot \left(\frac{\sum_{i=1}^n \Delta H_{vap_{ev(i)}}}{n} \right) + \dot{m}_{ref} \cdot C_{p_{ev}} \cdot 5 = Q_{stacks(net)} - Q_{FCHXs} \quad (5.23)$$

After obtaining the mass flowrate, the compressor real outlet temperature (T_2) and real work done (W_{comp}) can be obtained using equations 5.2, 5.3 and 5.4, and a compressor efficiency of 0.75. The condenser load $Q_{condenser}$ can be obtained.

$$Q_{condenser} = Q_{stacks(net)} - Q_{FCHXs} + W_{comp} \quad (5.24)$$

The subcooling provided in the ram air-condenser is then obtained by subtracting the amount of condenser superheat and latent heat. The temperature before the entry of expansion valve (d1) is found by rearranging equation 5.20.

5.4. Results of component sizing

5.4.1. De-superheater

The de-superheater brings the superheated compressed methanol into its saturated state. The information regarding the heat exchanging fluids are shown in the Table 5.4 as follows:

Table 5.4: De-superheater heat exchange conditions for energy balance. The thermophysical properties like specific heat capacity obtained at mean temperatures

Parameter	Hot Side	Cold Side
Fluid	Methanol	H ₂ BOG
\dot{m}_{ref} (kg/s)	1.3	0.0538
Pressure (bar)	4.8	1.5
Inlet Temperature (K)	418.3	192.8
Outlet Temperature (K)	383	343
C_p (kJ/kg.K)	2.57	15

Due to the high difference between the hot stream temperatures and the cold stream temperatures at inlet and exit, there is no pinch point in any of the flow configurations of the de-superheater as shown in Figure 5.6. Therefore any of the three configurations: parallel, counter and cross-flow configurations are possible. The cross-flow configuration is chosen as it is more efficient than parallel flows and design-wise flexible compared to counter-flow, for instance if multi-pass configurations are considered.

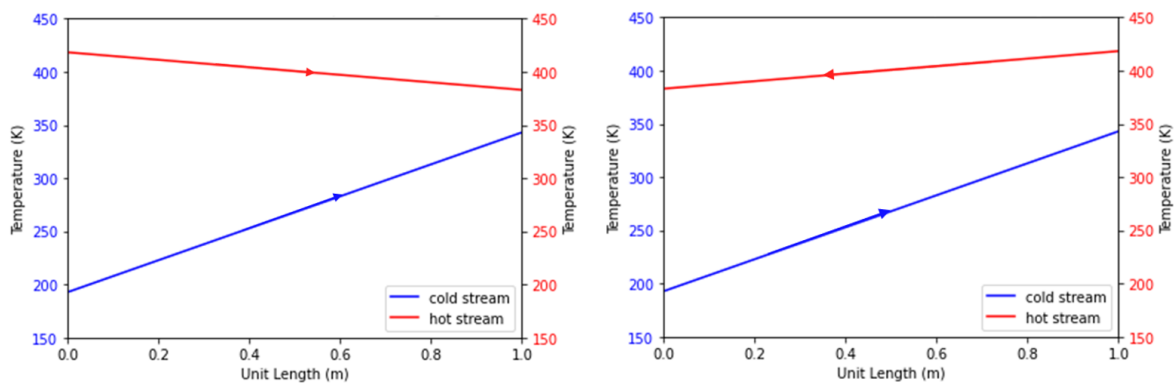


Figure 5.5: De-superheater flow configuration with left image showing parallel-flow configuration and right image showing counter-flow configuration. The temperature variation lines are straight due to the assumption of a uniform and constant C_p for all temperature difference per unit length of the heat exchanger. The high ΔT in the hydrogen stream is due to the greater difference between the hydrogen supply temperature to fuel cell and the low hydrogen outlet temperature from the intercooler.

The calculations were performed and noted in the Table 5.5 for FCHX using standard ranges used in industry, which is obtained from the paper by Jing-hua and Chen [94, 101].

Table 5.5: Standardized Fin parameters of hot and cold side of de-superheater.

Fin Parameter	Notation	Hot Side	Cold Side
Fin Thickness (m)	t_f	0.00025	0.00022
Fin Height (m)	h_f	0.01	0.003
Fin Density (fins/m)	d_f	600	600
Fin pitch (m/fin)	p_f	0.00167	0.00167
Cross sectional area per passage (m ²)	A_h	0.0082875	0.00241304
Fin perimeter (m)	P_f	13.04	5.072
Hydraulic diameter (m)	d_{hyd}	0.002474	0.0019
Primary heat transfer area (m ²)	A_1	1.7	1.736
Secondary heat transfer area (m ²)	A_2	11.7	3.336
Ratio secondary to total heat transfer	$\frac{A_2}{(A_1+A_2)}$	0.8731	0.6577
Heat transfer area per m ² single passage plate (m ²)	A_{sum}	13.4	5.072
Plate spacing (m)	h_p	0.01075	0.00372
Area Density (m ² /m ³)	β	1246.51	1363.44

In Table 5.6, the design results obtained by substituting the thermophysical and flow properties of the fluid and the materials in contact for heat exchange are provided for the de-superheater at the maximum operating point of the fuel cell. Table 5.7 shows the results for the overall surface efficiency due to fins for and ultimately the pressure drop in each side of the fluid for the de-superheater at its maximum operating point. Table 5.8 shows the final design calculation results of the de-superheater.

Table 5.6: Thermophysical and flow properties of hot and cold fluid in de-superheater based on maximum operating point of fuel cell stacks [94, 101].

Property	Notation	Hot Side	Cold Side
Mean Temperature (K)	T_{mean}	400.65	267.9
Dynamic viscosity (Pa.s)	μ	0.000012745	0.0000082874
Specific heat capacity (J/kg.K)	C_p	2564.4	15116
Thermal conductivity (W/m.K)	k	0.029068	0.18061
Density (kg/m ³)	ρ	4.9671	0.13563
mass flow (kg/s)	\dot{m}	1.3	0.0538
mass flux (kg/m ² s)	G	150	10
Minimum Free flow area (m ²)	A_o	0.00867	0.00538
Reynolds number	Re	29116	2296
Prandtl number	Pr	1.124	0.6936

Table 5.7: Heat Transfer and pressure drop per unit length results of de-superheater based on maximum operating point of fuel cell stacks [94, 101].

Parameter	Notation	Hot Side	Cold Side
Darcy Friction factor	f	0.02378	0.04989
Nusselt Number	Nu	88.963	7.1616
Heat transfer coefficient (W/m ² .K)	h	1045.3	679.68
Fin efficiency	η_f	0.8563	0.9853
Overall surface efficiency	η_o	0.8746	0.9904
Fluid unit Pressure Drop (Pa/m)	$\frac{\Delta p}{L}$	87086.1	38658.2

Table 5.8: Heat Transfer inputs de-superheater based on maximum operating point of fuel cell stacks [94, 101].

Parameter	Notation	Value
Plate thickness	δ_{wall}	0.0005
Plate conductivity (W/m.K)	k_{wall}	243
Overall heat transfer coefficient (W/m ² .K)	U	387.37
LMTD correction factor	F	0.9592
Corrected LMTD (K)	$\Delta T_{LMTD(\text{cross})}$	118.94
Heat Transfer surface area (m ²)	A	2.632
De-superheater volume (m ³)	$V_{(\text{PFHE})}$	0.00202
Unit weight (kg/m ³)	$\rho_{(\text{PFHE})}$	1000
De-superheater weight (kg)	$m_{(\text{PFHE})}$	2.02

5.4.2. Intercooler

This sub-section involves the intercooler, designed the same way as the de-superheater. The flow configuration chosen for the Intercooler is also a cross-flow type configuration. Table 5.9 shows the fluid conditions on hot and cold side of the Intercooler, after an energy balance in the heat exchanger was conducted as done in equation 5.5. For the illustration of the cross-flow configuration of the Intercooler Figure 4.2 can be referred.

Table 5.9: Intercooler heat exchange conditions for energy balance. In the energy balance, the C_p of hydrogen and outlet temperature of hydrogen was unknown. As the C_p of gaseous hydrogen changes with mean temperature it was obtained by iterating 8 times the energy balance using a starting $C_{p\text{H}_2} = 16.3$, until error was 0.14%.

Parameter	Hot Side	Cold Side
Fluid	Methanol	H ₂ BOG
\dot{m}_{ref} (kg/s)	1.3	0.0538
Pressure (bar)	2.44	1.5
Inlet Temperature (K)	407.5	24
Outlet Temperature (K)	362	192.8
C_p (kJ/kg.K)	2.17	14.13

Due to the high difference between the hot stream temperatures and the cold stream temperatures, there is no pinch point in any of the flow configurations of the Intercooler either as shown in Figure 5.6. Therefore any of the three configurations: parallel, counter and cross-flow configurations are possible. The cross-flow configuration is chosen as it is more efficient than parallel flows and design-wise flexible compared to counter-flow, for instance if multi-pass configurations are considered.

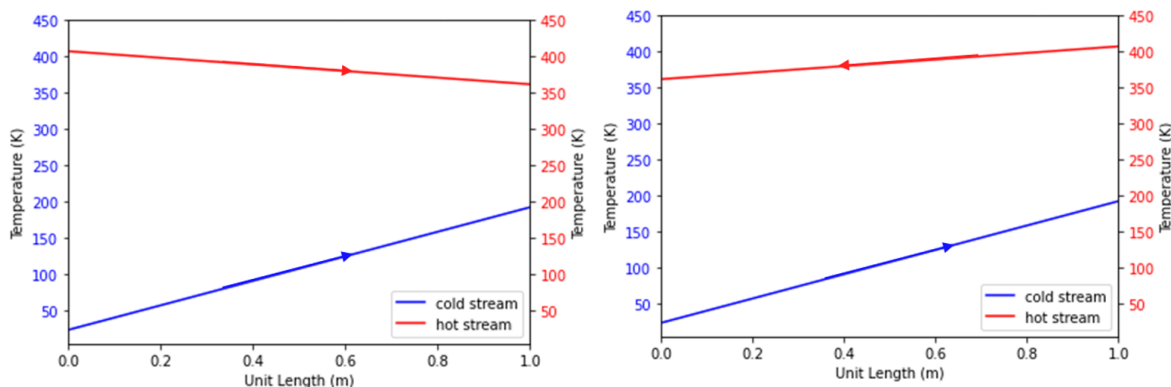


Figure 5.6: Intercooler flow configuration showing the left image as parallel-flow and the right image as counter-flow. The temperature variation lines are straight due to the assumption of a uniform and constant C_p for all temperature difference per unit length of the heat exchanger. The high ΔT of the hydrogen stream is due to the greater difference between the cryogenic storage temperature of hydrogen and the cold load required by the intercooler, resulting in a significant rise in the hydrogen outlet temperature.

Tables 5.10, 5.11, 5.12 and 5.13 provide the fin parameters, thermophysical and flow properties, heat transfer and pressure drop results and the overall size of the intercooler.

Table 5.10: Standardized Fin parameters of hot and cold side of Intercooler [94, 101].

Fin Parameter	Notation	Hot Side	Cold Side
Fin Thickness (m)	t_f	0.00025	0.00022
Fin Height (m)	h_f	0.01	0.003
Fin Density (fins/m)	d_f	600	600
Fin pitch (m/fin)	p_f	0.001667	0.001667
Cross sectional area per passage (m ²)	A_h	0.008288	0.002413
Fin perimeter (m)	P_f	13.4	5.072
Hydraulic diameter (m)	d_{hyd}	0.002474	0.0019
Primary heat transfer area (m ²)	A_1	1.7	1.736
Secondary heat transfer area (m ²)	A_2	11.7	3.336
Ratio secondary to total heat transfer	$\frac{A_2}{(A_1+A_2)}$	0.873	0.6577
Heat transfer area per single passage plate (m ²)	A_{sum}	13.4	5.072
Plate spacing (m)	h_p	0.01075	0.00372
Area Density (m ² /m ³)	β	1246.5	1363.4

Table 5.11: Thermophysical and flow properties of hot and cold fluid in Intercooler based on maximum operating point of fuel cell stacks [94, 101].

Property	Notation	Hot Side	Cold Side
Mean Temperature (K)	T_{mean}	384.75	108.4
Dynamic viscosity (Pa.s)	μ	0.000012335	0.0000044387
Specific heat capacity (J/kg.K)	C_p	2085	14130
Thermal conductivity (W/m.K)	k	0.025752	0.08947
Density (kg/m ³)	ρ	2.5498	0.33549
mass flow (kg/s)	\dot{m}	1.3	0.0538
mass flux (kg/m ² s)	G	100	10
Minimum Free flow area (m ²)	A_o	0.013	0.00538
Reynolds number	Re	20056	4287
Prandtl number	Pr	0.9988	0.701

Table 5.12: Heat Transfer and frictional pressure drop per unit length calculation results for Intercooler based on maximum operating point of fuel cell stacks.

Parameter	Notation	Hot Side	Cold Side
Darcy Friction factor	f	0.0261	0.0405
Nusselt Number	Nu	62.126	14.4
Heat transfer coefficient (W/m ² .K)	h	646.7	677.13
Fin efficiency	η_f	0.9049	0.9854
Overall surface efficiency	η_o	0.917	0.9904
Fluid unit Pressure Drop (Pa/m)	$\frac{\Delta p}{L}$	82747.2	12679.2

Table 5.13: Heat Transfer inputs Intercooler based on maximum operating point of fuel cell stacks [94, 101].

Parameter	Notation	Value
Plate thickness	δ_{wall}	0.0005
Plate conductivity (W/m.K)	k_{wall}	243
Overall heat transfer coefficient (W/m ² .K)	U	314.5
LMTD (K)	$\Delta T_{LMTD(\text{cross})}$	267.8
Heat Transfer surface area (m ²)	A	1.52
Intercooler volume (m ³)	$V_{(\text{PFHE})}$	0.00117
Unit weight (kg/m ³)	$\rho_{(\text{PFHE})}$	1000
Intercooler weight (kg)	$m_{(\text{PFHE})}$	1.17

Based on the obtained LMTD of both de-superheater and intercooler, one factor which needs to be looked upon in future research is the thermal stress generated inside the PFHE plates that separate both the fluids. Since the temperature difference between the fluids at the point of entry of the cold fluid is large, the difference in the thermal expansivity of the base plate material in practical scenarios could have the chances of developing thermal stresses.

5.4.3. Integrated Single Phase circuit cooling

The 4 FCHXs were individually designed using the same method, but using 52% ethylene glycol as the hot fluid. counter-flow configuration was chosen for these as, there is a possibility of a pinch point if parallel flow was considered. As the pinch point is at extreme right of the parallel flow heat exchanger, might still have the possibility of the pinch point to remain as its performance is in between the parallel flow and counter-flow. Also counter-flow configurations are more compact, which is necessary as number of components are greater for the VCRS + single phase system. The cold load distribution for FCHX 1, 2, 3, 4 are obtained as 72.8 kW, 70.88 kW, 68.9 kW, 66.86 kW respectively that are extracted and added up serially into the circulating ethylene glycol. The fin parameters used in Table 5.16 were kept same for all 4 of the FCHXs.

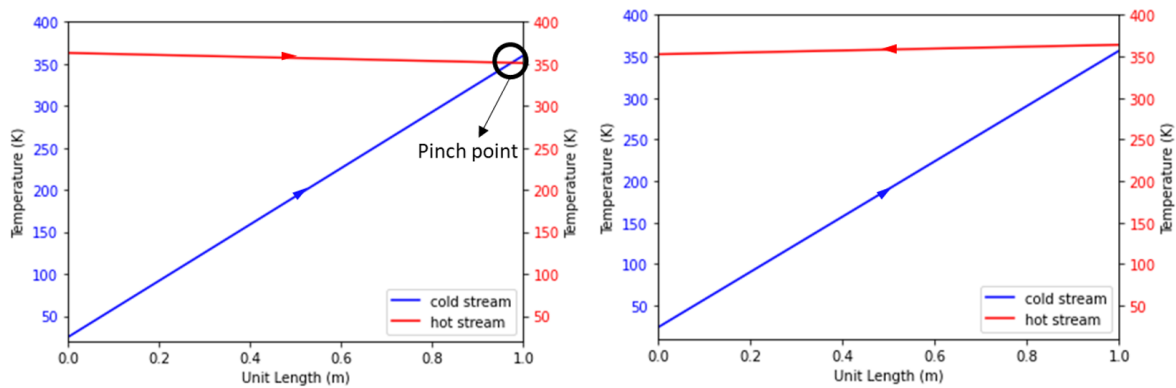


Figure 5.7: FCHX 1 flow configuration with parallel-flow in the left image showing a pinch point near the fluid exit where the heat transfer stops and after which the heat transfer is in reverse. Right image shows counter-flow configuration without any pinch point, meaning that the direction of heat transfer is consistent and therefore is a compatible configuration. The temperature variation lines are straight due to the assumption of a uniform and constant C_p for all temperature difference per unit length of the heat exchanger.

Tables 5.14 and 5.15 provide the parameters used in the energy balances of each of the FCHXs operating at different temperatures, Table 5.16 provide the same fin parameters of all the FCHXs.

Table 5.14: FCHX 1 and FCHX 2 conditions for energy balance. The hot fluid is 52% ethylene glycol and cold fluid is the H₂.

Parameter	FCHX 1 (Hot)	FCHX 1 (Cold)	FCHX 2 (Hot)	FCHX 2 (Cold)
Fluid	Glycol	H ₂	Glycol	H ₂
\dot{m} (kg/s)	2	0.01345	2	0.01345
Pressure (bar)	3.55	1.5	3.55	1.5
Inlet Temperature (K)	363	24	352.57	24
Outlet Temperature (K)	352.6	358	342.4	348
C_p (kJ/kg.K)	3.49	16.206	3.49	16.266

Table 5.15: FCHX 3 and FCHX 4 conditions for energy balance. The hot fluid is 52% ethylene glycol and cold fluid is the H₂.

Parameter	FCHX 3 (Hot)	FCHX 3 (Cold)	FCHX 4 (Hot)	FCHX 4 (Cold)
Fluid	Glycol	H ₂	Glycol	H ₂
\dot{m} (kg/s)	2	0.01345	2	0.01345
Pressure (bar)	3.55	1.5	3.55	1.5
Inlet Temperature (K)	342.4	24	332.54	24
Outlet Temperature (K)	332.5	338	323	328
C_p (kJ/kg.K)	3.49	16.315	3.49	16.352

Table 5.16: Standardized Fin parameters of hot and cold side of Intercooler [94, 101].

Fin Parameter	Notation	Hot Side	Cold Side
Fin Thickness (m)	t_f	0.00025	0.00022
Fin Height (m)	h_f	0.01	0.003
Fin Density (fins/m)	d_f	600	600
Fin pitch (m/fin)	p_f	0.001667	0.001667
Cross sectional area per passage (m ²)	A_h	0.008288	0.002413
Fin perimeter (m)	P_f	13.4	5.072
Hydraulic diameter (m)	d_{hyd}	0.002474	0.0019
Primary heat transfer area (m ²)	A_1	1.7	1.736
Secondary heat transfer area (m ²)	A_2	11.7	3.336
Ratio secondary to total heat transfer	$\frac{A_2}{(A_1+A_2)}$	0.873	0.6577
Heat transfer area per single passage plate (m ²)	A_{sum}	13.4	5.072
Plate spacing (m)	h_p	0.01075	0.00372
Area Density (m ² /m ³)	β	1246.5	1363.4

The parameters mentioned in Tables 5.17, 5.18 and 5.19 are only for FCHX 1. For all the four FCHXs calculations were performed with the same method as that for the FCHX 1 in Excel using data from REFPROP and [100].

Table 5.17: Thermophysical and flow properties of hot and cold fluid FCHX 1 based on maximum operating point of fuel cell stacks [94, 101].

Property	Notation	Hot Side	Cold Side
Mean Temperature (K)	T_{mean}	357.7	191
Dynamic viscosity (Pa.s)	μ	0.00105	0.0000657
Specific heat capacity (J/kg.K)	C_p	3490	16206
Thermal conductivity (W/m.K)	k	0.39	0.15174
Density (kg/m ³)	ρ	1045	0.198
mass flow (kg/s)	\dot{m}	2	0.01345
mass flux (kg/m ² s)	G	1500	23
Minimum Free flow area (m ²)	A_o	0.0013	0.000585
Reynolds number	Re	3534	6661
Prandtl number	Pr	9.396	0.701

Table 5.18: Heat Transfer and frictional pressure drop calculation results for FCHX 1 based on maximum operating point of fuel cell stacks.

Parameter	Notation	Hot Side	Cold Side
Darcy Friction factor	f	0.0431	0.0354
Nusselt Number	Nu	30.4	21.34
Heat transfer coefficient (W/m ² .K)	h	4792	1701.9
Fin efficiency	η_f	0.59	0.964
Overall surface efficiency	η_o	0.643	0.976
Fluid unit Pressure Drop (Pa/m)	$\frac{\Delta p}{L}$	74990.7	99249.2

Table 5.19: Overall sizing results of FCHX 1. The sizing of FCHX 2,3 and 4 were conducted similarly in Excel [94, 101].

Parameter	Notation	Value
Plate thickness	δ_{wall}	0.0005
Plate conductivity (W/m.K)	k_{wall}	243
Overall heat transfer coefficient (W/m ² .K)	U	1077.1
LMTD (K)	$\Delta T_{LMTD(\text{cross})}$	77.3
Heat Transfer surface area (m ²)	A	0.874
FCHX 1 volume (m ³)	$V_{(\text{PFHE})}$	0.0006712
Unit weight (kg/m ³)	$\rho_{(\text{PFHE})}$	1000
FCHX 1 weight (kg)	$m_{(\text{PFHE})}$	0.6712

Similarly after substituting the thermophysical properties for all 4 of the FCHXs, the total weight of the FCHXs combined was obtained as 2.84 kg.

5.4.4. System parasitic load

Compressor power consumption is critical as majority of the parasitic load is of the compressor itself. As the refrigerant methanol is unconventional for a VCRES system, customization of the compressor is necessary. Typical single staged refrigerant compressor efficiencies range between 70-90%, and the value generally considered is 80% [102]. The efficiency improves by around 10% when a 2-staged compressor is used. Considering 75% to be the single staged compressor efficiency, and a 6% improvement in the overall efficiency for a dual staged compressor, the stage efficiency would be 90%. Table 5.20 shows the power consumption results of the three type of thermal management systems, by keeping the Basic VCRES as a reference.

Table 5.20: Compressor power consumption results between Basic VCRS and the two cryogenic cold integrated systems. Constant compressor pressure ratio was considered for all three cases. The total compressor efficiency is fixed to 0.75 for single stage and 0.8 for overall efficiency of dual stage, giving stage efficiency 0.9.

Parameters	Basic VCRS	VCRS with In-tercooler & de-superheater	VCRS + single phase circuit
Compressor pressure ratio	3.85	3.85	3.85
Compressor efficiency	0.75	0.8	0.75
Stage ₁ outlet temperature (K)	-	407.5	-
Stage ₂ inlet temperature (K)	-	362	-
Outlet temperature (K)	493.3	418.3	465.4
Real Stage 1 Work (kW)	-	131.6	-
Real Stage 2 Work (kW)	-	158.8	-
Compressor power consumption (kW)	335.5	290.4	249.6
Pump efficiency (kW) [103]	-	-	0.5
Pump shaft power (kW) [104]	-	-	0.376
Total Work (kW)	335.5	290.4	249.976

The power consumption of the compressors have been oversized in the Table 5.20 above as calculations are made for an assumed constant compressor efficiency. As the additional thrust build up by the ram air to compensate for the drag is neglected during ground motion, the fuel cell power generation requirement has been oversized, and so is the fuel cell heat generation and the load requirements. Therefore rather than absolute values of system power consumption, the relative change in the power consumption is a better way to compare. A system with optimum integration technique is when there is a balance between the allowable LTPEMFC size due to the fuel cell over-sizing for the additional parasitic load and the overall compactness of thermal management system. As the assigned maximum auxiliary power that was declared initially during power generation calculations was 300kW, it is understood that integration of the cryogenic cold leads to a reduced parasitic load that is below the auxiliary power limit of the fuel cell, whereas the Basic VCRS system had a power consumption greater than the auxiliary power supply. This means that if cryogenic cold is integrated, fuel cell over-sizing to compensate for extra power requirements can be avoided.

5.4.5. Expansion valve

Expansion valve is responsible for providing the additional cooling effect in a VCRS system by bringing down the pressure of the refrigerant from the condenser saturation pressure back to evaporator saturation pressure, isenthalpically. The adjustment of expansion valve pressure ratio is based on the summation of compressor pressure rise and individual heat exchanger pressure drops.

To understand the level of cooling provided by the expansion valve, the JT coefficient (shown by equation 2.1) for the case of methanol was obtained using REFPROP. At 4.8 bar when methanol is in its subcooled phase, it has a negative JT coefficient of around -0.02 (K/bar) which lowers further when subcooled. In the saturated phase, the JT coefficient shoots up to a strictly positive value of ranging from 6.37 (K/bar) at condenser pressure and 17.11 (K/bar) at evaporator pressure. This is different for conventional refrigerants like R134a that have a positive liquid and vapor JT coefficient at their operating pressures such as 0.012 (K/bar) for subcooled liquid at 10 bar.

At the initial stages of isenthalpic pressure drop in the expansion valve, when the methanol is in sub-cooled region, there is a tendency of slight heating. However, the main function of the expansion valve is to drop the pressure, and the change in temperature is a function of the pressure drop. The drop in saturation temperature of methanol per unit drop in pressure (bar) outweighs the temperature rise, resulting in vaporization, of methanol. When the vapor phase starts forming during expansion, its strictly high JT-coefficient creates a resultant cooling effect on methanol.

5.5. Comparison of thermal management system results

The following results for the overall integrated thermal management systems were noted in Table 5.21 and compared with the basic VCRS system as a reference.

Table 5.21: Results from two types of Cryogenic Cold integration techniques compared to a basic VCRS.

Parameters	Basic VCRS	VCRS with Intercooler & FCHX	VCRS + single phase circuit
Fuel stacks heat load	1309.8	1309.8	1309.8
Fuel cell operating pressure (bar)	1.5	1.5	1.5
Compressor pressure ratio	3.85	3.85	3.85
Evaporator Inlet Vapor quality	0.1	0.1	0.1
Compressor efficiency	0.75	0.8	0.75
Outlet temperature (K)	493.3	418.3	465.4
Compressor work (kW)	335.5	290.4	249.6
Pump work (kW)	-	-	0.376
Total Work (kW)	335.5	290.4	249.976
Condenser load (kW)	1644.5	1350.4	1279.6
Condenser Temperature (K)	383	383	364
Extra components	-	1 FCHX + 1 inter-cooler	4 FCHX + 1 pump
Extra component weight (kg) [105]	-	2 + 1.17	2.85 + 1.151
Cooling agents	Methanol	Methanol	Methanol + 52% ethylene glycol
Mass flow (kg/s)	1.3	1.3	1.03 + 2

It can be observed that the condenser load reduces by 18% for the VCRS with intercooler and by 22% for the VCRS + single phase circuit. Based on the 12.5% (300 kW) of power generated by the fuel cell that is kept for auxiliary power supply such as pumps and compressors, the basic VCRS compressor power requirement crosses this value, but both the cooling circuits with cryogenic cold do not. The VCRS with intercooler system consumes 13.4% less power and the VCRS with the single phase circuit consumes around 26% less power, which is a significant drop in the parasitic load. This means that basic VCRS would need their fuel cell stack to be oversized by the extra amount of parasitic load requirement, that can involve additional heat release.

As per the weight addition to the VCRS, the system with intercooler and FCHX adds 3.17 kg of component weight only, but the system involving a single phase circuit will require 4 kg of component weight and a total of 3 kg/s coolant flowrate. The effect on system weight due to the coolant flow rate will depend on the size of the circuit based on its positioning, and can be reduced by placing the FCHXs and pumps near the fuel cell stacks.

5.6. Results for dynamic conditions of boil-off

The results for the boil-off rate and tank pressure variation have been plotted in Figure 5.8. The blue line in Figure 5.8 shows the vapor pressure in the transferring trailer and the orange line shows the vapor pressure in the fuel tank during and after fill. The set pressure of the regulator valve in line (5) is 1.7 bar, and the lockup pressure is 1.9 bar. This value can be changed as per the downstream pressure requirement for retrieving the BOG vapor. Based on the set objectives, only the fuel tank (ET) is focused in this thesis. The tank filling starts from 0 minutes and is completed at nearly 13 minutes. The wavy pattern shows the frequent opening and closing of the pressure regulator based on its set pressure and lockup pressure in allowing the boil-off vapor to pass through the BOG retrieval line (5) of Figure 3.3. It is observed that after the filling is complete the regulator closes and the tank pressure starts to drop towards the initial pressure of the tank before filling. This is due to the dampening of the dynamic effects in bringing the system back into its original state.

After the fill is complete, if the fuel is held for a short period of less than 15 minutes before starting the supply to the fuel cell, that is when the tank pressure is still higher than its initial condition, it can lead to a greater boil-off rate. There is a possibility of this high boil-off rate to exceed the fuel supply requirement, resulting in significant hydrogen losses. Additionally, the excess hydrogen can flood and potentially damage the fuel cell. This scenario is likely when the pressure relief valve threshold is set higher than the regulator's lock-up pressure.

If the fuel is held for a longer period before supply to the fuel cell, then the slight drop in tank pressure below the supply pressure as shown in Figure 5.8 beyond 20 minutes after complete filling, can generate a low fuel flow pressure to the cells. This is the duration when a pump might be required to start the supply of fuel until the tank pressure is built back to the supply pressure of 1.5 bar by the boil-off rate and vaporizer line.

Figure 5.9 shows a significantly high boil-off starting from 1.184 kg/s to 1.278 kg/s at the end of fill. This high boil-off cannot be supplied to the fuel cell system since the aircraft engine is not started during tank filling. Also the mentioned dynamic boil-off rate is higher than the maximum fuel cell anode reactant requirement, that can cause flooding of H_2 in the fuel cell and the H_2 recirculation line (25). Therefore it is evident that this BOG needs to be directed to the another application/ storage system through line (5). In the upcoming section 5.7, the results of the stand-alone fuel tank system is provided.

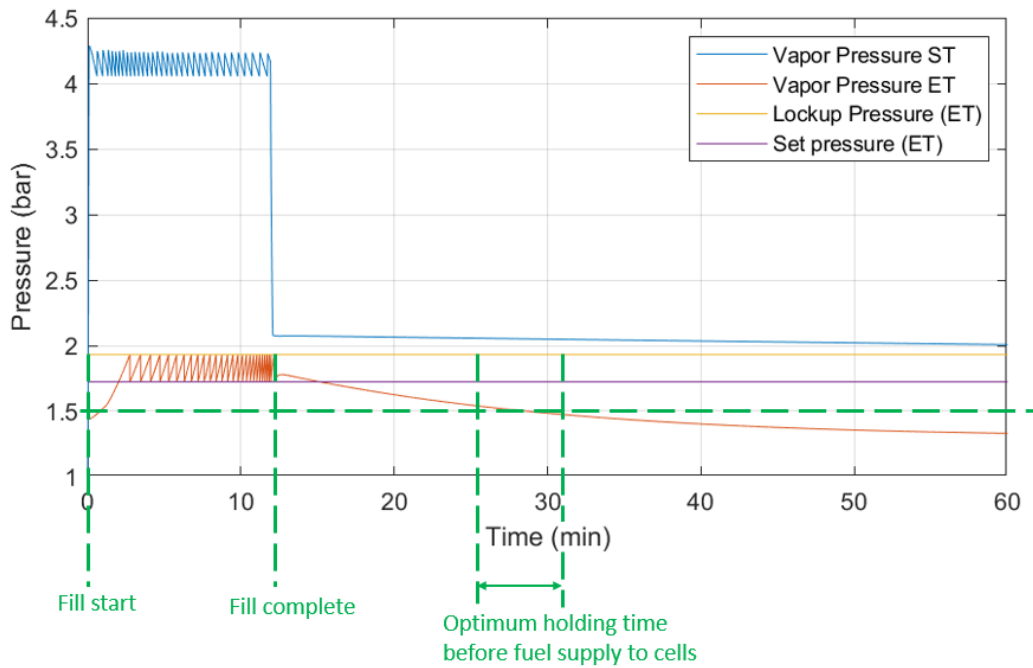


Figure 5.8: Pressure variation results due to dynamic effects during filling the fuel tank from the trailer. blue = vapor pressure of the transferring trailer (ST), orange = vapor pressure of the fuel tank (ET). The initial spike of pressure is due to the dynamic boil-off during the filling process. The flow pressure is shown by the difference in pressure between ST and ET for a particular time. The pressure starts dropping after fill is complete as the dynamic effects of filling are damped.

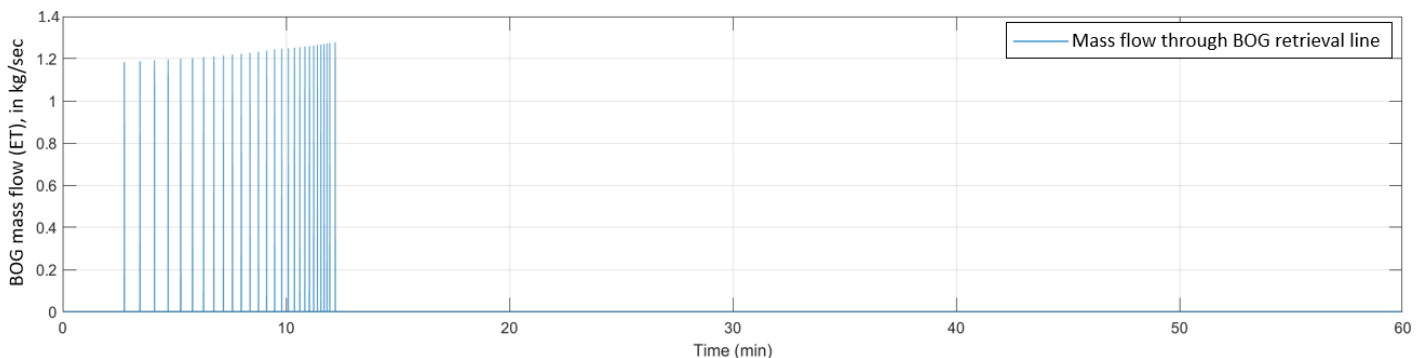


Figure 5.9: BOG rate (kg/s) variation results due to dynamic effects during filling the fuel tank from the trailer. The boil-off released through the retrieval line stops after fill is complete. It shows a significant boil-off rate during filling process compared to the boil-off after the filling is complete.

5.7. Results for stand-alone conditions of boil-off

The boil-off results obtained from the BoilFAST software are presented in this section. Sensitivity analysis of each: insulation thickness, initial tank pressure when the manual valve (13) is opened, and fill levels of the tank were conducted to understand how the boil-off rate changes by changing each of them one at a time. The chosen stand-alone tank condition out of all would be based on the case that the maximum boil-off rate should be lower than the minimum fuel supply requirement on ground, so that no BOG is lost through the safety pressure-relief system (3). The rest of the simulation parameters are kept as provided in the section 3.1.2 for a fair comparison. The calculated mass flowrate of anode reactant H_2 is 0.04037 kg/s per engine on ground during take-off. The results of BoilFAST at varying initial tank pressures for the fixed pressure regulator set pressure of 1.5 bar are shown in Figure 5.11, and compared to the boil-off rate when the initial tank pressure is same as the regulator set pressure of 1.5 bar, as shown in Figure 5.10.

The results obtained in Figure 5.10 for the initial tank pressure of 1.5 bar, show the boil-off rate in the stand alone tank during the 1st hour of the flight journey. The boil-off rate starts at a value of 0.0002643 kg/s and then gradually increases up to a maximum value of 0.000307 kg/s and becomes almost constant. This denotes a holding time of around 16 minutes after the tank is filled. In the top left image of Figure 5.11, the initial tank pressure of 1.49 bar means a holding time greater than 16 minutes after complete filling, and the plot shows an initial negative boil-off rate. At the start of the simulation, the tank pressure is 0.1 bar below the regulator pressure. The left image of Figure 5.12 shows the pressure changes in the tank from an initial pressure of 1.49 bar. Since the set pressure has not yet been reached till the first 9 minutes after filling, it means that the pressure regulator is closed and the tank pressure is lower than the supply pressure to the fuel cell. The boil-off rate for that time duration is negative, that is before the regulator ④ opens, because the dynamic effects are still diminishing, the reduction in the kinetic energy of the vapor molecules when in contact with the cold tank wall can cause condensation to outweigh the evaporation rate. In the top right image of Figure 5.11 the initial tank pressure is 0.01 bar higher than the set pressure, which results in an initial spike of BOG supply of 0.01981 kg/s to the fuel cell, which then drops down back to 0.000306 kg/s. The boil-off rate during the initial spike increases with the increase in initial tank pressure and thus with lower fuel holding times. It is the BOG mass flowrate caused by this initial spike that needs to be controlled and kept below the fuel cell supply requirement to be able to integrate the BOG with the fuel supply system.

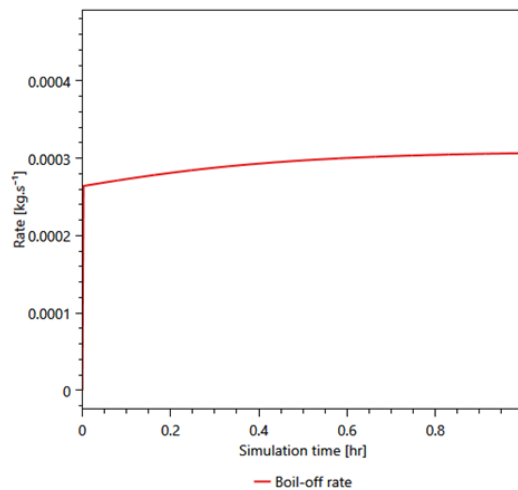


Figure 5.10: BOG rate (kg/s) at 1.5 bar initial tank pressure (same as pressure regulator set pressure). The boil-off rate is initially increasing till 24 minutes and then stabilizing.

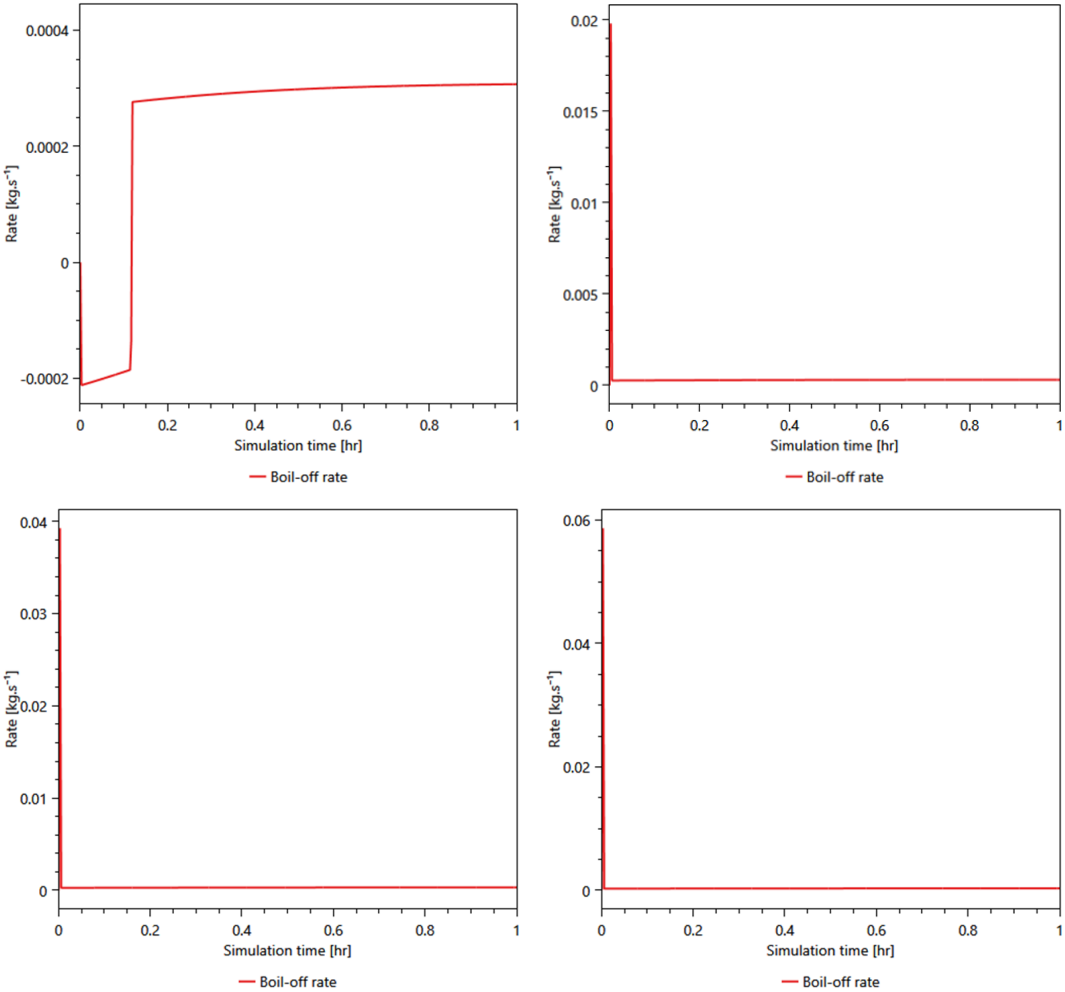


Figure 5.11: BoilFAST BOG rate results as per 1st hour of flight journey at varying initial tank pressures for the fixed pressure regulator set pressure of 1.5 bar. From upper left image to lower right image the initial tank pressures are 1.49 bar, 1.51 bar, 1.52 bar, 1.53 bar respectively.

The tank pressure variations for varying initial pressure conditions are shown in the Figure 5.12. The left image shows how the pressure increases in the tank as until it reaches the regulator's set pressure and then is maintained at that pressure. The right image shows the pressure variation that was obtained same for 1.5 bar and also for higher initial pressures, indicating that the pressure is maintained throughout when the initial condition is same or higher as the regulator's set condition.

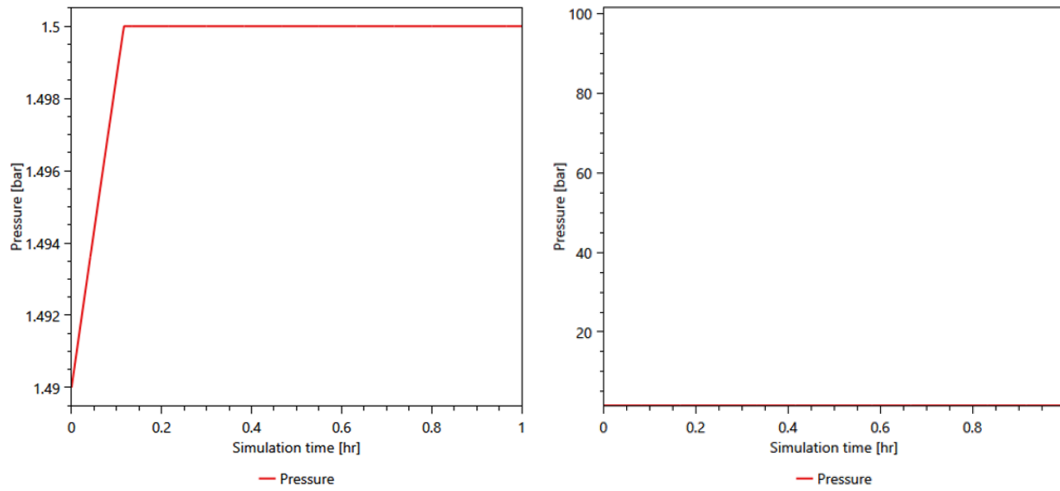


Figure 5.12: BoilFAST tank pressure variation results as per 1st hour of flight journey at lower and same initial tank pressures as the fixed pressure regulator set pressure of 1.5 bar. The left image is based on an initial tank pressure of 1.49 bar, and the right image shows no pressure variation as the tank pressure is held constant as its initial pressure of 1.5 bar.

The Table 5.22 shows the maximum boil-off rate based on initial tank pressure. The boil-off rate variation was also obtained with respect to % fill level of the LH₂, as shown in Table 5.23.

Table 5.22: Maximum boil-off rate for 1 hour duration with respect to initial tank pressure, for a regulator set pressure of 1.5 bar at 328K ambient. H₂ supply requirement in fuel cell stacks is 0.0538 kg/s, meaning that initial pressure beyond 1.53 bar for the given set pressure is not recommended.

Initial tank pressure (bar)	Maximum boil-off rate (kg/s)
1.49	0.000307
1.5	0.000307
1.51	0.01981
1.52	0.03928
1.53	0.05867

Table 5.23: Maximum boil-off rate for 1 hour duration with respect to % fill level of LH₂, for an initial tank pressure of 1.5 bar and regulator set pressure of 1.5 bar at 328K ambient.

% fill level	Maximum boil-off rate (kg/s)
90	0.000307
80	0.0002849
70	0.0002614
60	0.0002381
50	0.0002153
40	0.0001929
30	0.0001707
20	0.0001488
10	0.0001269

Maximum boil-off obtained in Table 5.23 is at initial fill level of 90%, because for a fixed inner surface area of the tank, as the liquid has more contact area than the vapor, the total heat transfer in liquid

phase is greater than in the vapor phase as shown in Figure 5.13, possibly due to higher thermal conductivity of liquid (0.10129 (W/m.K)) than vapor (0.020404 (W/m.K)) at 24K, 1.5 bar, assuming that the convection currents in vapor and liquid are not as dominant due to thermal stratification. The heat transfer rate is least though the interface because the heat transfer direction is only within the vapor and liquid. This is because the contact area of interface with the tank is least (a line).

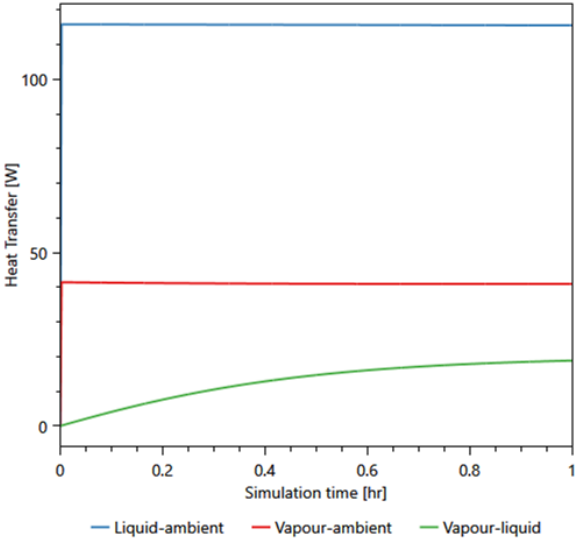


Figure 5.13: Ambient Heat Ingress (W) into the phases separately, liquid (blue), vapor (red) and interface (green). Showing highest heat transfer rate into liquid, then to vapor, and the least through the vapor-liquid interface.

6

Conclusions and Recommendations

It can be concluded that there is a significant potential in the available cryogenic cold to reduce the thermal management system load. But it comes with a drawback of additional system component weight such as the heat exchangers and pump. Regarding the selection of the type of cryogenic cold integration technique, it will depend on the priorities of the aviation sector: acceptability of additional parasitic load or additional component weight.

To further conclude, the boil-off integration system designed works, as the boil-off rates obtained are lower than the fuel supply requirements. If not, the fuel holding time can be varied to obtain the acceptable boil-off release rate through the pressure regulator into the fuel cell system.

While simulations provide valuable insights into the behavior of LH₂ in fuel tanks, experimental validation is necessary to ensure accuracy and reliability. Simulations generally rely on assumptions and models that may not involve the complexities of real-world scenarios. The real-world scenario is not fully captured as sloshing effects were neglected. As the intensity of sloshing varies based on journey, experimental tests are needed involving sloshing effects due to flight turbulence in the upcoming research.

The drawback of the MATLAB simulation was the manual input of grid parameters for the scaled-down version of the code, that resulted in convergence issues for large grid sizes. Even if the code for the large scale system is validated, and the trend of the fluid pressure behaviour for the scaled down system is similar to the large scale system, it is difficult to rely on a numerical validation as grid parameters were selected on a trial and error basis, rather than self-adaptive meshing techniques. Therefore experimental validation is also required for modelling the boil-off rate in the scaled down version.

Changing the type of insulation and studying its material behaviour is not within the scope of this thesis, as the heat fluxes in the MATLAB code were considered after it crossed the insulation. For the Boil-FAST software self-pressurization tests, the insulation used was made up of 2 blankets of MLI, each with 17 Mylar layers and the thickness was not stated [10].

The effect on the addition of coolant mass flowrates will depend on the piping length, and the time it takes for a unit coolant to cross the entire circuit. If the FCHX is located near to the fuel cell stacks (on the wings) and the pump below the cabin walkway in the part of the fuselage near to the aircraft wings, then the overall size of the single phase circuit would be less, requiring less overall mass of ethylene glycol. The compactness of the fluid flow in pipelines for the single phased circuit is greater than the methanol VCRS because the density of 52% ethylene glycol is 32% more than the density of liquid methanol. This will require lower volume flowrates of the ethylene glycol, requiring less pipeline cross-sectional area for the same speed,

The compressor were oversized based on power consumption, because the drag considerations and the addition of thrust by the ram-air was not considered. The ram air thrust needs to be separately

studied as it exists due to the aircraft speed during the maximum operating point, that is during take-off. Also the real outlet temperature from the compressor would vary in real-life based on the variation in efficiency. Also the fuel cell performance and heat generation variation need to be used to understand how effective this system would be at high altitudes, with reduced air temperature, pressure and oxygen concentration. Due to the reduced oxygen concentration, the power consumption of additional blowers to adjust the suction air into the fuel cell to maintain cathode reactant supply needs to be studied.

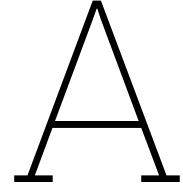
The compatibility of the cryogenic heat exchangers for large LMTD needs to be studied, as the large temperature difference between the two fluids at a particular length of the PFHE can cause thermal stresses due to the difference in the thermal expansivity of corrosion resistant-coated aluminium separating plates. The thermal expansion of Aluminium alloys is around -0.4% obtained from [106]. The surface of the plate touching the cryogenic fluid can experience thermal contraction and the surface touching the hot fluid will experience thermal expansion, causing thermal stress variation across the plate cross-section. Therefore even if the temperature experienced is within the operable range, experimental tests on the effect of large LMTD on cryogenic heat exchangers is recommended.

The consideration of ortho-para conversion will be based on the duration of the LH₂ in transporting from the liquefaction plant to the fuel tank, holding time of the fuel tank after fill up and the duration of the flight. For long-term storage, converting hydrogen to parahydrogen is essential to avoid excessive boil-off caused by the exothermic conversion from ortho-hydrogen. This forced conversion during liquefaction requires additional energy input. Since the spontaneous conversion is slow, the extent of conversion needed depends on how soon the hydrogen will be used. For instance, if the hydrogen will be used within 19 hours after liquefaction, it is more economical to liquefy it without increasing the parahydrogen content significantly [107]. A 100% parahydrogen was considered in this work, leaving no possibility of boil-off resulting from the exothermic, spontaneous but slow rate of ortho-para conversion and keeping in mind that there will always be a possibility of delay in transportation and holding time of the fuel. For undesired residues of ortho content in the filled hydrogen in tank, a separate study needs to be considered to obtain boil-off rates for different initial ortho compositions.

As this study used the cryogenic cold into thermal management system for half of the fuel cell stacks of 1 propulsion unit, the drop in ram air-cooled condenser load increases the chances of using the condenser for also cooling the other 2 stacks. Just the way the cryogenic fuel and the ram air was used as a heat sink, other potential passive heat sinks are needed to be discovered to improve the thermal management of the fuel cells.

The material compatibility of the valve components at cryogenic temperatures, such as the flexibility of diaphragms used in pressure regulators and the sensitivity of sensors and pressure-relief systems need to be tested.

After all the recommendations made in this section get satisfied in the upcoming research, a cost benefit analysis will need to be considered. This would include costs of the system design, installation, operation, and maintenance. Benefits of implementing the system will need to be studied which would include savings from reduced hydrogen loss, enhanced fuel cell efficiency, and reduction in cooling system costs. The return on investment (ROI) for the BOG integrated fuel supply system and of the fuel cell thermal management system after incorporating the additional components for the cryogenic cold would need to be individually calculated.



Appendix

This section can be used for referring to the additional details of the thesis.

A.1. Choked Flow Equations

To calculate the mass flow rate of boil-off that is getting released from the pressure relief valves, the following choked flow equations for compressible fluids can be used [24]. This is when sonic speed ($Ma = 1$) is considered through the minimum cross-section of the valve.

$$J_{valve} = \frac{\Gamma P_o A_{c(min)}}{\sqrt{\gamma R T_o}} \quad (A.1)$$

where the following equation can be substituted for Γ .

$$\Gamma = \gamma \left(\frac{2}{\gamma + 1} \right)^{\frac{\gamma + 1}{2(\gamma - 1)}} \quad (A.2)$$

P_o and T_o are the stagnation pressure and temperature equal to the internal vessel conditions if the flow is assumed isentropic, $A_{c(min)}$ is the minimum flow cross-section area, γ is the specific heat ratio,

A.2. Heat Ingress in non-spherical tanks

For non-spherical tanks, the paths of heat ingress was segregated into 3 sections: through top of the tank, through the wall of the tank, and through the bottom of the tank.

Assuming a disc shaped roof, the heat ingress through the roof of the tank can be determined by:

$$Q_{top} = \frac{-\pi \cdot r_{out}^2 \cdot (T_{in} - T_{out})}{\frac{1}{h_{c(in)}} + \sum_{i=1}^n \frac{x_i}{k_i} + \frac{1}{h_{c(out)}}} \quad (A.3)$$

where Q_{top} is the heat ingress through the roof of the storage tank, $i = 1, 2, 3 \dots n$, where n is the total number of insulation layers, x_i is the thickness of each layer of insulation involving the tank wall with units in m, k_i is the heat conductivity of each insulation layer involving the tank wall, $h_{c(in)}$ and $h_{c(out)}$ are the inner and outer convective heat transfer coefficient respectively, r_{out} is the outer radius of the tank, T_{in} is the temperature of the near wall fluid inside the tank, T_{out} is the temperature of the near wall fluid outside the tank, usually the ambient temperature. Heat transfer through the side wall can be determined considering cylindrical sides:

$$Q_{wall} = \frac{-2\pi \cdot H \cdot (T_{in} - T_{out})}{\frac{1}{r_{in} \cdot h_{c(in)}} + \frac{1}{k_1} \cdot \ln\left(\frac{r_1}{r_{in}}\right) + \sum_{i=2}^n \frac{1}{k_i} \cdot \ln\left(\frac{r_i}{r_{i-1}}\right) + \frac{1}{r_{out} \cdot h_{c(out)}}} \quad (A.4)$$

where Q_{wall} is the heat ingress through side walls of the storage tank, r_i radius of each individual tank insulation layers, H is the tank height, Similarly heat transfer through the bottom of the tank is as follows:

$$Q_{bottom} = \frac{-\pi \cdot r_{out}^2 \cdot (T_{in} - T_g)}{\frac{1}{h_{c(in)}} + \sum_{i=1}^n \frac{x_i}{k_i} + \frac{1}{h_{c(g)}}} \quad (\text{A.5})$$

where Q_{bottom} is the heat ingress through the bottom of the storage tank, T_g is the temperature of the ground contact of the tank, $h_{c(g)}$ is the bottom convective heat transfer coefficient.

The total heat ingress from ambient is found by adding the heat transfer in all the three parts of the tank:

$$Q_{in} = Q_{top} + Q_{wall} + Q_{bottom} \quad (\text{A.6})$$

A.3. Altitude effects on Fuel Cell performance

Understanding the effects of high-altitude conditions on fuel cell performance is important. High-altitude environments impact fuel cells through a complex interplay of physical, chemical, and electrochemical processes. These processes are generally characterized by considering the theoretical (Nernst) potential and three types of cell polarization (activation, ohmic, and concentration), all of which can be influenced by high-altitude conditions. A precise understanding of how these conditions affect both the fuel cell potential and polarizations is essential for designing aerospace fuel cell systems.

When maintaining a constant concentration of oxygen in the reactant stream, the primary impact of reduced total pressure operation is a decline in performance. At a specific voltage, the fuel cell generates less power; alternatively, at a fixed power output, irreversible losses increase, leading to lower voltage and efficiency. Both total pressure and oxygen concentration influence the partial pressure of oxygen according to Raoult's law as shown in equation A.7.

$$p_{O_2} = x_{O_2} \cdot P_T \quad (\text{A.7})$$

where p_{O_2} is the partial pressure of oxygen, x_{O_2} is the mole fraction of oxygen and P_T is the total pressure. Therefore, reducing either the concentration of oxygen or the total pressure will reduce the partial pressure. Partial pressure is generally used in the Nernst equation as follows:

$$E = E^\circ + \frac{R \cdot T}{n \cdot F} \ln \frac{p_{H_2} \sqrt{p_{O_2}}}{p_{H_2O}} \quad (\text{A.8})$$

where E is the cell potential, E° is the standard cell potential, n is the number of moles of electrons transferred, p_{H_2} and p_{O_2} are the partial pressure of the reactants hydrogen and oxygen respectively, and p_{H_2O} is the partial pressure of product water. It is tempting to believe that partial pressure is responsible for fuel cell performance changes without individually considering the changes in oxygen concentration and total pressure. For instance, two cases are considered in the paper by Joseph et al. [74]. First case is that if the partial pressure of oxygen is 1 bar with oxygen mole fraction as 1, the total pressure is also 1 bar. The second case is also with a partial pressure of oxygen as 1 bar but with a different oxygen mole fraction of 0.21 bar (oxygen concentration at sea-level) giving a total pressure of 4.8 bar. Although the partial pressures are the same in the two cases, the performance of the fuel cell varies. Therefore it can be understood that, rather than the partial pressure being the sole reason for understanding the variation of fuel cell performance, both concentration of the reactant and the total pressure should be individually considered.

A.4. Defrosting of fuel cooled heat exchangers at regular intervals

Although the thermophysical properties are assumed uniform throughout the heat exchanger length, in practical scenarios, they vary. After long use of cryogenic heat exchangers, due to undesired changes in the thermophysical and material properties such as specific heat and thermal conductivity, the localized heat transfer coefficients can vary causing inefficiencies in homogeneously transferring heat through the heat exchanger plate. Localized frost can form in the hot fluid side and if left over for a long duration, it can lead to blockage. To avoid this, individual FCHX would need to be de-frosted, by bypassing the hydrogen sub-stream one at a time to the extra FCHX (b5) in Figure A.1.

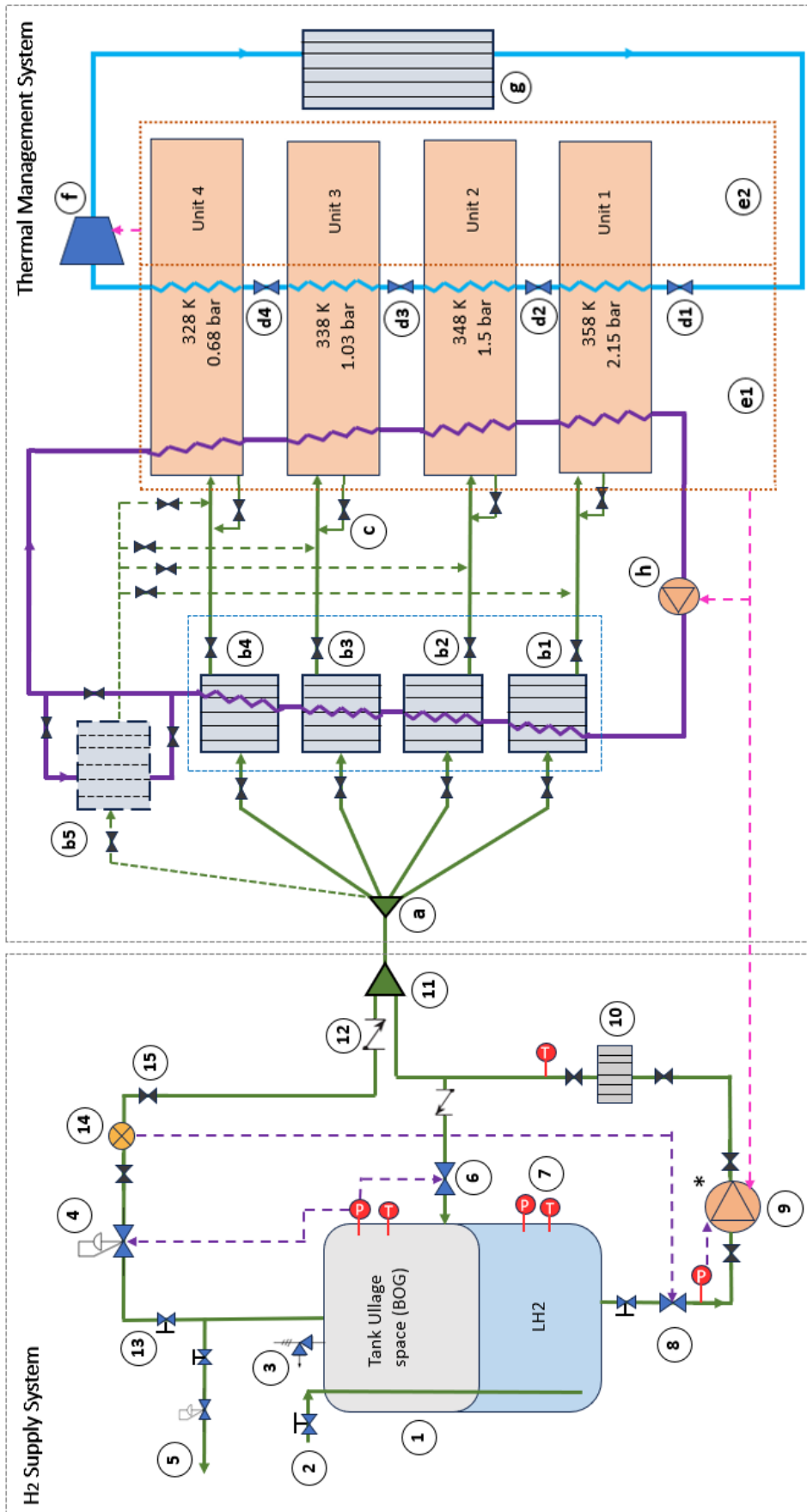


Figure A.1: Process flow diagram of the Integrated thermal management system with Single phase coolant circuit + VCRS, showing an additional FCHX labelled as 'b5' to function when each of the main FCHX is defrosted in a cyclic manner.

A.5. Logarithmic mean temperature difference correction factors

A.5.1. De-superheater

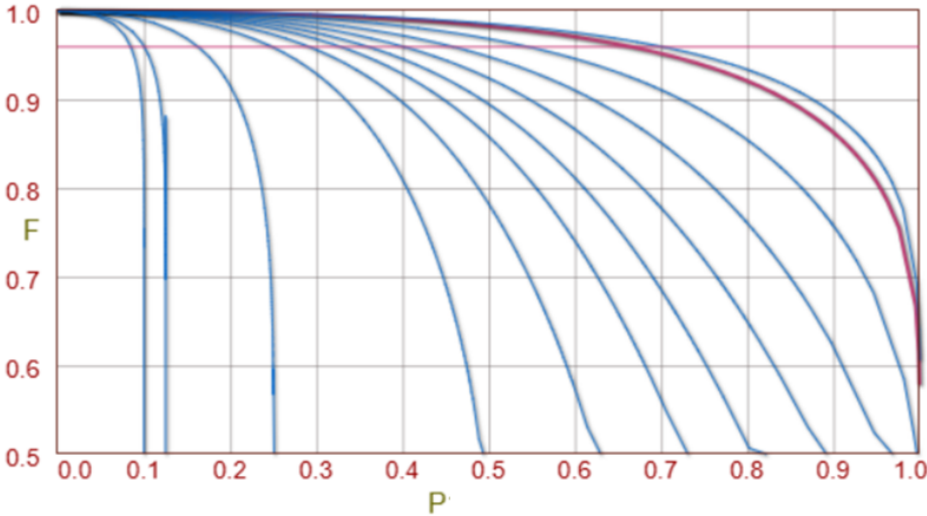


Figure A.2: LMTD correction factor ($F = 0.9592$) shown by the faint red horizontal line for a cross-flow configuration of FCHX with both fluids unmixed.

A.5.2. Intercooler

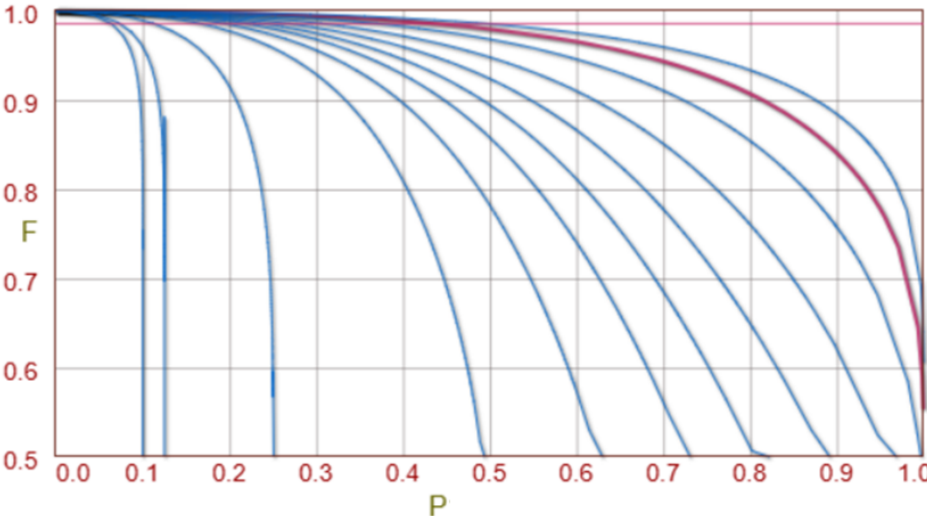


Figure A.3: Graph showing the LMTD correction factor ($F = 0.9857$) shown by the faint red horizontal line for a cross-flow configuration of intercooler with both fluids unmixed.

A.6. Aircraft Dimensions

The Bombardier Dash8 Q300, occupying up to 56 passengers, almost has a circular cross-section with a fuselage diameter of 2.69 m and a cabin width of 2.51 m [108]. This study only focuses on the Propulsion Unit 1 which consists of 4 stacks of fuel cells, 2 of which involves a ram air-cooled thermal management system, with ram air-cooled heat exchangers situated on both sides of the nacelle.

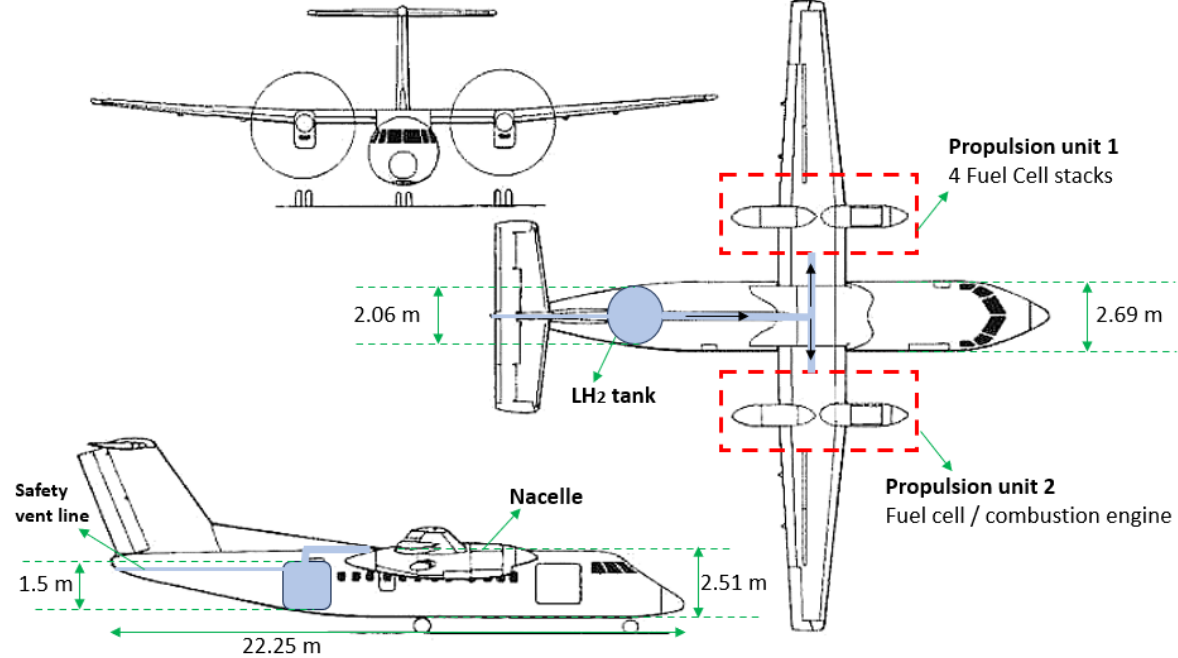


Figure A.4: Bombardier Dash 8 Q300 flight dimensions. The aircraft template was referred from [109].

References

- [1] Saif ZS. Al Ghafri, Stephanie Munro. "Hydrogen liquefaction: a review of the fundamental physics, engineering practice and future opportunities". In: 2022.
- [2] Muhammad Aziz. "Liquid Hydrogen: A Review on Liquefaction, Storage, Transportation, and Safety". In: MDPI, 2021.
- [3] Richard Folkson. "Hydrogen as an energy vector for transportation vehicles". In: *Alternative Fuels and Advanced Vehicle Technologies for Improved Environmental Performance*. 2nd ed. Woodhead Publishing Series in Energy, 2022, pp. 151–171.
- [4] K. Ohira. "3 - Slush hydrogen production, storage, and transportation". In: *Compendium of Hydrogen Energy*. 2016, pp. 53–90.
- [5] Jan Groznik. "Technologies of hydrogen liquefaction, transport and storage- Paving the way to a hydrogen fueled future". In: *Kawasaki Technical Review*, 2016.
- [6] Laurens Van Hoecke , Ludovic Laffineur. "Challenges in the use of hydrogen for maritime applications". In: MDPI, 2021.
- [7] Markus ReuB, Martin Robinius. "Seasonal storage and alternative carriers: A flexible hydrogen supply chain model". In: 2017.
- [8] Mihai Ursan. "What is boil-off?" In: United Nations Economic Commission for Europe, 2011.
- [9] N.T.Stetson S.McWhorter. "1 - Introduction to hydrogen storage". In: Woodhead Publishing, 2016, pp. 3–25.
- [10] Saif Z S Al Ghafri, Adam Swanger. "Modelling of Liquid Hydrogen Boil-Off". In: vol. 15. MDPI, 2022.
- [11] Ergenics Wyckoff. *Capture of Liquid Hydrogen boil-off with metal hydride absorbers*. Tech. rep. NASA, 1984.
- [12] Polly Martin. "Solving the liquid hydrogen boil-off problem US awards 48m towards H2 research and development". In: *Hydrogen news and intelligence | Hydrogen Insight (2023)*.
- [13] Aljazeera. "Mapping the hottest temperatures around the world". In: (2023).
- [14] *NIST Chemistry WebBook, SRD 69*. U.S. Department of Commerce.
- [15] Andreas Zuttel. "Materials for Hydrogen storage". In: vol. 6. 9. NASA, John F. Kennedy Space Center, 2003, pp. 24–33.
- [16] Patrick Molloy. "Run on Less with Hydrogen Fuel Cells". In: *RMI (2019)*.
- [17] Pamela Ramirez Vidal, Giuseppe Sdanghi, Alain Celzard. "High hydrogen release by cryo-adsorption and compression on porous materials". In: 2022, pp. 8892–8915.
- [18] Jan Groznik. "Boil-off gas handling from liquefied hydrogen storage". In: Norwegian University of Science and Technology, 2020.
- [19] Federico Ustolin, Alessandro Campari. "An Extensive Review of Liquid Hydrogen in Transportation with Focus on the Maritime Sector". In: MDPI, 2022.
- [20] Robert C. Hendricks , Ildiko C. Peller , Anne K. Baron. "Joule-Thomson Inversion Curves and related coefficients for several simple fluids". In: NASA, 1972.
- [21] L Bonadio. "Fuels – Hydrogen Storage | Liquid". In: *Encyclopedia of Electrochemical Power Sources*, 2009.
- [22] Christoph Windmeier, Randall F. Barron. "Cryogenic Technology". In: *Ullmann's Encyclopedia of Industrial Chemistry*. Wiley-VCH Verlag GmbH Co. KGaA, 2013.
- [23] Guillaume Petitpas. *Boil-off losses along the LH2 pathway*. Tech. rep. Lawrence Livermore National Laboratory, 2018.

- [24] L. X. Jia, L. Wang. "Equations for gas releasing process from pressurized vessels in ODH Evaluation". In: Cryogenic Engineering Conference in Madison, 2001.
- [25] Octave Levenspiel. "The Three Mechanisms of Heat Transfer: Conduction, Convection, and Radiation". In: *Engineering Flow and Heat Exchange*. The Plenum Chemical Engineering Series. Springer, 1984.
- [26] Daehoon Kang, Daehoon Kang, Bo-kyong Kim. "Review of the Liquid Hydrogen Storage Tank and Insulation System for the High-Power Locomotive". In: vol. 15. 2022.
- [27] T Wlodek. "Analysis of boil-off rate problem in Liquefied Natural Gas (LNG) receiving terminals". In: IOP Earth and Environmental Science, 2019.
- [28] McIntosh G.E. *Layer by Layer MLI Calculation Using a Separated Mode Equation*. Vol. 39. Springer, Boston, 1994.
- [29] Minsuk Kang, Juwon Kim. "Experimental investigation of thermal stratification in cryogenic tanks". In: 2018.
- [30] Gavin P. Towler, Ray Sinnott. "Heat Transfer Equipment". In: *Chemical Engineering Design*. 2nd ed. 2012.
- [31] Ismael Rodriguez Maestre, Juan José Gómez Sánchez, Francisco Javier González Gallero. "Performance analysis of natural convection correlations for spheres at high Rayleigh numbers". In: vol. 168. 2021.
- [32] Fardin Ghaffari-Tabrizi, Jan Haemisch, Daniela Lindner. "Reducing Hydrogen Boil-Off Losses during Fuelling by Pre-Cooling Cryogenic Tank". In: MDPI, 2022.
- [33] Ebenezer Adom, Xianda Ji, Sheikh Zahidul Islam. "Modelling of Boil-Off Gas in LNG Tanks: A Case Study". In: 2010.
- [34] Holyst and Poniewierski. "Phase transitions in pure substances". In: Springer, 2012.
- [35] Takuji Hanada, Kunihiro Takahashi. "Liquid-Hydrogen Storage". In: vol. 2. Encyclopedia of Life Support Systems.
- [36] Hendrie Derking, Luuk van der Togt. "Liquid Hydrogen Storage: Status and Future Perspectives". In: Cryoworld, Advanced Cryogenics, 2019.
- [37] Tim Burschyk, Yannic Cabac, Daniel Silberhorn and Brigitte Boden, Björn Nagel. "Liquid hydrogen storage design trades for a short-range aircraft concept". In: vol. 14. Springer, 2023, pp. 879–893.
- [38] Jing-Jie Ren, Jian-Yun Shi. "Simulation on thermal stratification and de-stratification in liquefied gas tanks". In: 2013.
- [39] Jeff Robbins, A. C. Rogers Jr. "An analysis on predicting thermal stratification in liquid hydrogen". In: 1966.
- [40] S. Prasanth Kumar, B.V.S.S.S. Prasad, G. Venkatarathnam. "Influence of surface evaporation on stratification in liquid hydrogen tanks of different aspect ratios". In: vol. 32. 2007, pp. 1954–1960.
- [41] Viatcheslav V Osipov, Matthew J Daigle, Cyrill B Muratov. "Dynamical Model of Rocket Propellant Loading with Liquid Hydrogen". In: 2011.
- [42] V.V. Osipov, C.B. Muratov. "Dynamic condensation blocking in cryogenic refueling". In: 2009.
- [43] Guomeng Wei, Jianfei Zhang. "Numerical Study of the Filling Process of a Liquid Hydrogen Storage Tank under Different Sloshing Conditions". In: vol. 8. 2020, p. 1020.
- [44] Rainer Kurz, Bernhard Winkelmann, Sebastian Freund. "Transport and storage". In: 2022.
- [45] Jessie R Smith, Savvas Gkantonas. "Modelling of Boil-Off and Sloshing Relevant to Future Liquid Hydrogen Carriers". In: MDPI, 2022.
- [46] Helvines Corazon Aquino, Akira Sou. "Sloshing of LNG and Liquid Hydrogen in Rectangular Tanks". In: 2016. ISBN: 978-1-880653-88-3.
- [47] Zhan Liu, Yuyang Feng, Gang Lei. "Fluid sloshing dynamic performance in a liquid hydrogen tank". In: 2019.

- [48] Adam Swanger James E. Fesmire. "Overview of the New LH2 Sphere at NASA Kennedy Space Center". In: NASA Kennedy Space Center, Cryogenics Test Laboratory, KSC, FL 32899 USA, 2021.
- [49] A.K. Majumdar, T.E. Steadman, J.L. Maroney. "Numerical Modeling of Propellant Boiloff in Cryogenic Storage Tank". In: NASA, 2007.
- [50] J Fesmire, A Swanger, J Jacobson. "Energy efficient large-scale storage of liquid hydrogen". In: IOP Conf. Series: Materials Science and Engineering, 2022.
- [51] W U Notardonato, A M Swanger, J E Fesmire. "Zero boil-off methods for large-scale liquid hydrogen tanks using integrated refrigeration and storage". In: IOP Conference Series: Materials Science and Engineering, 2017.
- [52] Bob Granath. "Innovative Liquid Hydrogen Storage to Support Space Launch System". In: NASA, 2018.
- [53] Zuo Zhongqi, Jiang Wenbing, Huang Yonghua. "Effect of baffles on pressurization and thermal stratification in cryogenic tanks under micro-gravity". In: 2018.
- [54] Joachim Wolf. "Liquid-Hydrogen Technology for Vehicles". In: MRS Bulletin 27, 2002, pp. 684–687.
- [55] Araceli Guadalupe Romero-Izquierdo, Claudia Gutierrez-Antonio. "Advanced biorefineries for the production of renewable aviation fuel". In: 2022.
- [56] Donghoi KIM, Stian TRÆDAL, David BERSTAD. "Hydrogen Re-liquefaction Process for Boil-off Gas Handling on a Large-scale Liquid Hydrogen Carrier". In: The 17th Cryogenics 2023, IIR Conference, 2023.
- [57] "Cryocap- Carbon Capture Technologies". In: Air Liquide, Engineering and Construction, 2023.
- [58] "CO2 reduction through storage under the North Sea". In: Porthos CO2 Transport and Storage C.V., 2023.
- [59] Ajsa Habibic. "Air Liquide to install CO2 capture unit at hydrogen plant in Rotterdam port". In: Offshore Energy, 2023.
- [60] Ajsa Habibic. "Air Products to build carbon capture facility at existing hydrogen plant in Rotterdam". In: Offshore Energy, 2023.
- [61] *ZEROe: Towards the world's first hydrogen-powered commercial aircraft*. Tech. rep. Airbus, 2024.
- [62] Ho Lung Yip , Ales Srna. "A Review of Hydrogen Direct Injection for Internal Combustion Engines: Towards Carbon-Free Combustion". In: *MDPI Applied Sciences* (2019).
- [63] "Hydrogen fuel cells and combustion engines". In: *Volvo* (2024).
- [64] Ziyad Salameh. *Renewable Energy System Design*. Academic Press, 2014.
- [65] James Larminie , Andrew Dicks. *Fuel Cell Systems Explained*. Wiley, 2003.
- [66] Bhaskar Balasubramanian , Frano Barbir. "Optimal operating temperature and pressure of PEM fuel cell systems in automotive applications". In: 44 (1999).
- [67] Mohamed Mamlouk Suthida Authayanun. "Comparison of high-temperature and low-temperature polymer electrolyte membrane fuel cell systems with glycerol reforming process for stationary applications". In: *Applied Energy* (2013).
- [68] Antje Link, Jonas Ludowicy, Martin Staggat. "Assessment of a serial cooling concept for HTPEM fuel cell system for aviation applications". In: *ICAS* (2022).
- [69] Airbus. "First ZEROe engine fuel cell successfully powers on". In: (2024).
- [70] Ryan P. O'Hayre. "Fuel cells for electrochemical energy conversion". In: *EPJ Web of Conferences* (2016).
- [71] Toshiki SATO. "Recent Development Trends in Materials for Bipolar Plates of Proton Exchange Membrane Fuel Cells (PEMFCs) and Kobe Steel's Activities". In: *Kobelco Technology Review* (2023).

- [72] Joseph W. Pratt , Jacob Brouwer. "Performance of Proton Exchange Membrane Fuel Cell at High-Altitude Conditions". In: *Journal of Propulsion and Power* (2007).
- [73] Jay T. Pukrushpan , Huei Peng. "Simulation and Analysis of Transient Fuel Cell System Performance Based on a Dynamic Reactant Flow Model". In: *IMECE* (2002).
- [74] Joseph W. Pratt , Jacob Brouwer. "Performance of Proton Exchange Membrane Fuel Cell at High-Altitude Conditions". In: *Journal of Propulsion and Power* (2007).
- [75] Bahman Shabani Huy Quoc Nguyen. "Proton exchange membrane fuel cells heat recovery opportunities for combined heating/cooling and power applications". In: *Energy Conversion and Management* (2020).
- [76] Nicholas A. Klymyshyn , Kriston Brooks. "Methods for Estimating Hydrogen Fuel Tank Characteristics". In: *Journal of Pressure Vessel Technology* (2023).
- [77] John Turner, Stephanie Contaut. "Cryogenic Hydrogen Fuel System and Storage". In: (2022).
- [78] *BoilFAST – new free software tool to model boil-off production*. 2021.
- [79] Antonio Scoccimarro. "Preliminary Design Methods for the Thermal Management of Fuel Cell Powered Aeroengines". MA thesis. Aerospace Engineering, Delft University of Technology, 2023.
- [80] "How To Estimate Required Fuel Flow For PEM Cells". In: *Scribner LLC* (2017).
- [81] Ronald M. Dell, Patrick T. Moseley , David A.J. Rand. "Hydrogen, Fuel Cells and Fuel Cell Vehicles". In: *Towards Sustainable Road Transport Book* (2014).
- [82] "Fuel Cell Stack Monitoring". In: *Hyfindr* (2023).
- [83] Tim Burschyk , Yannic Cabac. "Liquid hydrogen storage design trades for a short-range aircraft concept". In: *CEAS Aeronautical Journal* (2023).
- [84] Italo Raffaelli. *Effect of Altitude on Power of Aviation Engines*. Tech. rep. National Advisory Committee for Aeronautics, 1924.
- [85] W.D. Gove. *The variation in engine power with altitude determined from measurements in flight with a hub dynamometer*.
- [86] Rana Adil Abdul-Nabe , Dr. Mohammad Tariq. "Thermal Analysis of a Gas Turbine". In: *IJARET* (2014).
- [87] Gary McCreadie. "The Hot Gas Bypass Valve Explained". In: *HVAC Know It All* (2024).
- [88] Jayant Mukhopadhyaya, Dan Rutherford. "Performance analysis of evolutionary hydrogen-powered aircraft". In: *International council of clean transportation* (2022).
- [89] Nazar Oudah Mousa Alyaseen, Salem Mehrzad, Mohammad Reza Saffarian. "Design of the Multistream Plate-Fin Heat Exchanger in the Air Separation Units". In: *International Journal of Heat and Technology* (2023).
- [90] "The Standards of Braze Aluminium Plate-fin Heat Exchanger Manufacturers' Association". In: *ALPEMA* (2000).
- [91] "Aluminium Plate-fin Heat Exchanger". In: (2012).
- [92] *Compatibility of Metals Alloys in Neat Methanol Service*. Methanol Safe Handling technical bulletin.
- [93] Sadik Kakac , Hongtan Liu , Anchasa Pramuanjaroenkij. *Heat Exchangers, Selection, Rating, and Thermal Design*. CRC Press Taylor and Francis Group, 2020.
- [94] Xu Jing-hua , Chen Xiao-jie , Zhang Shu-you. "Thermal design of large plate-fin heat exchanger for cryogenic air separation unit based on multiple dynamic equilibriums". In: *Applied Thermal Engineering* (2017).
- [95] Masoud Asadi. "Analysis of Heat Transfer arising radiation in circular finned-tube heat exchanger". In: *International Journal of Technology in Education* (2013).
- [96] M.V.V. Morteau , M.B.H. Mantelli. "Nusselt number correlation for compact heat exchangers in transition regimes". In: *Applied Thermal Engineering* (2019).

- [97] Tao Liang , Wanwu Xu , Wei Ye. "Study on the heat transfer characteristics of a plate-fin-typed precooler considering cooling fluid phase change". In: *Case Studies in Thermal Engineering* (2023).
- [98] T.M. Adams , S.I. Abdel Khalik , S.M. Jeter. "An experimental investigation of single-phase forced convection in microchannels". In: *International Journal of Heat and Mass Transfer* (1998).
- [99] *Plate Fin Heat Exchanger Component*. Altair Flow Simulator. Version 2024.
- [100] *Properties of mixture Water/Glycol*. 1991.
- [101] Ralph L. Webb. "Plate Fin Surface Geometries". In: *Heat Exchanger Design Handbook* (2014).
- [102] M. Rafiqul Islam. *Reservoir Development*. Gulf Professional Publishing, 2021.
- [103] *Pump Efficiency – Why is it Important?*
- [104] *Pump Power Calculator*. Engineering Toolbox. 2003.
- [105] *The EWP 115 Electric Water Pump*. Davies Craig.
- [106] Jaroslaw Polinski. *Materials in Cryogenics*. 2010.
- [107] D. Verstraete , P. Hendrick. "Hydrogen fuel tanks for subsonic transport aircraft". In: *International Journal of Hydrogen Energy* (2010).
- [108] "DeHavilland Canada / Bombardier Dash 8." In: *Modern Airlines* (2023).
- [109] *BOMBARDIER Dash 8 Q300*. Skybrary Aviation Safety.